Simulation of Hydraulic Fracturing Fluid Cleanup for Partially Degraded Fracturing Fluids in Unconventional Gas Reservoirs

By

Regina Tayong Abubei

B.Sc., University of Buea-Cameroon, 2012

Submitted to the graduate degree program in the Department of Chemical and Petroleum Engineering and the Graduate Faculty of the University of Kansas in partial fulfillment of the requirements for the degree of Master of Science in Petroleum Engineering.

_____

Chair: Dr. Reza Barati

_____

Dr. Shapour Vossoughi

_____

Dr. Russell Ostermann

Date Defended: 05/18/2017

The Thesis Committee for Regina Tayong Abubei

Certifies that this is the approved version of the following thesis:

SIMULATION OF HYDRAULIC FRACTURING FLUID CLEAN–UP FOR

PARTIALLY DEGRADED FRACTURING FLUIDS IN UNCONVENTIONAL GAS

RESERVOIRS

_____

Dr. Reza Barati

(Chairperson)

Date approved: 05/23/2017

Abstract

Unconventional reservoirs are low porosity and low permeability reservoirs ($< 0.1 md$), usually requiring enhanced stimulation techniques such as hydraulic fracturing and horizontal drilling to increase the contact between the wellbore and the producing formation for a profitable recovery. During the fracturing process, fluids are pumped into the reservoir under high pressure, to create fractures through which gas flows back to the earth's surface during production. We expect these fracturing fluids to properly clean up during production. The inadequacy of our cleanup processes after a fracture treatment is typically due to poor degradability of our polymers, proppant crushing, clay swelling in the case of incompatible fluids and formation damage.

This thesis summarizes the development of a comprehensive workflow, from characterizing an existing reservoir to simulating fluid flow and recovery performance through a fractured grid. A 2-D, three-phase IMPES simulator, incorporating a yield-power-law-rheology (Herschel-Buckley fluids), has been developed in MATLAB to characterize fluid flow through a hydraulic fractured grid and assess the influence of increasing breaker activity on yield stress and broken gel viscosity, varying polymer concentration along the fracture face, fracture conductivity, fracture length and capillary pressure on the fracturing-fluid cleanup process and cumulative fluid recovery in tight gas reservoirs.

The effect of increasing capillary pressure in the formation simulated in this study resulted in a 10.4% decrease in cumulative production after 100 days of fluid recovery. Increasing the breaker concentration from $5 - 15\ gal/Mgal$ on the yield stress and fluid viscosity of a $200\ lb/Mgal$ guar fluid resulted in a 10.83% increase in cumulative gas production. Several correlations have been developed relating polymer concentration to distance along the fracture face and injection time. The rate at which the yield stress (τ_o) is increasing is found to be proportional to the square of the volume of fluid lost to the formation. For tight gas formations ($k = 0.05\ md$), fluid recovery increases with increasing shut-in time, increasing fracture conductivity and fracture length, irrespective of the yield stress of the fracturing fluid. Mechanical induced formation damage combined with hydraulic damage tends to be the most significant.

Acknowledgments

Contents

List of Figures

List of Tables

1   Introduction

1.1   <u>Statement of the Problem</u>

Natural gas provides roughly 30% of the energy in the United States, and it is diversely used in heating our homes, electricity generation as well as a raw material in a variety of common products such as paints, fertilizers, plastics, medicines and antifreeze. It is typically preferred to the use of coal or petroleum for combustion because it releases fewer undesirable by-products per unit energy [1].

The U.S. Energy Information Administration (EIA) estimates about 2,474 trillion cubic feet of technically recoverable resources of dry natural gas in the United States as of January 2014. Despite the 26.6 trillion cubic feet of natural gas that is estimated consumed each year, the United States still has enough natural gas to last for the next 100 years [2]. Several measures have been taken to enhance energy security in the United States during the last decades, some of which include the development and exploitation of very low permeability and low porosity fields in challenging environments. These reservoirs, usually involve huge development costs from subsurface characterization to production, and as such careful data analysis and reliable production forecast are required.

Tight gas reservoirs are characterized by very low permeability $(< 0.1\ md)$, economic volumes of natural gas can only be produced if the well is subjected to stimulation by a large hydraulic fracture treatment, a horizontal wellbore, or by using multilateral wellbores to increase contact between the wellbore and the producing formation. The first hydraulic fracturing experiment was conducted in 1947 at the Hugoton gas field in Grant County of southwestern Kansas [3]. This experiment was not very successful as the productivity of the well did not change considerably. Halliburton performed the first two commercial hydraulic fracturing treatments in Stephens County, Oklahoma, March 1949 and for the past ten years, it has become the technique by which most of the natural gas is produced in the United States. EIA estimates from the most recent data divulge that hydraulic fractured wells account for two-thirds of the total U.S. marketed gas production and about half of the current U.S. crude oil production [4]. Despite the huge environmental and human health concerns, hydraulic fracturing has had a wide variety of

successful applications in horizontal, directional and vertical wells, natural gas and oil wells and in both tight and non-tight formations

During the fracturing process, fluids (typically a mixture of water, proppant and chemical additives) are pumped at sufficiently high pressures to crack the rock open, and under very high injection rates to propagate the fracture through the formation. Some of the fluid eventually leaks off into the formation to create the invasion zone, leaving back polymer residues that form the filter cake. **Figure 1** shows the different regions created in a reservoir after a fracture treatment. Original fracturing fluids may remain in the fracture unless the filter cake occupies the entire pore space of the propped fracture following closure [5]. Fracturing fluids used should possess two important qualities: (i) They must be viscous enough to carry the proppants along the fracture. (ii) They should be easily broken down after injection to sustain a highly conductive path in the fracture during production. Guar based fluids are frequently used as fracturing fluids during injection. Cross-linkers (such as borates and zirconates) and delayed breakers (either oxidizers or enzymes) are added to the fluid to degrade the polymer gel and filter cake formed before the start of production [6]. Enzyme breakers are generally used in place of oxidizers as they are cheaper, less corrosive, more environmentally friendly and not expended during the reaction. Encapsulating agents are used for the breakers to prevent them from degrading the polymer gel before the fracture is propagated. Water based fracturing fluids are preferred to gel fracturing fluids because they are cheaper, safer and easy to clean up [7]. At the end of the fracture treatment process, the well is shut-in to allow for fracture closure during which fluid filtrate continues to leak off into the matrix, thereby increasing the concentration of polymer formed on the fracture face. The thickness of the filter cake formed is a function of the type of fracturing fluid used, reservoir properties, pressure gradients between reservoir and fracture and the erosional effect of the slurry on the fracture face [8].
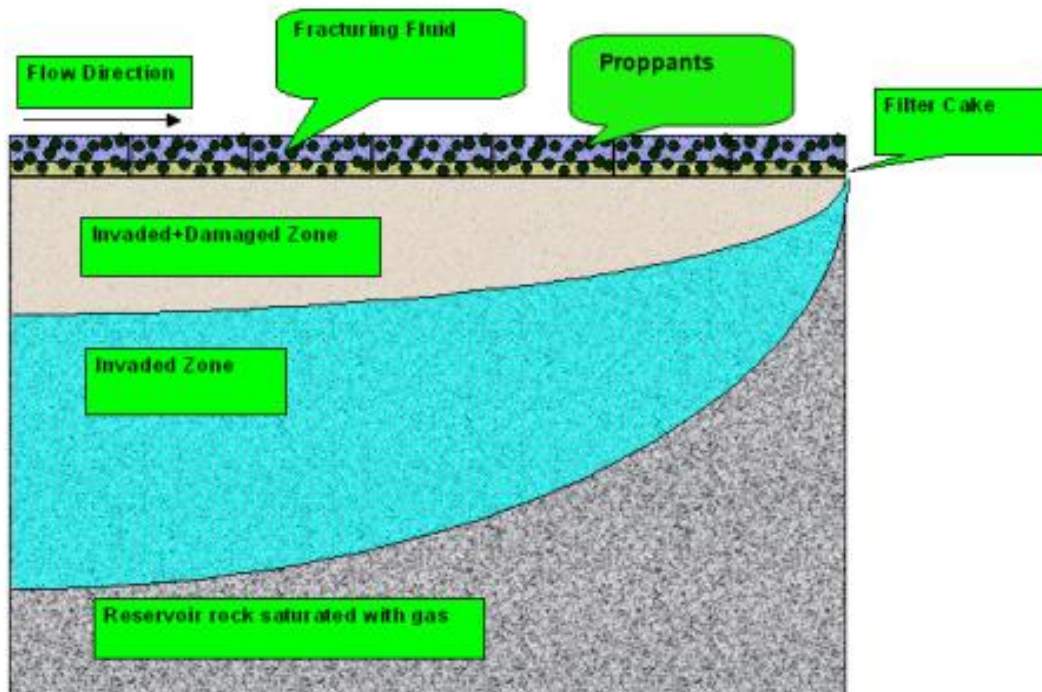
Figure 1. Schematic picture of the different regions created in a reservoir after fracture treatment (drawn by Dr. Reza Barati: used with permission) [9].

The gas flow mechanism in the reservoir will change from radial to linear flow after a successful fracture treatment [10] as in **Figure 2**. Concentrated polymer residue on the fracture face generates a yield stress, which requires a minimum pressure gradient to begin the cleanup process in the proppant pack [11]. During the cleanup process, fluids flow through the fracture back out of the well, leaving behind the proppants that help to keep the newly created fissures open. These fissures typically extend into the formation enabling oil and gas to flow from pores within the formation to the production well. The initial fluid that returns to the surface is usually termed "flow back" and the fluid that flows from the well along with oil and gas during the production phase is often referred to as "produced water''. Long cleanup periods following a fracture treatment are typically due to a combination of poorly degraded polymer fluids, low formation bottom-hole pressures and/-or large retained liquid volumes. The joint effects of non-Darcy flow, stress dependency of reservoir permeability, fracture closure and high capillary pressure in the matrix can contribute to a 40% cut in production over a 10-year period under realistic conditions [12].
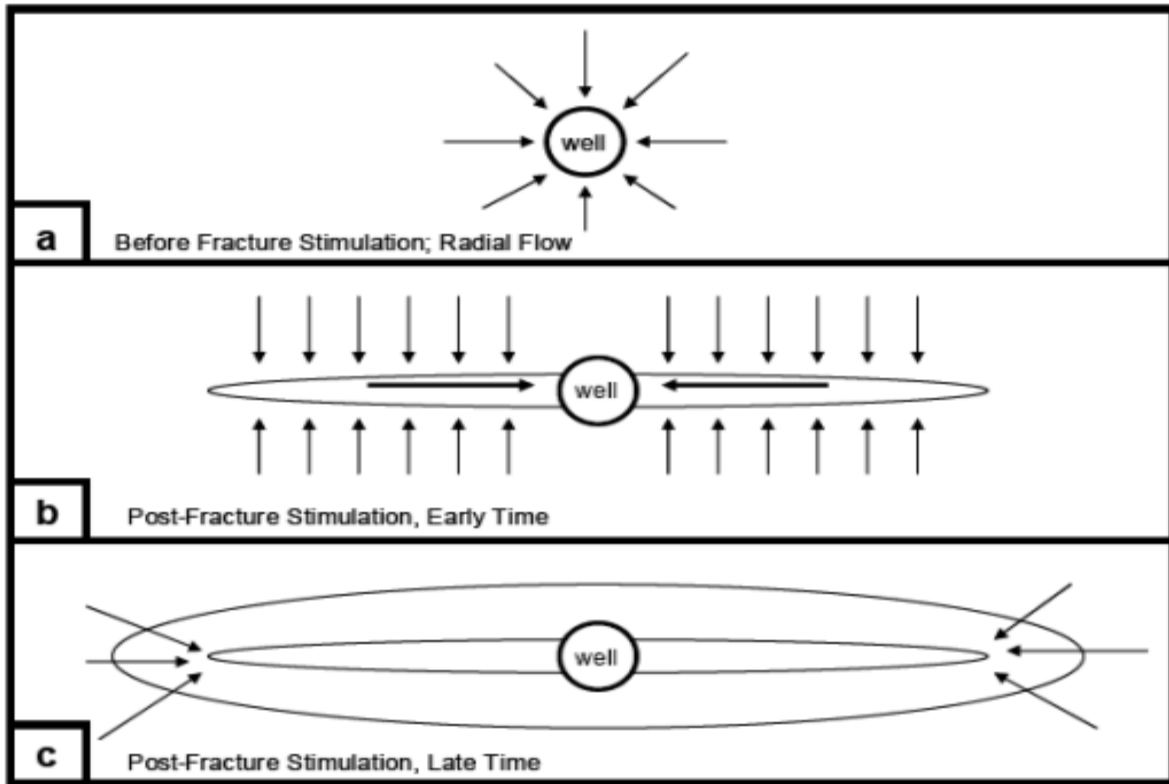
Figure 2. Gas fracture mechanisms before and after fracture treatment [11]

The severity of formation damage varies with reservoir characteristics and is most commonly dependent on the kind of wellbore fluids used during drilling, completion and workover operations. It may occur near the well-bore region of a well or extend deep into the formation, resulting in a reduction in permeability and adversely curtailing productivity. Mechanical, chemical and hydraulic damage to the reservoir have resulted from hydraulic fracturing process. Mechanical damage typically results from broken polymer/fines migration into the reservoir matrix under very high fluid shear rates, external solids entrainment that plug formation pores, phase trapping and blocking, perforation damage, proppant crushing and embedment. Chemical damage is caused by adverse rock-fluid interactions, adverse fluid-fluid interactions and near wellbore wettability alterations resulting in clay swelling, clay de-flocculation, formation dissolution, pore plugging and a switch from water-wet to oil-wet conditions. [13]. Hydraulic damage in the invaded zone arises from the increase in water saturation during leak-off, which causes a shift in capillary pressures to higher values, a reduction in gas relative permeability and relative permeability

hysteresis in the invaded zone. However, mechanically induced formation damage combined with hydraulic damage tends to be the most significant for low permeability reservoirs [14].

1.2 <u>Objectives</u>

Despite the extensive application of breakers in hydraulic fracturing treatments, the effective fracture length is often less than 50% of the propped fracture length. This is typically due to insufficient proppant concentration or poor proppant transport, the use of the wrong propping agent or a fracturing fluid that fails to break to a low viscosity fluid after fracture treatment [7].

This study has been designed to create a better understanding of the fracture treatment process and the shortcomings of its application in tight gas reservoirs, with the following main objectives;

1. Modeling the physics of nonlinear multiphase flow through the development of a three-phase IMPES (Implicit pressure-explicit saturation calculations) black Oil Simulator. This simulator was validated by solving a three-phase flow problem and history matching results obtained with that reported in the literature.
2. Modeling fracturing fluid flow by considering the Rheology inside the fracture and examining the influence of yield stress of filter cake, capillary pressure, fracture conductivity, fracture length, aqueous phase trapping and formation damage on the cleanup process in unconventional tight gas formations.

1.3   <u>Organization</u>

This thesis is written in five chapters. Chapter 1 introduces the subject and summarizes the workflow of events. Chapter 2 presents a critique of relevant work that has been done with respect to assessing of mechanisms related to damage and cleanup in hydraulically fractured wells. Chapter 3 reports the methodology used in this work. It is divided into two parts. Part I highlights the steps in the development of a three-phase flow IMPES Black oil simulator in 2-D (Cartesian co-ordinates). Part II simulates fracture cleanup and factors affecting the effectiveness of the fracturing fluid cleanup process in tight gas reservoirs using the model developed in Part I. Chapter 4 focuses on the results and analysis of the history matched data used to validate the model and the factors influencing the effectiveness of the fracturing cleanup process in tight gas formations. Chapter 5 concludes this thesis with key recommendations for future applications.

2   Literature Review

The choice of fracturing fluids and proppants has proven over the years to be very crucial to the success of a fracturing cleanup process. Tight gas reservoirs have become the center of unconventional gas production due to their huge hydrocarbon reserves. However, they cannot be economically and profitably exploited unless subject to large hydraulic fracture treatments or produced using horizontal drilling. Most of these fracture treatments have failed to deliver the desired results of enhanced gas production due to inadequate fracturing fluid cleanup and formation damage.

Several simulators have been reported in the literature for investigating fracture face damage mechanisms and factors affecting fracturing fluid cleanup in hydraulically fractured wells. A critique of relevant work done in this area is summarized in the following four subsections.

2.1   <u>Simulations of Holditch and Wang et al.</u>

Holditch [15] used a single-phase 2-D finite difference model to simulate the effects of reservoir permeability damage around a fracture and a fully implicit two phase, two-dimensional model to investigate the effects of relative permeability and capillary pressure on the productivity of fractured reservoirs.

He identified three distinct permeability zones: the reservoir, fracture and damage zone. Capillary pressure calculated for each region was by means of the measured Leverett J-function for the desired rock type, as given in **Equation 1,**

$$P_c = \sigma \cos(\theta) J(S_w) \sqrt{\frac{\phi}{k}} \qquad (1)$$

where P_c capillary pressure is in (kPa), σ the interfacial tension is in (mN/m), the permeability k is in md and J the productivity index is in $(m^3/kPa.d)$.

He made the following important observations:

- With increasing degree of damage, the capillary pressure tends to have a terrific effect on gas production by water blockage in the damage zone. A 6-inch damage zone with 10% of its initial permeability caused more than 15% loss in productivity. If the reservoir-rock permeability next to the fracture is undamaged by fracturing fluid invasion and the pressure drawdown greatly exceeds the capillary pressure, the cumulative gas produced becomes independent of capillary pressure.

- Unless the reservoir rock permeability is damaged by fracturing fluid invasion, a complete water blockage to gas flow cannot occur except water mobility is so low in the fracture face and the pressure drawdown fails to exceed formation capillary pressure.

He concluded that the effect of formation damage was significant only if it was several inches deep and reduced the formation permeability by a factor of 100 or more. Secondly, the relative permeability damage alone will restrict gas production only when the injected fluid is not easily removed from the invaded zone. Finally, his results indicated that the damaged zone permeability must be reduced by several orders of magnitude and the capillary pressure altered before a serious water block to gas flow will occur.

Wang et al. [7] used a three dimensional three-phase black oil simulator to simulated the effects of gel residue, filter cake formation and yield stress on fracturing fluid clean up and long term gas recovery in tight gas formation. He validated his model against Voneiff's work [16] for Newtonian fluid flow without yield stress and Friedel's model [12, 17] for Herschel Buckley fluids with finite yield stress values.

The fracturing fluid invasion zone was modelled by injecting water into the reservoir for 0.1 day. The reservoir initially was assumed to have gas and water phase only, the gel phase in the proppant pack was injected during the fracture treatment. Relative permeability curves from tight gas cores in West Texas were used in simulating multiphase flow of gas, water and fracturing gel through a homogeneous and isotropic reservoir. Properties of fracturing fluid filtrate were assumed same as those of water. Only ¼ of the drainage area from the fractured well was simulated. He ran several simulation cases to investigate the factors influencing fracturing fluid cleanup. Some of which include the effect of yield stress of filter cake, the effect of fracture conductivity, the effect of fracture length and initial pressure.

Table 1. Simulation scenarios investigated in Wang et al. [7] model.

CASES	SCENARIOS
1	Single phase model
2	Gas/water model
3	Filter cake (thickness)
4	Yield stress model

In-situ stress was evaluated from **Equation 2**,

$$\sigma_{min} = \frac{v}{1-v}(\sigma_z - p) + p + \sigma_{ext}$$

(2)

where v is the Poisson's ratio, σ_z is the overburden pressure, p is the pore pressure and σ_{ext} represents any external stress. The main conclusions were as follows;

- Fracture proppant crushing and unbroken gel are very instrumental to the effectiveness of a cleanup process after treatment.
- If the fracturing fluid breaks down to a Newtonian fluid, then a dimensionless fracture conductivity of 10 or greater is suitable for optimizing gas production and fracturing fluid cleanup. If the fracturing fluid does not break but retains a gel strength of 3-100 Pa, then the fracturing fluid either cleans up slowly or never cleans up when a dimensionless fracture conductivity value of 10 or less is applied.

2.2   **Simulations of Gdanski et al.**

In 2005, Gdanski et al. [18] modeled the effect of formation damage in the invaded zone by correlating the capillary function with the Leverett J function. The resulting equation was used in modeling capillary pressure in the matrix.

$$P_c = \frac{\sigma}{a_2 S_w^{a1}}(\frac{\phi}{k})^{a3}$$

(3)

where P_c is the capillary pressure, $\boldsymbol{\sigma}$ is the surface tension and a1, a2 and a3 are adjustable constants.

Now considering **Equation 3**, mechanical damage resulting in lower matrix permeability raises the capillary pressure in the damaged zone causing an influx of water from the undamaged matrix. Higher water saturation in the damaged zone adversely affects gas production. After varying the relative permeability to gas for constant water curve, he observed that water production was equally a function of gas relative permeability in which lowering the gas permeability at high water saturations raised the pressure near the fracture face and consequently water production. He postulated that the relative permeability and capillary pressure changes were unimportant for the undamaged matrix if high capillary pressure imbibed more water into the reservoir and a high-pressure drawdown existed to overcome the capillary pressure differences between the invaded and unadulterated portions of the formation. They calculated the skin factor on the face of the fracture from **Equation 4,**

$$s = \left(\frac{k}{k'} - 1\right)\left(\frac{\pi w}{2x_f}\right) \tag{4}$$

where x_f and w are the fracture length and width respectively, k and k' are the permeability of undamaged and damaged.

In 2006, using the same model Gdanski et al. [19], made improvements on previously published results after considering that the apparent lower fracture face skin could be due to pressure drop across the damaged zone that lowers gas density and viscosity. Skin factor calculations for m number of cells along the fracture and n-1 number of invaded cells perpendicular to the fracture were modified to

$$s = \left(\frac{\pi}{2x_f}\right) \sum_{j=2}^{n} wj \left(\frac{\left(\frac{k_g}{\mu_g}\right)_0 x_f}{\sum_{i=1}^{m}\left(\frac{k_g}{\mu_g}\right)_{i,j} L_I} - 1\right) \tag{5}$$

where $\left(\frac{k_g}{\mu_g}\right)_0$ the undamaged mobility to gas is measured at the reference point (0), x_f and w are the fracture length and width respectively.

Two main scenarios for the damaged formation were considered when monitoring the apparent fracture face skin variation with time. The first scenario considered a saturation dependent capillary pressure for low permeability values. High capillary pressure values slackened the cleanup process and the skin factor computed from **Equation 5** was significantly reduced with time. The second scenario considered formation damage for which capillary pressure is both saturation and permeability dependent. Here the skin factor computed decreased slowly with time or remained unchanged. Severe damage was reported for both cases for a $k/k_d > 100$.

Finally, in 2009 Gdanski et al. [19] used a new backward difference scheme on a two-phase two-dimensional model to demonstrate that the fracture face skin relative to gas flow can be calculated continually throughout a fracturing treatment cleanup and production process using an expansion of the classical Cinco-Ley and Samaniego fracture face skin equation [20]. He established that the effect of water saturation in the damaged zone becomes much more significant for lower permeability and higher capillary pressures in the matrix and that the effective fracture face skin relative to gas could be several times higher than expected from a single-phase flow. Fluid invasion into the matrix reduces the permeability to gas by relative permeability effects, clay swelling and clay dispersion. It also shifts the capillary pressure to the left by relative permeability hysteresis from phase trapping. Clay swelling and dispersion could easily be avoided by suitable choice of brine for the fracturing fluid. Two scenarios were considered when the fracturing fluid caused a loss in permeability in the invaded zone. A kaolinite dispersion scenario for capillary pressures that are unchanged by the loss of permeability and a smectite-swelling scenario for capillary pressures that increase as per the leverett J-function. Conclusively, his results demonstrated that there would always be a higher fracture face skin to gas in the smectite-swelling scenario than in the kaolinite dispersion scenario. In addition, for tight gas reservoirs (~0.01 md or less), even a small amount of matrix damage could result in high fracture face skins and significantly prolong cleanup times. Also, that tight gas reservoirs were much more susceptible to water blocking by clay damage than formations with higher permeability.

2.3   Simulations of Friedel and Barati et al.

Friedel [12, 17] developed a fast and stable fully implicit, three-phase black oil simulator capable for modeling YPL behavior of fracturing fluids flowing through the proppant pack. The equations of power law behavior after gel yielding and yield stress were obtained from the work of Al-Fariss

et al. [21]. The algorithm for choosing suitable grids for fractured wells was determined by Bennett et al. [22]. It is designed to create finer grids near the fracture face, wellbore and fracture tip. Only 1/4 of the drainage area from the fracture was simulated assuming a symmetric fracture that extends equal distances on both sides of the wellbore and fully penetrates the formation. He investigated the effects of non-Darcy flow and stress dependency of tight reservoir rocks, usually neglected in most fracturing fluid cleanup studies. He concluded that inertial effects were more influential than non-Darcy effects in the fracture, but non-Darcy effects if neglected will result in an overestimation of production. Also, he stated that the combined effects of permeability dependence on stress and non-Darcy effects decreased production by 40% compared to the case without non-Darcy flow.

A two dimensional two-phase injection model was used to simulate hydraulic damage and generate initial conditions for the polymer clean up model. Capillary pressure curves in the formation were calculated using Brooks-Corey correlation assuming a material parameter (λ =1).

$$P_c = P_d S_{wd}^{-\lambda} \tag{6}$$

The displacement pressure P_d correlates with the absolute permeability of a typical tight gas Rotliegend reservoir.

$$P_d = 0.886k^{-0.693} \tag{7}$$

$$S_{wd} = \frac{S_w - S_{wi}}{1 - S_{gc} - S_{wi}} \tag{8}$$

Relative permeability curves used were equally representative of a tight gas formation. Within the fracture, linear relative permeability curves and zero capillary pressures were applied.

In 2009, Barati et al. [23] modified Friedel's model [12, 17] and further investigated the fracturing cleanup process in tight gas formations with permeability of 0.005md and greater. This model was validated against type curves published by Argarwal et al. [24] for a single well connected with a finite conductivity fracture in an infinite reservoir producing under constant pressure, to ratify that the fine-grid system around the fracture did not affect the calculations. Capillary pressure curves

were not scaled in the damage zone but were limited to a maximum value for most of the runs. However in his final set of runs he made use of a capillary pressure that was scalable with permeability according to the Leverett J-function. A total of $30\ m^3$ of water was injected to create the leak-off volume for half a day after which the well was shut–in for the same amount of time. Finally a polymer clean up model was used in assessing the influence of capillary pressure changes, yield stress of the filter cake and broken gel viscosity, formation damage and fracture conductivity on production from tight gas reservoirs. The three phases under consideration were gas, water and the gel phases.

After a thorough analysis of the effects of capillary pressure, yield stress, conductivity and mechanical damage on the fracturing fluid cleanup process, they concluded that

- The model with Bennett gridding accurately represented the transient response of a hydraulic fractured well.
- Capillary pressure caused the leak off water to be imbibed deeper into the reservoir. Increasing the capillary pressure had insignificant effects on gas and gel production but not on water production. This effect became more significant for lower permeability values.
- Gas and water production increased with increasing fracture conductivity. Gel production increases with increasing fracture conductivity only if the pressure gradient along the fracture is greater than the yield stress needed for the fluid to move for low permeability formations. However, if the permeability is increased above 5md, yield stress effects become insignificant.
- Increasing the yield stress and viscosity values of fracturing fluids negatively affects the production of gas, water and gel. However if the reservoir permeability is increased above 5md these effects become less significant for the conditions modelled in his study.
- When a yield stress power law fluid is present, any small amount of damage causes a decrease in the amount of gas production. Decreasing reservoir permeability makes these effects more significant.
- Finally, they stated that the effects under consideration become less significant when reservoir permeability exceeds 5md for the conditions modelled in their study.

2.4 Simulations of Ghahri et al.

Ghahri et al. [25], developed a Matlab-ECLIPSE100 coupled computer code that has the capabilities of reading input data, and automatically linking the injection and production periods to generate an output for over 130000 runs on a single-well model. For their cleanup study, they investigated the influence of 16 parameters that govern the gas and fracturing fluid effective permeability of the matrix and the fracture, pressure drawdown, capillary pressure and porosity using two injected fracture fluid volumes. They validated their model by mapping the gas production loss (GPL) to the 100% cleanup case using linear and quadratic response surface methods. A least square method was applied to estimate the regression coefficients in their models that were scalable for intercepts with height value.

They injected water (with viscosity of $0.5\ cp$) as fracturing fluid into a 3-D Cartesian grid to create the initial conditions for the production period. The volume of fluid injected is assumed to fully saturate the fracture at the start of injection period. Their grid was optimized to a width of 0.001m to increase numerical stability and minimize dispersion error for a fracture length of 400m.

Three methods were used to sample the range of variation of the parameters they considered for their study: a two-level full factorial statistical experimental design, a three-level Box-Behken and a Central Composite design method. They made comparisons of the GLP obtained to the 100% cleanup scenario for each run at three different production periods following fluid injection.

Their main inferences were as follow:

- For all production periods, experimental design and response surface methods simulated, the GPL realized was significantly affected by fracture permeability.
- With continuous fluid injection and gas production, the number of cases with severe gas production loss decreases but the relative importance of the pertinent parameters increases, i.e. most of the parameters tend to have higher values of coefficients based on response surface methods after longer production periods.
- For all experimental design and response surface methods applied, the influence of residual gas saturation within the fracture and gas relative permeability for scaled coefficients less than 0.1 were negligible.

- Increasing the fracture fluid volume significantly increases the percentages of the cases with severe fracture fluid damage and GPL, thereby delaying the fracture cleanup process.

- Finally, for absolute scaled coefficient values greater than or equal to 0.2, most of the parameters investigated in their study tend to affect the GPL obtained more after 1 year of production.

2.5   Simulations of Cai et al.

Hydraulic fracturing has been widely applied to develop tight oil and gas wells. However, not all wells have had a positive response to monotonous fracturing treatment, rather huge production costs were incurred. Their study has been the latest approach to analyzing the influence of fracture face damage skins (FFDS) on fracturing fluid cleanup. They developed a new FFDS mathematical model based on the classical model of Perkins-Kern-Nordgren (PKN) and Khristianovic-Geertsma-Daneshy (KGD) using fluid/rock mechanics, fluid coupling method and tomography (CT) scanning for a rectangular, homogeneous and closed boundary reservoir [26].

The average velocity of any point along the fracture length direction was computed from **Equation 9,**

$$V_x = \frac{qx}{w_x h}$$

(9)

where V_x the average flow rate is in m/min, q is the fluid rate, x is the distance to the fracture vertical fracture and h is the reservoir thickness. The parameters in Gdanski et al.'s equation [19] for calculating fracture face skin were modified to be a function of a dimensional net pressure P_{net}

$$s = P_{net}(k, k_s)(\frac{\pi w}{2 x_f})$$

(10)

For their case study, they pumped four different volumes of proppants at different rates into a tight oil reservoir for the same stratum and net pay. They concluded that

- Propping agents and reservoir rock interactions may change the strength of the rock surface during the fracture treatment. When the effective stress increases, the proppant in the fractures embedded on broken rock particles affect greatly the propped fracture conductivity. Increasing proppant embedment within the fracture requires additional pressure drop that reduces the flow capacity of the reservoir.

- The influence of FFDS on productivity was increased from 5% to 51% using their new model for a permeability of 0.1 md relative to their former model. However, the FFDS has a negative effect on productivity only during the wellbore storage and fracture linear flow period.

- Particle migration to the effective layer could result in serious blockage of the effective layer. Their study showed that 5% of the damage might reduce the flow capacity by 60%.

- Increasing pressure and lowering the permeability increased the impact of FFDS from experimental evaluation conducted using tomography scanning and rock mechanics. However, the impact of FFDS could be reduced by using a low viscosity fracturing fluid, optimizing the viscosity value of fracturing fluid with corresponding treatment parameters or Acid-fracturing to minimize skin damage.

- Finally, they reported that their model would offer a better solution for pressure distribution and fracture face skin analysis in hydraulic fracturing designs.

3   Simulator Methodology

Simulation studies for this project were conducted in two parts. To begin with, a three-phase simulator was developed in MATLAB using a two dimensional structured grid system. This model is very fast, stable and has the capabilities of handling both anisotropic/isotropic, homogeneous/heterogeneous as well as different types of boundary conditions. This simulator was validated by solving the three-phase flow exercise provided in Ertekin's textbook [27]. Fluid PVT Data, relative permeability and capillary pressure curves imported into the Simulator were gotten from the A-1 reservoir situated in Plum Bush Creek field, Washington County, Colorado. History matching for all the five wells reported for this field was very successful. For the second half of this project, reservoir grids were altered to suit what is recommended for fractured grid system using Bennett's algorithm. A two-phase fracture propagation model was used to create the formation damage and invaded zone by injecting water for 0.05 and 0.1 of a day and shutting in the well for roughly equal amounts of time. Pressure and saturation maps at the end of shut-in periods was used to establish the initial conditions for our polymer clean up model. Our polymer model was simulated by replacing the oil phase in our three-phase simulator with fracturing fluid (gel). The gel phase was restricted to the fracture. Lastly, this model was used to study the effect of increasing breaker concentration on broken gel viscosity and yield stress, the effect of capillary pressure changes, fracture conductivity, aqueous phase trapping, fracture length and formation damage on fluid recovery in tight gas formations with permeability of 0.05md.

3.1   Phase I: Modeling Multiphase Flow in the A-1 Reservoir

Mathematical simulation of reservoir behavior is essential to understanding flow processes, reservoir behavior and potential for the most economically efficient and sustainable exploitation. This chapter embodies the fundamentals of modeling a multiphase flow reservoir system through a proper understanding of the reservoir-rock properties, the reservoir-fluid properties, phase relative permeability and capillary pressures.

3.1.1 Reservoir-Rock properties

Reservoir-rock properties such as porosity and permeability are assumed independent of fluid content, provided the rock and fluid are non-reactive.

3.1.1.1   Porosity

Porosity is a measure of the volume or void space within a rock that can contain fluids. These pore spaces could be either interconnected or isolated. Two porosity types exist in a real reservoir rock, total porosity that includes both isolated and interconnected pore spaces and effective porosity which includes only interconnected pores. We are mostly concerned with the effective porosity in a rock because it contributes to the free flow in a reservoir. Reservoir porosity usually varies in space from one point to the other and from one region to another. The A-1 formation consists of poorly to well sorted Cretaceous Dakota J sands. This sands exhibit excellent reservoir quality, with an average effective porosity of 21.4%.

The pore volume for a producing reservoir changes with time. This variation is a function rock compressibility and the pressure dependence of porosity. The porosity of the A-1 rock at any given pressure is calculated from **Equation 11,**

$$\phi = \phi^o \left[1 + c_\phi (p - p^o) \right] \tag{11}$$

where p^o is the reference pressure, usually the initial reservoir pressure or the atmospheric pressure at which the porosity is ϕ^o. Porosity of reservoir rock increases with increasing pressure exertion from the fluids in the interconnected pore spaces as depicted in **Equation 11**. Initial porosity distribution derived from core analysis and well test data for our formation of interest are shown in **Figure 3**.
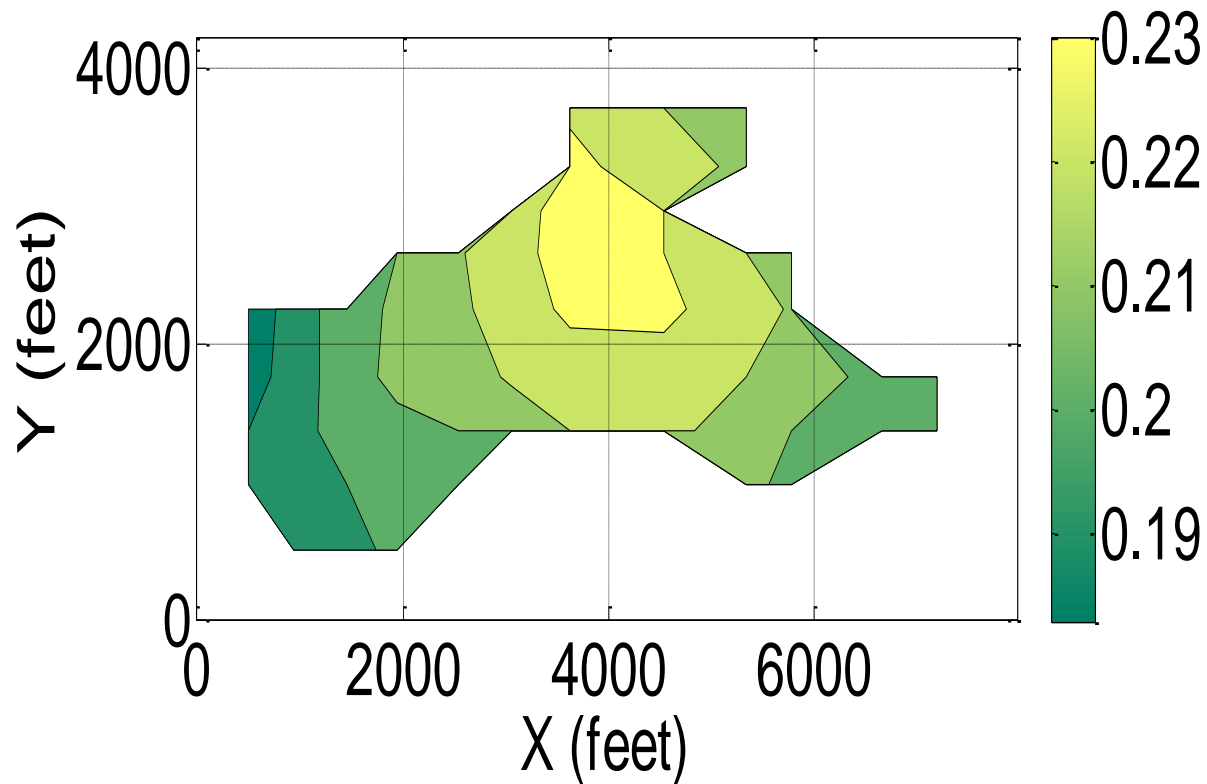
Figure 3. Porosity distribution map for A-1 reservoir

3.1.1.2   **Permeability**

Permeability measures the ability of a rock to convey fluids through its interconnected pores. Permeability measurements for a given formation are usually reported in Darcy or millidarcy. Sandstones have many large and well-connected pores, as such they are described as permeable since they transmit fluids with ease. Shales and siltstones are fine grained with fewer interconnected pores as such they don't readily transmit fluids. If a single fluid phase is present in the reservoir rock, the permeability is referred to as the absolute permeability. If two or more phases exist in the pore spaces, the reservoirs capacity to transmit any phase is called the effective permeability to that phase. The relative permeability to a particular fluid, is the ratio of the effective permeability of that fluid at a particular saturation to the absolute permeability of that fluid at total saturation. Permeability in the gas phase is a function of pressure due to the Klinkenberg effect [28].

Permeability is a directional property that varies from one point to another. If the permeability of a reservoir in the x, y, z directions are equal i.e. ($k_x = k_y = k_z$), then the porous medium is described as being isotropic. If the permeability is different in the x, y, z directions then the medium is anisotropic. Permeability in our reservoir rock of interest shows a directional bias, ($k_x \neq k_y$) with values ranging from 250 to 300 md and averaging at a value of 279.6 md for the field. Permeability distributions are shown in **Figure 4**.
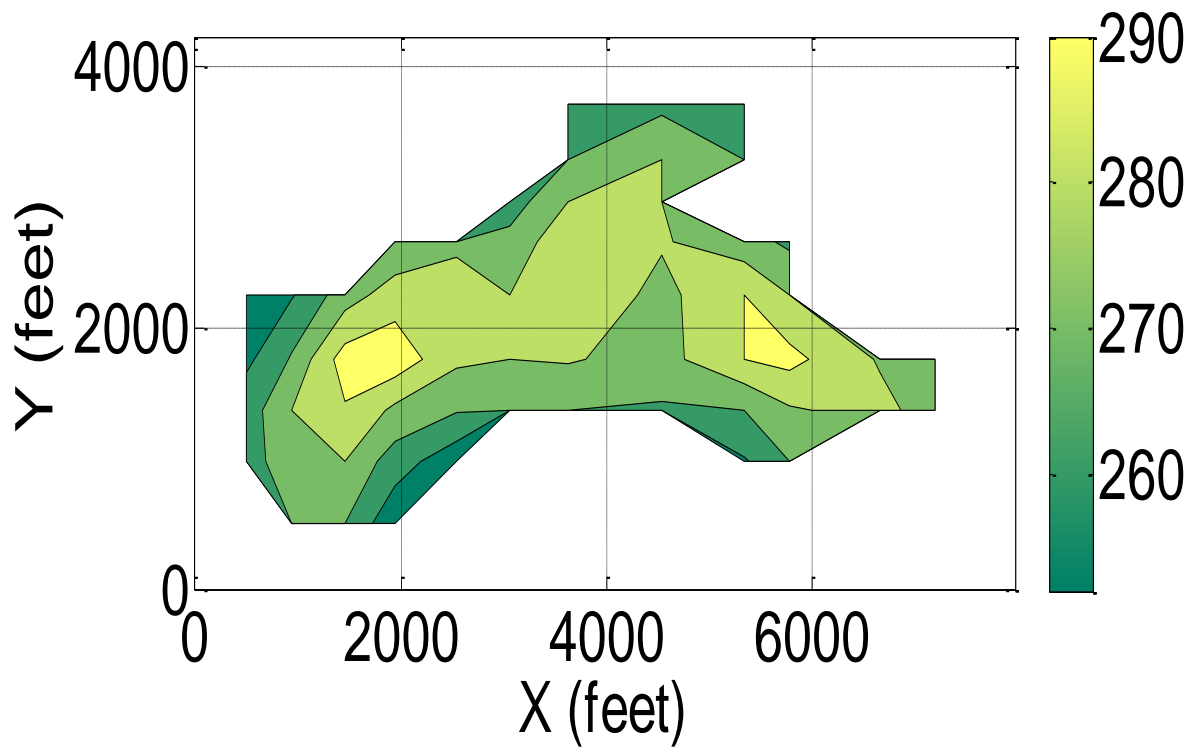
Figure 4. Permeability distribution map for A-1 reservoir (kx direction in md)

The main flow directions are parallel to the southwest-northeast and southeast-northwest directions.
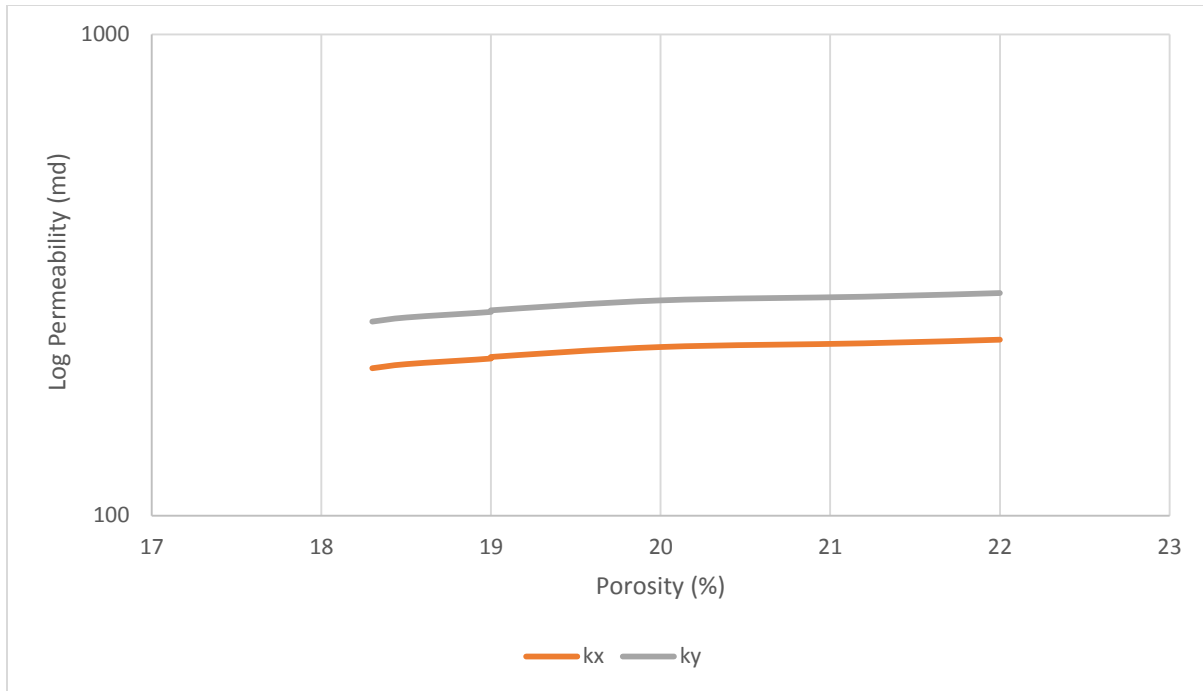
Figure 5. Logarithm of permeability vs porosity plot for A-1 sandstone

Plots of core data reveal a linearly proportional correlation between the logarithm of permeability and core porosity as in **Figure 5**. This is in conformity with the work of Philip [29] depicting a sublitharenite sandstone classification.

3.1.2 Fluid Properties

At reservoir temperature and pressure, oil, water and gas fluids coexist in equilibrium under isothermal conditions and can simultaneously be produced from hydrocarbon reservoirs. In black oil systems, neither oil nor water vaporizes in the gas phase in any significant quantity, but the gas component is most miscible in the oil phase and negligible in the water phase. The gas obtained from a producing reservoir composes of free gas and solution gas with the greater portion of solution gas coming as gas dissolved in oil and to a lesser extent water. Oil phase properties in multiphase flow at reservoir conditions are strongly affected by pressure variation and the amount of gas in solution.

Pressure dependence of fluid properties such as fluid compressibility and gas-compressibility factors, solution gas/oil ratios, fluid densities, fluid formation volume factors (FVF's), fluid viscosities were vital in modeling and characterizing the A-1 reservoir.

The A-1 reservoir has been produced by primary production. The formation produces approximately 50° API gravity oil with no significant Sulphur content. The produced water contains to a greater extent NaCl, and other dissolved cations such as K^+, Ca^{++} and Mg^{++}. Heavy metals such as Ba^{++}, Li^+, Fe^{++} and St^{++} exist in trace amounts. Other anions found in the analysis are $SO_4^{--}, HCO_3^-, CO_3^{--}, NO_3^{--}, B^-, I^-$ and S^{--}. Gas composition by mole fractions for the A-1 formation is presented in the following pie chart.
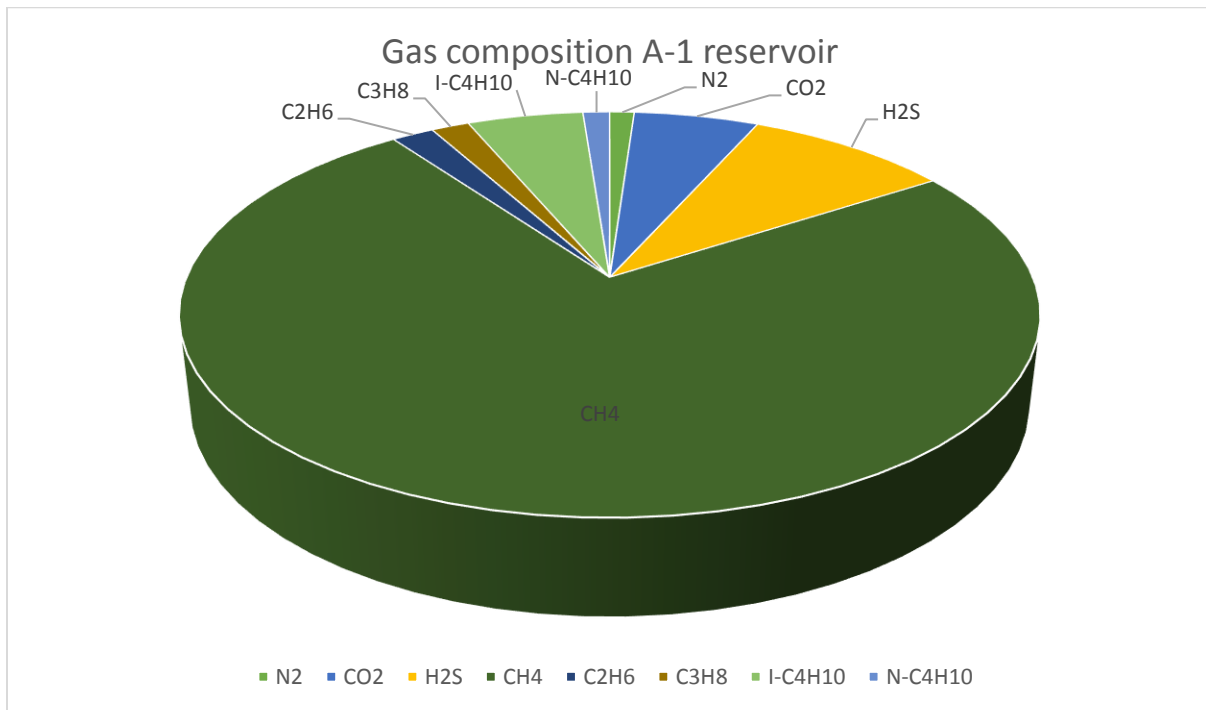
Figure 6. Gas composition for the A-1 reservoir

Three quarters of the A-1 gas was composed of methane gas CH_4 , followed by hydrogen sulfide H_2S, Carbon dioxide CO_2 and butane C_4H_{10} in close competition, with the remaining gases constituting a minute percentage as seen in **Figure 6**.

3.1.2.1   Fluid/Rock Compressibility and Gas Compressibility Factor

Reservoir fluid can be classified as incompressible, slightly compressible or compressible depending on their behavior when exposed to external pressure. In multiphase flow systems, oil and its solution gas is treated as slightly compressible when initial pressure is higher than oil bubble point pressure i.e. ($P > P_b$) and as compressible when reservoir pressure drops below bubble point pressure ($P < P_b$). Water could either be slightly compressible or incompressible while natural gas is strictly a compressible fluid.

Compressibility (c_x) can be defined as the relative volume change in matter relative to a unit change in pressure at constant temperature. It is usually expressed in the following form,

$$c_x = -\frac{1}{\rho}\frac{\partial \rho}{\partial P}|_T \tag{12}$$

where $x = o, w, r \; or \; g$ and $\rho = m/V$.

For the gas phase, gas compressibility may be expressed in another form by substituting the real gas law **Equation 13**, into **Equation 12**,

$$\rho_g = \frac{pM}{zRT} \tag{13}$$

$$c_g = \frac{1}{P} - \frac{1}{z}\frac{\partial z}{\partial p}|_T \tag{14}$$

where M is the molecular weight and R, the gas law constant measured in $J/(g \; mol - K)$

In a reservoir rock where pore space is occupied by oil, water and gas, the total compressibility is evaluated as follows

$$c_t = c_g S_g + c_o S_o + c_w S_w + c_f \tag{15}$$

Values for compressibility of the A-1 reservoir rock and fluid at initial conditions were calculated and reported as follows

Table 2. Fluid and total compressibility values for A-1 reservoir

Compressibility of oil (C_o)	$5 \times 10^{-6} \ psi^{-1}$
Compressibility of water (C_w)	$3 \times 10^{-6} \ psi^{-1}$
Compressibility of gas (C_g)	$1.25 \times 10^{-4} \ psi^{-1}$
Formation compressibility (C_f)	$3 \times 10^{-6} \ psi^{-1}$
Total compressibility (C_t)	$1.68 \times 10^{-5} \ psi^{-1}$

3.1.2.2   Solution-Gas/Liquid Ratio

The volume of gas that must dissolve in a unit volume of liquid at standard conditions for the liquid and gas system to reach equilibrium at reservoir temperature and pressure is referred to as the solution-gas/liquid ratio. There exist two types of solution-gas/liquid ratios in a black-oil reservoir: solution-gas/oil ratio and solution-gas/water ratios. Solution-gas/water ratio is usually assumed zero because of negligible or near zero gas dissolution in water.

During the life cycle of a primary depleted reservoir, the reservoir is initially undersaturated and the initial reservoir pressure decreases everywhere as fluids are extracted from the subsurface beyond the bubble point pressure i.e. $P_b < P < P_i$ and the solution gas-oil ratio R_S remains constant. The first bubble of gas evolves from solution at $P = P_b$ and more gas is produced as pressure drops below bubble point pressure creating the free gas phase. At this point the reservoir is said to be saturated as both oil and gas phases coexist in thermal equilibrium. **Figure 7** is a plot of solution gas/oil ratio for the A-1 reservoir versus pressure. Region A is the saturated oil region and region B is the undersaturated oil region. The A-1 reservoir has an initial pressure of 4800 psi and a bubble point pressure of 5500 psi, since its operational pressure is less than the bubble point pressure, the reservoir is producing in the saturated oil region.

$$P_{b_{A-1,reservoir}} = 5500 \ psi \qquad\qquad (16)$$

$$P_{i_{A-1,reservoir}} = 4800 \; psi$$
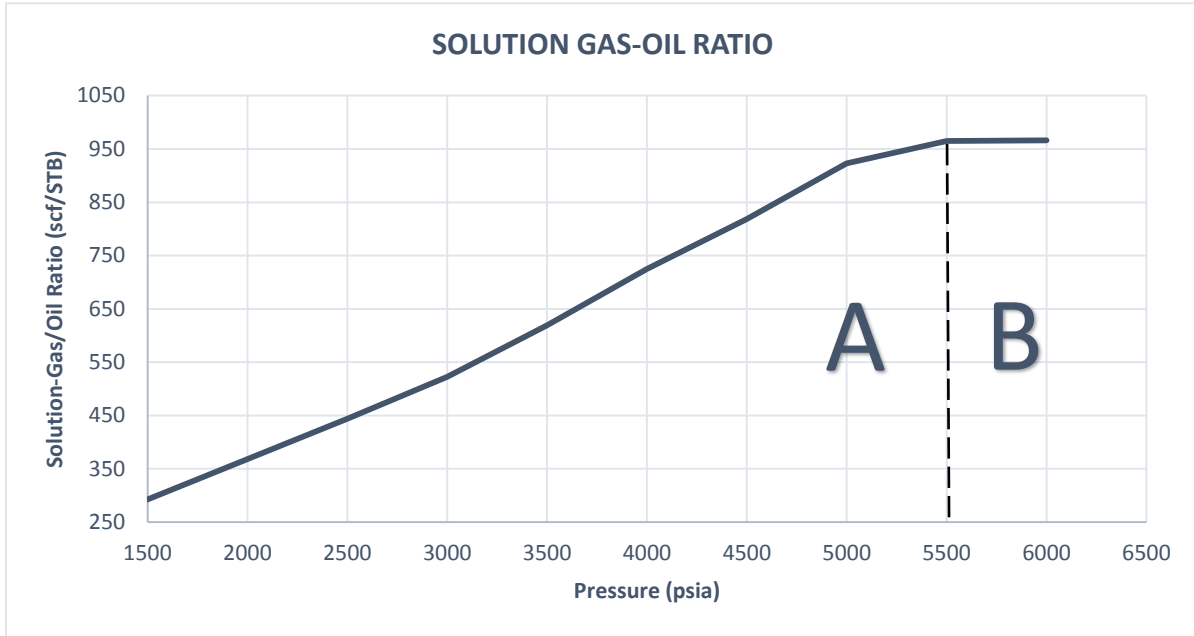
Figure 7. Solution gas-oil ratio for A-1 reservoir

3.1.2.3   Formation Volume Factor (FVF)

According to Boyle's law [30], the pressure and volume of a gas are inversely dependent on each other if the temperature and amount of gas remain unchanged within a closed system [31].

$$P \; \alpha \; \frac{1}{V}$$

(18)

where P is the pressure and V is the volume of the gas.

If the pressure increases, the volume decreases proportionately and vice-versa. Fluid flow occurs in the formation, but oil and gas measurements are conducted at the surface as such formation volume factors (FVF) are used to convert measured surface volumes to reservoir volumes given that there is a pressure variation from the formation to the surface. The FVF of any phase can be

defined as the ratio of the volume that the phase occupies at reservoir pressure and temperature to that at standard conditions.

For slightly compressible fluids, such as water and dead oil, FVF's can be approximated by the following expression

$$B_l = \frac{B_l{}^o}{[1 + c_l(P - P^o)]} \tag{19}$$

for the gas phase, the real gas law is applied at reservoir and standard conditions to obtain

$$B_g = \frac{P_{sc}}{\alpha_c T_{sc}} T \frac{z}{P} \tag{20}$$

where $l = o \; or \; w$, and p^o is the reference pressure usually the initial reservoir pressure or atmospheric pressure. For undersaturated reservoirs ($P > P_b$), FVF of the oil phase is expressed mathematically as

$$B_o = B_{ob}[1 - c_o(P - P_b)] \tag{21}$$

Oil, water and gas FVF's for the A-1 reservoir are shown in the following plots, **Figure 8**.
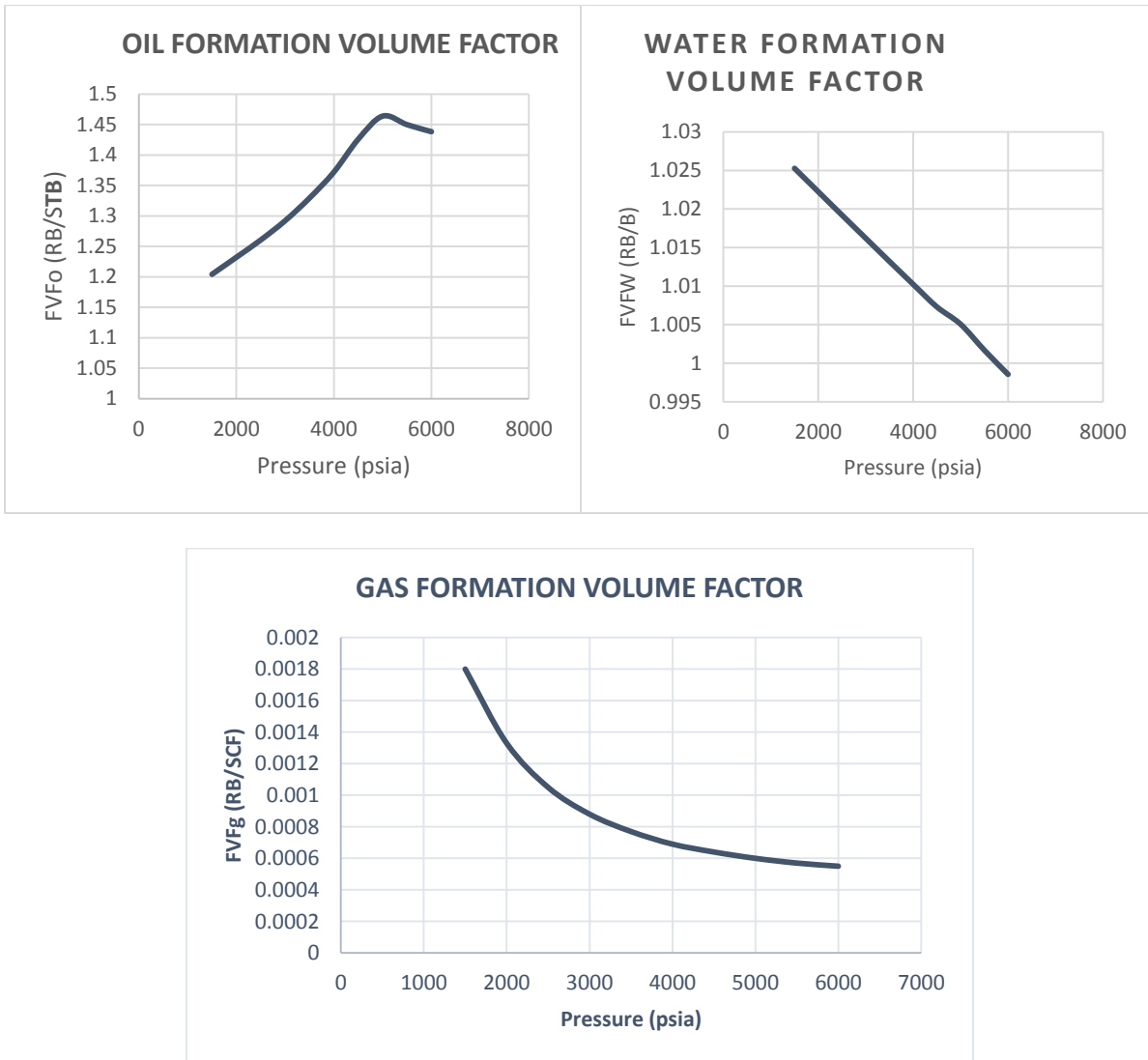
Figure 8. Fluid formation volume factor for A-1 reservoir

Oil FVF increases as pressure decreases in the undersaturated region as a result of expansion of the oil and its solution gas. In the saturated region, as pressure decreases, the oil phase shrinks as it releases free gas resulting in a decrease in the oil FVF, the overall effect is gas evolution dominating oil expansion. Water FVF decreases steadily with increasing pressure in the formation. Gas FVF increases exponentially with decreasing pressures due to the effect of gas evolution.

3.1.2.4   Fluid Density

Density is the ratio of the mass per unit volume of an object. In the oil field, density is typically reported as pounds per barrel (drilling mud). The pressure dependence of density can be approximated mathematically as

$$\rho_w = \frac{\rho_{wsc}}{B_w} \qquad (22)$$

for the water phase, and

$$\rho_g = \frac{\rho_{wsc}}{\alpha_c B_g} \qquad (23)$$

for the gas phase,

If ideal mixing of oil and solution gas is assumed, then oil phase density for both undersaturated and saturated conditions is given by

$$\rho_o = \frac{\rho_{osc} + \rho_{gsc} R_s / \alpha_c}{B_o} \qquad (24)$$

for ($P \leq P_b$) and,

$$\rho_o = \rho_{ob}[1 + c_o(P - P_b)] \qquad (25)$$

for ($P > P_b$). ρ_{ob} , and P_b are the densities and pressures at bubble point respectively.

Plots of fluid density variation with pressure for the A-1 reservoir are shown in **Figure 9**.
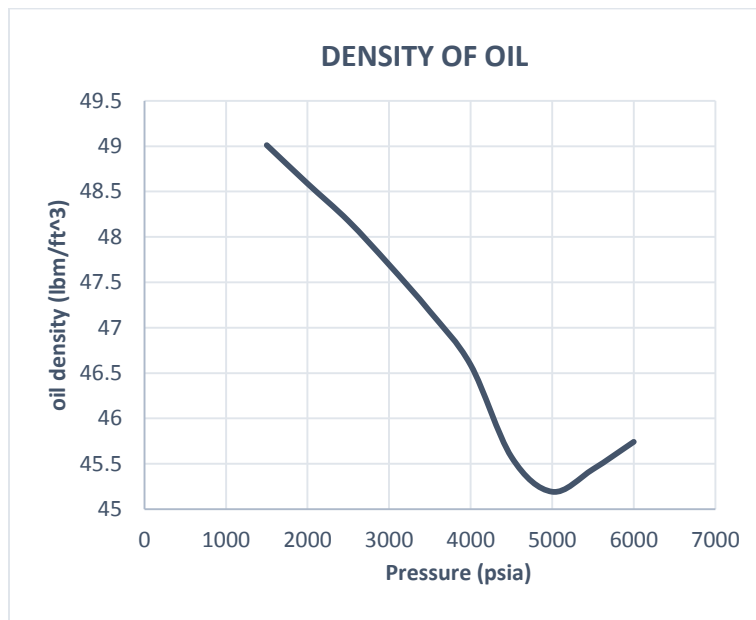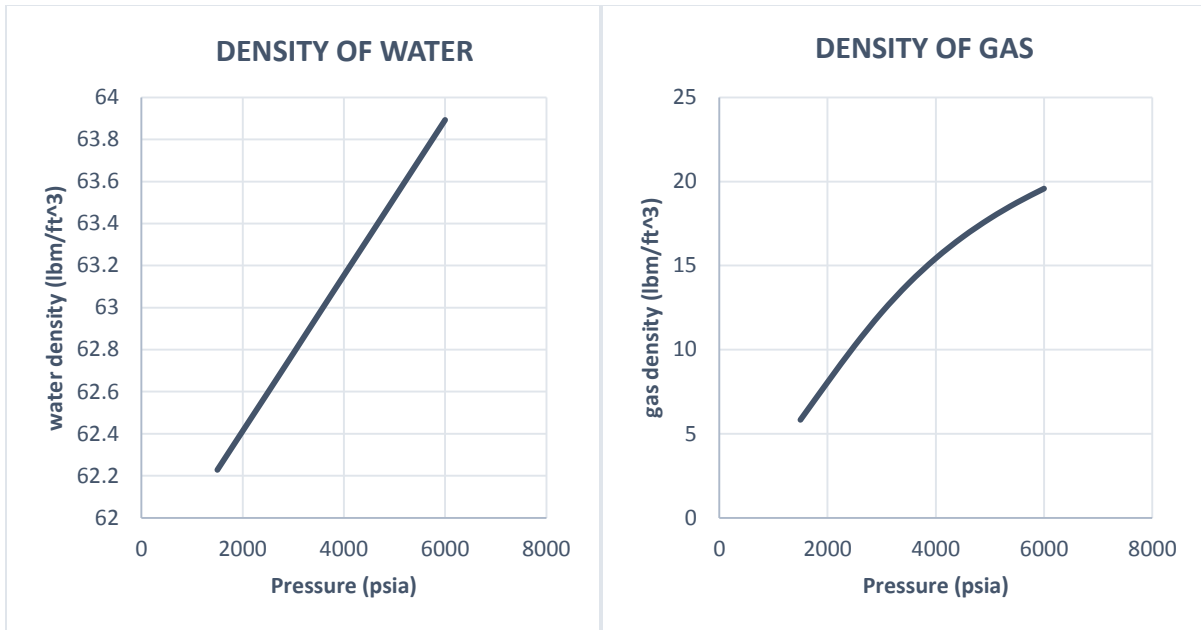
Figure 9. Fluid densities for A-1 formation

The density of water in the A-1 formation increases steeply with increasing pressure, the density of oil increases steeply with decreasing pressure due to gas evolution and oil expansion. Oil density decreases with decreasing pressure up to bubble point. Gas density decreases steadily with decreasing pressure.

3.1.2.5 Fluid Viscosity

A property of fluids that indicates their resistance to flow under an applied pressure gradient, usually reported in centipoise. Fluid viscosity is a function of both temperature and pressure. Reservoir oils are typically dense fluids that offer high resistance to flow because fluid molecules are closer to each other and their random motion retards flow. For isothermal reservoirs we concern ourselves mostly with the pressure dependence of viscosity as seen in **Figure 10** .

Figure 10. Fluid viscosities for A-1 formation

Water is a slightly compressible fluid, as such when pressure increases in the reservoir, its viscosity remains almost constant or increases slightly. Viscosity of dead oil is similar to that of water. Gas is a compressible fluid, therefore as pressure increases, gas viscosity increases but tends to level off at very high pressures. This is due to the fact that at very high pressures gas tends to behave as a liquid.

Oil viscosity dependence on pressure is more involving because it must account for mass transfer between the oil and gas systems. Pressure dependence of viscosity is mostly influenced by the effect of pressure on oil density and solution gas-oil ratio on oil phase dilution. The behavior of viscosity is associated with that of density because density is a measure of the mean free path of liquid and gas molecules and therefore a measure of random molecular motions and interactions that affect viscosity.

As pressure decreases in the saturated region ($P \leq P_b$), gas is being released from the oil phase, as such the oil component and remaining associated solution gas expand to fill created volume. Oil phase viscosity increases as pressure drops due to the overall effect of gas liberation that dominates oil expansion. In the undersaturated oil region ($P > P_b$), oil dilution remains unchanged because R_s is constant and only the oil component density decreases as reservoir pressure drops to bubble point pressure. Oil viscosity in undersaturated region is dependent on bubble point pressure and can be expressed mathematically as

$$\mu_o = \frac{\mu_{ob}}{[1 - c_u(P - P_b)]} \tag{26}$$

where μ_{ob} is the oil viscosity at bubble is point pressure and c_u is a constant that depends on the solution gas oil ratio at bubble point pressure. Oil phase viscosity calculated from **Equation 26,** should decrease as pressure decreases. For the A-1 reservoir only a very slight decrease in viscosity is observed as pressure drops to bubble point.

3.1.3　Rock/Fluid Properties

3.1.3.1　　Fluid Saturation

In three-phase flow systems, fluid saturation is the relative amount of water, oil and gas present in the pores of a rock, usually expressed as a percentage of pore volume. The wetting phase adheres to the walls of the solid rock and fills the fine pores; the non-wetting phase occupies the center of the large pores while the remaining phase fills the space left unoccupied by the other two phases. The pore volume must always be filled by the fluids present thus a general volume balance for the three phases are related by the following constraint equation.

$$S_o + S_w + S_g = 1 \tag{27}$$

At an initial pressure of 4800 psi, the oil, water and gas saturations used in the simulator for the A-1 reservoir are reported as follows

Table 3. Initial phase saturations for A-1 reservoir

S_{oi}	0.5
S_{wi}	0.42
S_{gi}	0.08

3.1.3.2　　Relative Permeability

Relative permeability is a measure of a rock's capacity to transmit any phase through its pores. Relative permeability in the three phase flow of oil, water and gas systems can be estimated from data gotten from two phase flow systems using the Stone's three phase model II with the assumption that water is the wetting phase, gas is the non-wetting phase and oil is the intermediate phase in the three phase system. Stone's second model is a probability model based on channel flow considerations used in approximating three-phase relative permeability from two-phase relative permeability data sets. Unlike Stone's first model, this model does not require the knowledge of residual oil saturation S_{or} . However, it is concluded that the normalized Method I

with the recommended form of S_{or} is superior to Method II as the latter tends to under predict relative permeability [32]. Stone's second Model is stated in **Equations (28, 29 and 30,**

$$k_{rw} = f(S_w) \tag{28}$$

for the water phase,

$$k_{rg} = f(S_g) \tag{29}$$

for the gas phase and,

$$k_{ro} = k_{rocw} \left[\left(\frac{k_{row}}{k_{rocw}} + k_{rw} \right) \left(\frac{k_{rog}}{k_{rocw}} + k_{rg} \right) - \left(k_{rw} + k_{rg} \right) \right] \tag{30}$$

for the oil phase.

k_{row} and k_{rw} , are obtained from two-phase oil/ water data at a given S_w and k_{rog} and k_{rg} are obtained from two-phase oil/water data at a given S_g in the presence of irreducible water. k_{rocw} is the relative permeability to oil k_{row} at irreducible water saturation ($S_w = S_{wi}$) or relative permeability to oil k_{rog} at ($S_g = 0$).

In a water-wet system, phase relative permeability is strictly a function of phase saturation. Oil/water relative permeability and gas/oil relative permeability curves used in A-1 simulation project are shown in **Figure 11 and 12**.
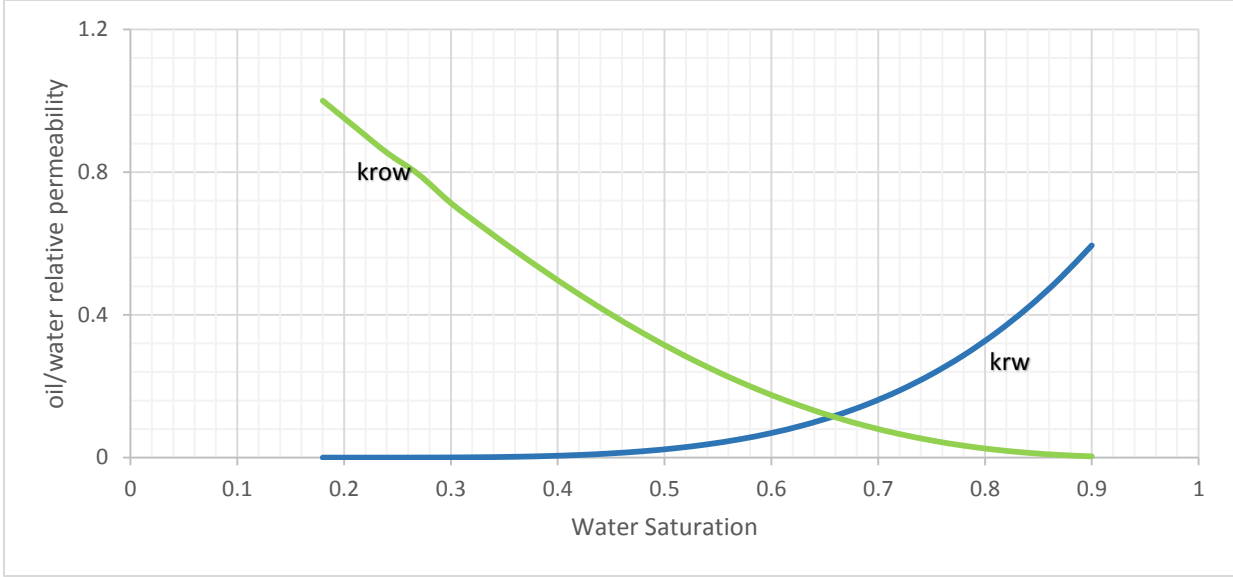
Figure 11. Oil-water relative permeability curve used in simulation study (typical of a completely water wet system)
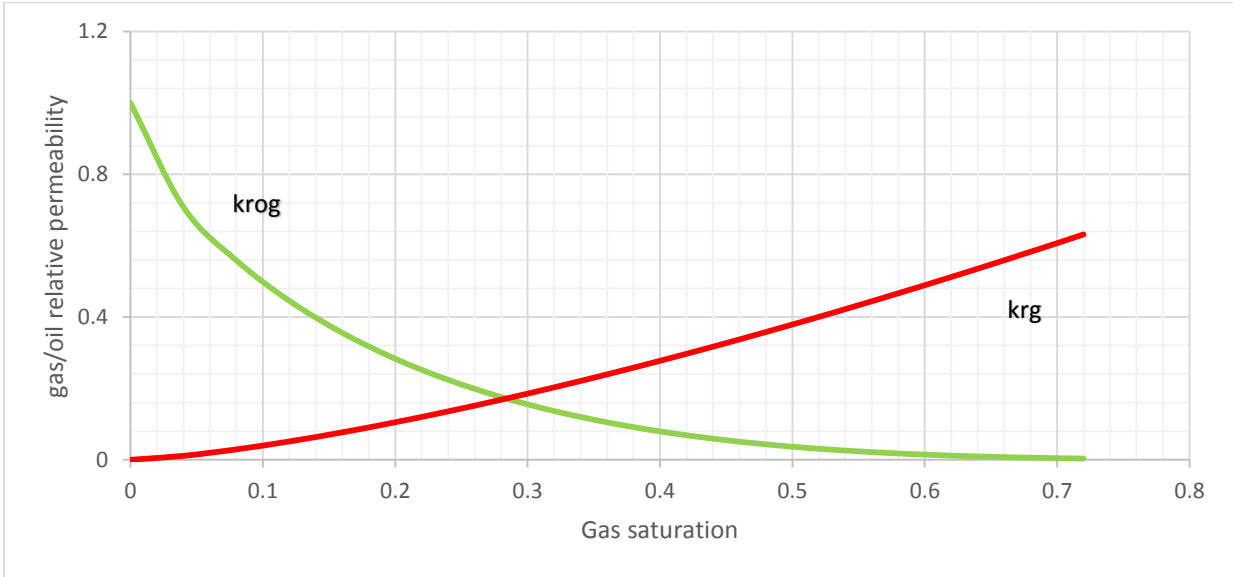
Figure 12. Gas-oil relative permeability curve used in simulation study (typical of a completely water wet system).

3.1.3.3   Capillary Pressure

When two or more mobile phases coexist in the pore throat sizes of a reservoir rock, a pressure difference is created between any two phases across the interphase. This pressure difference (capillary pressure) is a function of saturation and saturation history for a given reservoir rock and fluids at constant temperature and composition. In the presence of gas, (oil or water) always wets the rock. Capillary pressure is equally defined as the pressure of the non-wetting phase minus the pressure of the wetting phase. In which case it is expressed mathematically as

$$P_{cow} = f(S_w) = P_o - P_w \tag{31}$$

for a two phase oil/water system in a water-wet rock, and

$$P_{cgo} = f(S_g) = P_g - P_o \tag{32}$$

for a two-phase gas/oil system.

Due to the experimental complexity and the large amount of data required to define three phase capillary pressure and relative permeability relationships, Leverett and Lewis established in 1941 that capillary pressures derived from two-phase systems could be used in three phase flow problems [33, 34]. This allows three-phase simulation to be made based upon conventionally measured imbibition and drainage data. However in a three phase system, flow cannot be described simply as "imbibition" or "drainage" but rather as "drainage/drainage", "drainage/imbibition" or "imbibition/imbibition" to account for the change in saturation in all three phases [34]. Capillary pressure curves are important for understanding saturation distribution in the reservoir and how it affects imbibition and multiphase fluid flow through the rock. Capillary pressure curves from two phase systems used in solving the A-1 three phase reservoir problem are shown in **Figure 13.**
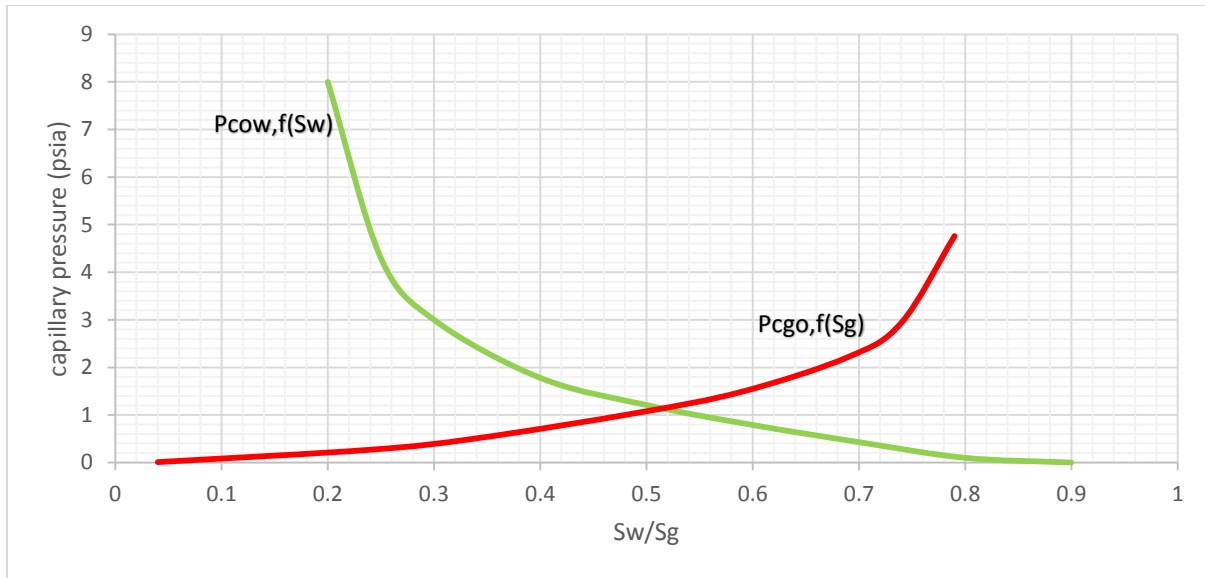
Figure 13. Capillary pressure curves used in simulation study (typical of a completely water wet system).

3.1.4 Structure and Topography

Oil and natural gas production from the state of Colorado has been a large contributor to the economy and the industry as a whole. The analysis of the A-1 Reservoir in Plum Bush Creek field situated approximately sixty miles east of Denver provides an overview of the future potential and historical productivity of the field. Plum Bush Creek field is located on the gentle west-dipping east flank of Denver Basin making it an ideal field for hydrocarbon accumulation. The field was discovered by Kimbark Co., Ltd and Sterling Drilling Co. The A-1 reservoir is a gentle west dipping Dakota sandstone reservoir of Cretaceous age. The geometry of the reservoir rock is that of a channel sand and the trapping mechanism is a permeability pinch out undip on a slight structural nose. Primary production occurs within three separate benches of the 'J' sand in the field, most specifically from the first and third benches in the northeastern part of the field and the first and second benches in the southwest part of the field. The total productive area was roughly 1920 acres.
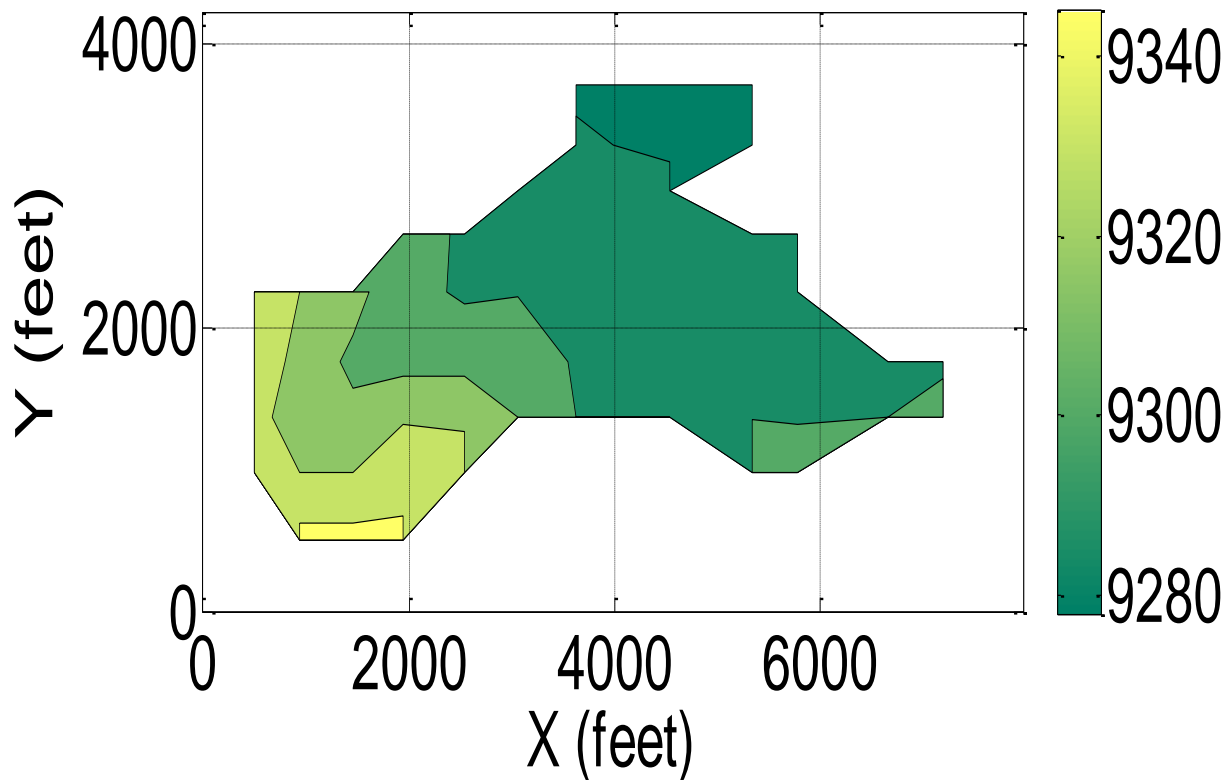
Figure 14. Structural contour map revealing subsea surface that is dipping towards the westward potion of the field (A-1 reservoir).

Structure maps of the A-1 reservoir reveals a surface that is dipping towards the westward portion of the field and a formation depth ranging from 9280 feet to about 9350 feet in southeastern portion upwards as seen in **Figure 14 and 15**. The maximum elevation difference within the structure is approximately 60 feet, which translates to a drop of approximately 1 foot every 100 feet. Initial formation pressure of 4800 psi is measured at a reference depth of 9290 feet. Structural cross-sections along the longitudinal axis and along the west axis are shown below.
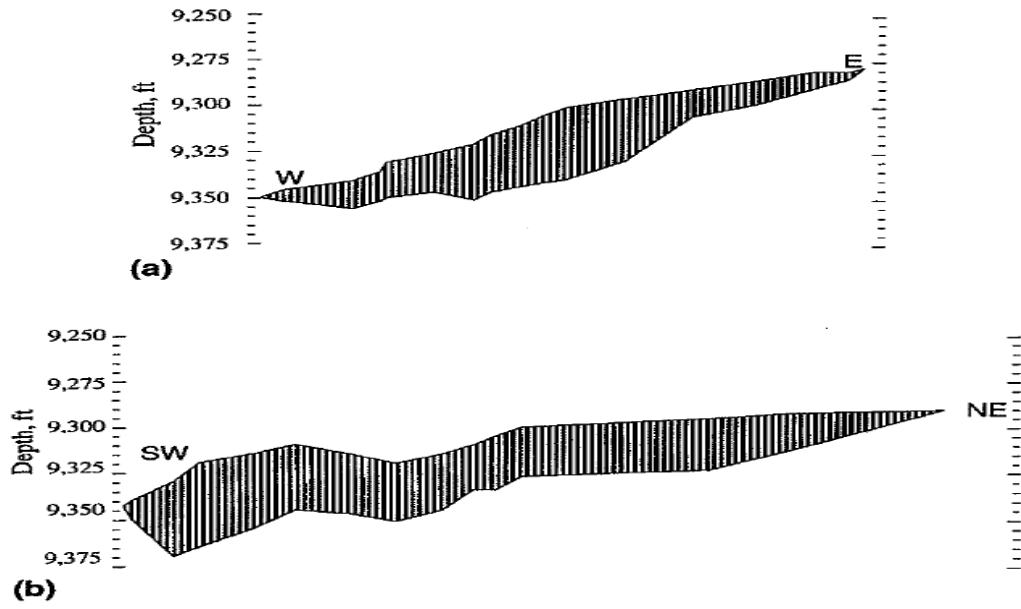
Figure 15. Structural cross-sections for the A-1 reservoir: (a) west-east and (b) southwest-northeast [27]
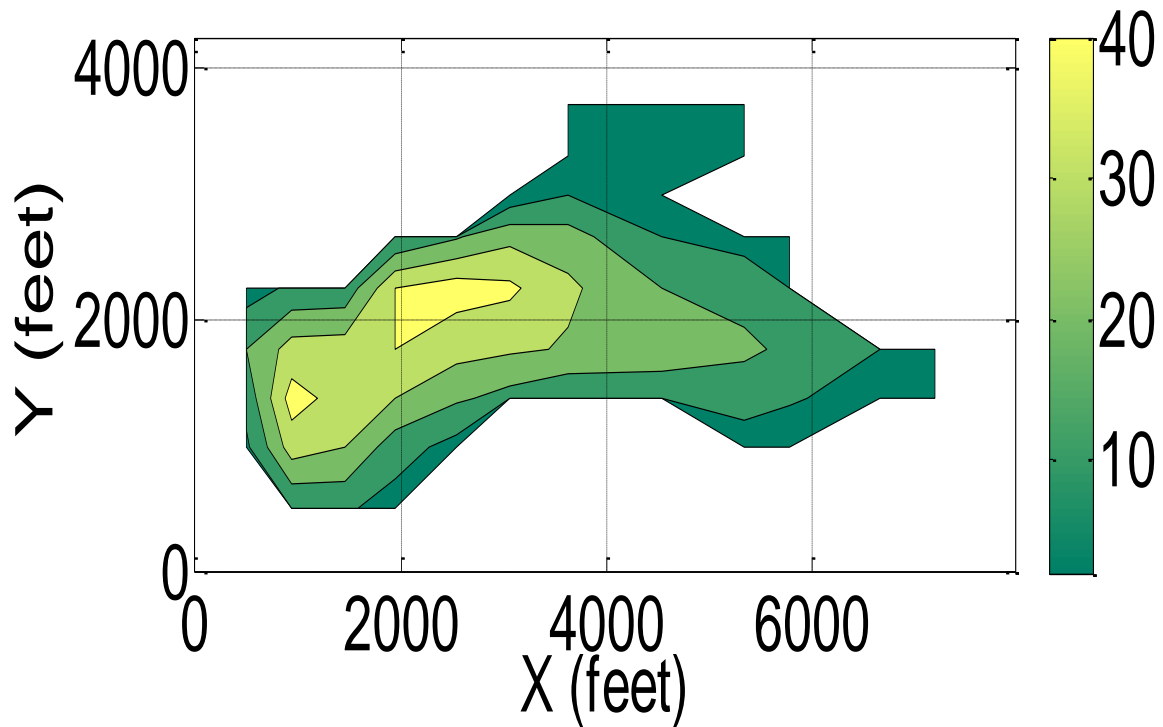
Figure 16. Net pay thickness map (thinning from southwest to eastern portions)

The thickest section of the reservoir is seen in the southwestern portion and is approximately 44 feet thick as seen in **Figure 16**. The average net pay thickness is 20 feet and the reservoir thins from the center portion outwards.

3.1.5 Physical and Mathematical Modeling of Multiphase Flow

3.1.5.1   Reservoir Discretization

The A-1 reservoir is modelled as a 2D reservoir using non-uniform block centered grids in Cartesian coordinates where the distance between block boundaries is the defining variable in space. Here the grid block dimensions are selected first followed by the placement of points in central locations of the block. The rectangular coordinate system is defined in such a manner that the x and y directions of the coordinate system are placed parallel with the principal flow directions which are the southwest-northeast and southeast-northwest directions respectively. As such the four component permeability tensor in $2d$ space is approximated with a permeability vector in two entries $(k_x \text{ and } k_y)$, the smallest and largest permeability values as y and x respectively. The y-directional permeabilities are assigned 80% of the x-directional permeability values. Depths to formation tops of grid blocks are reported as positive downward from sea level.

To ensure continuity of the major gridlines in the gird system, Δx values along each column of blocks and Δy values along each row of blocks are kept uniform. However, Δx and Δy values are allowed to vary along the x and y-directions respectively as seen in **Figure 17** . Grid dimensions of Δx and Δy are related to the boundaries by

$$\Delta x_i = x_{i+1/2} - x_{i-1/2} \tag{33}$$

$$\Delta y_j = y_{j+1/2} - y_{j-1/2} \tag{34}$$
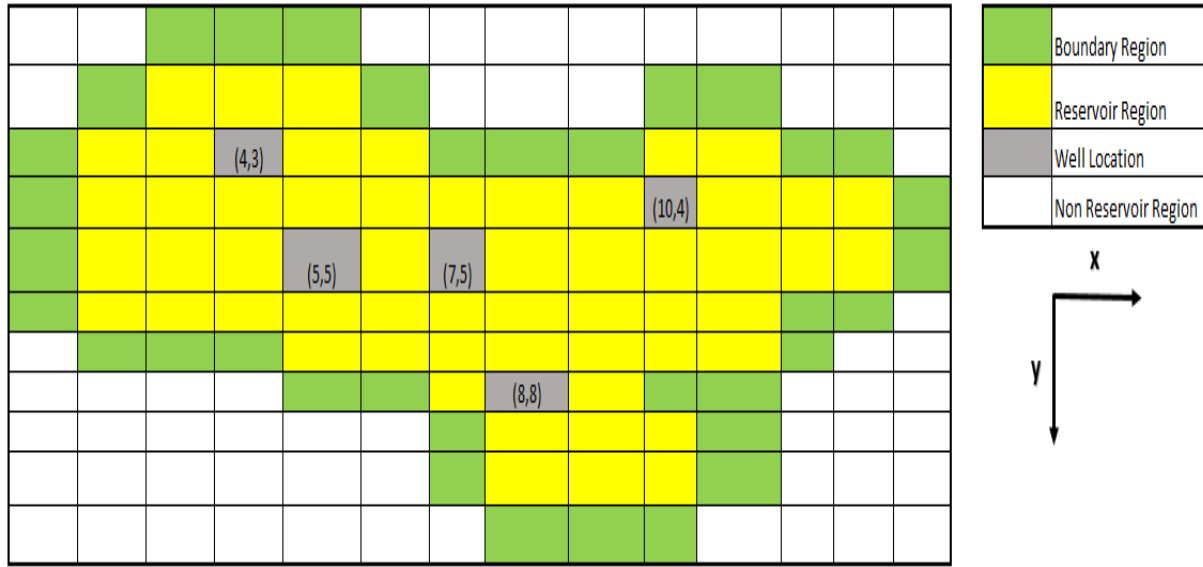
Figure 17. Finite difference grid showing the partitioning of the different regions in the reservoir

Multiphase flow equations are written using Control volume finite difference (CVFD) terminology. This method is advantageous in that, it is applicable to grid blocks of any geometry and addresses the treatment of known flow rates through external and internal boundaries in the model.

3.1.5.2   Darcy's Law in Multiphase Flow

Darcy's law was formulated by henry Darcy based on the results of experiments on the flow of water through beds of sand. It is a simple proportional relationship between the instantaneous discharge rate through a porous medium, the viscosity of the fluid and the pressure drop over a given distance [35].

The fluid volumetric velocity of phase $p = o, w$ or g from block $i-1$ to block i is given by

$$Q_{px}|_{x_{i-1/2}} = \beta_c \frac{(k_x k_{rp})|_{x_{i-1/2}}}{\mu_p|_{x_{i-1/2}}} \left[\frac{\Phi_{p_{i-1}} - \Phi_{p_i}}{\Delta_{x_{i-1/2}}}\right] \tag{35}$$

where φ is the potential difference between block $i-1$ and block i is expressed as

$$\Phi_{w_{i-1}} - \Phi_{w_i} = \left(P_{w_{i-1}} - P_{w_i}\right) - y_{w_{i-\frac{1}{2}}}(Z_{i-1} - Z_i) - \left(P_{cwo_{i-1}} - P_{cwo_i}\right) \tag{36}$$

$$\Phi_{o_{i-1}} - \Phi_{o_i} = \left(P_{o_{i-1}} - P_{o_i}\right) - y_{o_{i-\frac{1}{2}}}(Z_{i-1} - Z_i) \tag{37}$$

$$\Phi_{g_{i-1}} - \Phi_{g_i} = \left(P_{g_{i-1}} - P_{g_i}\right) - y_{g_{i-\frac{1}{2}}}(Z_{i-1} - Z_i) + \left(P_{cgo_{i-1}} - P_{go_i}\right) \tag{38}$$

for $p = o, w$ or g and P_C is the capillary pressure between oil/water and oil/gas system.

3.1.5.3 Mass Conservation in Multiphase System

The law of conservation of mass is a material balance equation written for any component of flow (oil, water or gas) in a control volume of the system under consideration **Figure 18**. The mass accumulated (m_a) equals the mass of excess material stored in or depleted from the control volume over a given time interval and can be expressed mathematically as

$$m_{\left(x-\frac{\Delta x}{2}\right)} - m_{\left(x+\frac{\Delta x}{2}\right)} + m_{\left(y+\frac{\Delta y}{2}\right)} - m_{\left(y-\frac{\Delta y}{2}\right)} - m_s = m_a \tag{39}$$

where m_s is the mass of the component entering or leaving the control volume externally (through wells). For a mass rate of q_m entering the control volume through a well in a defined time interval Δt, the above equation can be rewritten in terms of mass rates (w) of components ($o, w, fg,$ or sg), mass of fluid contained in a unit volume of reservoir (m_s) , phase densities (ρ_p) , porosity Φ and bulk volume V_b as

$$w_{|x-\frac{\Delta x}{2}}\Delta t - w_{|x+\frac{\Delta x}{2}}\Delta t \; w_{|y-\frac{\Delta y}{2}}\Delta t - w_{|y+\frac{\Delta y}{2}}\Delta t - q_m\Delta t$$
$$= \rho_p * \Phi * V_b(|_{t+\Delta t} - m_v|_t) \tag{40}$$

3.1.5.4   Diffusivity Equation

If we assume horizontal flow and neglect gravitational forces, for the control volume defined in **Figure 18**, when the limits are $\Delta x, \Delta y, \Delta t \;\rightarrow\; 0$, potential gradients $(\frac{\partial \Phi}{\partial i})$ could be replaced with the pressure gradients $(\frac{\partial P}{\partial i})$ in the culmination of the above equations and the resulting diffusivity equation for multiphase flow in porous $2D$ reservoirs is expressed as

$$\frac{\delta^2 P}{(\Delta y)^2} + \frac{\delta^2 P}{(\Delta x)^2} = \Phi \frac{c_t}{\lambda_t} \frac{\partial P}{\partial t} \tag{41}$$

This expression is valid if the fluid compressibility is small and remains constant within pressure range of interest. $C_t \; and \; \lambda_t$ are the total compressibility and mobility ratios respectively.
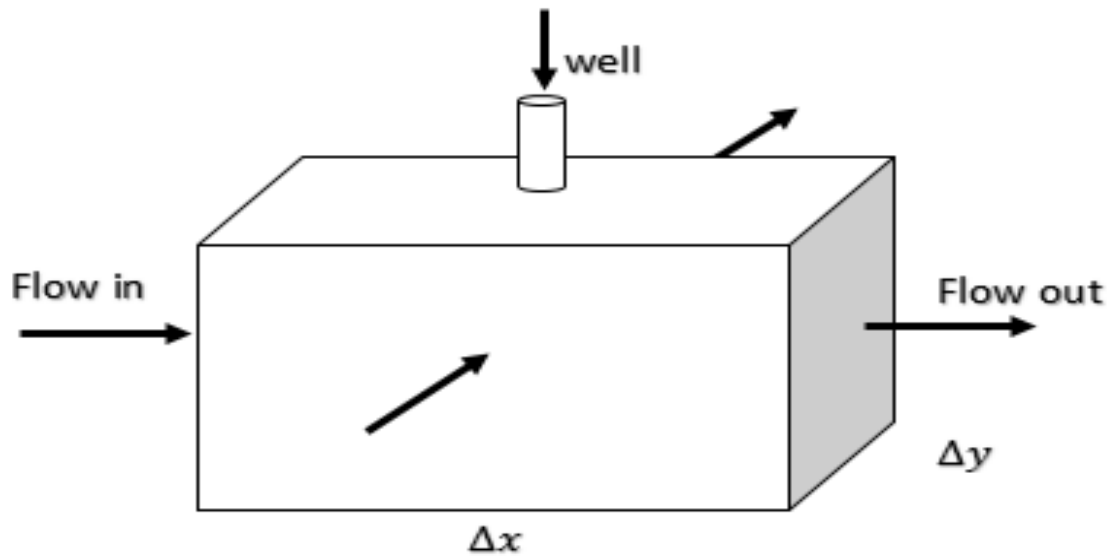
Figure 18. Control volume showing mass balance in a reservoir system

The external source/sink (well) term denotes production/injection into the reservoir. Arrows indicate mass flow in and out of block.

3.1.5.5   Convergence of the Diffusivity Equation

The Von Neumann stability analysis can be used in determining the condition for stability in the explicit solution of a PDE. **Equation 41** can be expressed in terms of $M_{tt}, M_{xxxx}, and\ M_{yyyy}$. The proof of convergence is established as

$$E^n \leq [\frac{1}{2}\Delta t\ M_{tt} + \frac{1}{12}b((\Delta x)^2 M_{xxxx} + (\Delta y)^2 M_{yyyy}]t_F$$

(42)

provided the mesh sizes satisfy the condition

$$\mu_x + \mu_y \ \leq\ \frac{1}{2}$$

(43)

where M_t and $M_{x,y}$ are partial derivatives in time and space, $\mu_x = \frac{b_x \Delta t}{(\Delta x)^2}$ $\mu_y = \frac{b_y \Delta t}{(\Delta y)^2}$ and $b = \frac{\Lambda_t}{\Phi c_t}$

Δx , Δy are typically the smallest grid sizes in a grid system of variable block sizes. If the solution is stable for the smallest block size, it will be stable for all other block sizes.

3.1.6 Simulator Development

The variables of interests are divide into three categories;

3.1.6.1   **Assumptions:**

The major assumptions in this three phase flow model concerns the fluid properties. We assume the following to simplify our flow equations and reduce computational time

- No flow in the third dimension
- Isothermal reservoir
- Laminar flow, Darcy's law is applicable
- No mass exchange between phases

- Phase pressures and saturations are characterized by a single value initially.
- Phase relative permeability and capillary pressures are solely a function of the saturation of that phase.

3.1.6.2   Input Data:

The input data required for a three-phase simulation include: grid dimensions, formation tops, reservoir thickness, porosity and permeability maps, initial conditions, compressibility values, PVT tables, reservoir and non-reservoir grid assignments and well specifications. All these are coupled with the simulator as .m files in MATLAB.

3.1.6.3   Output Data:

Output data obtained from the three-phase reservoir simulator are of two types. Well data (flow rates, cumulative production curves and material balance checks) and reservoir data (porosity, pressure and saturation distribution maps).

3.1.6.4   Program Description

This Three-Phase reservoir simulator is written in MATLAB. MATLAB is a high performance language that integrates computation, visualization and programming in a user friendly environment from a mathematical model [12]. A computer program is written to simulate three immiscible phases in a two-dimensional geometry of a heterogeneous and anisotropic reservoir producing under solution gas/water drive mechanisms. Using a scripting language such as MATLAB to provide the input data, process grids and solve iteratively for pressure has an edge over commercial simulators in that it allows the user access to all the stages of the simulation process and a proper understanding of the physics of fluid flow. A system of finite difference equations are used to approximate a numerical solution to the differential equations governing multiphase flow for simplicity. Reservoir rock/fluid properties are represented as two-dimensional arrays of 154 blocks. Each block within the array is assigned reservoir and fluid properties that are constants or a function of pressure and saturation changing with time. Reservoir properties can be varied with position, making the gridding system quite flexible. Five producing wells were assigned to this system, and well dimensions are limited to a single grid block. External boundaries

to this reservoir were treated as impermeable barriers and modelled with zero transmissibility. Transmissibility within the reservoir was calculated from averaged fluid properties across neighboring grids with the exception of grids closest to the external boundaries. Directional transmissibility values calculated were assigned to matrix coefficients W, E, N, S, C for the west $(i, j - 1)$, east $(i, j + 1)$ north $(i + 1, j)$ south $(i - 1, j)$ and center (i, j) positions respectively. Initial conditions and reservoir properties were coupled with the simulator through a Properties2d.m file. This model simulates the effect of relative permeability, capillary pressures, viscosity, gravity, fluid/rock compressibility and gas solubility on reservoir performance. The matrix equation $Ax = b$, generated from the multiphase flow **Equations** $51, 52,$ **and** 53 , is solved iteratively for pressures and saturations using GMRES solver. Since the solutions to the difference equations are obtained iteratively, accelerated parameters are used to improve convergence to the correct solutions. Linear interpolation of non-linear properties using look-up tables are calculated in a separate subroutine of the simulator. The A matrix is passed the coefficients W, N, S, E and C and the b matrix to the coefficient Q that represents the right hand side (RHS) terms of the multiphase flow **Equation 62**. The x matrix is solved implicitly for pressures at the next time step $(n + 1)$. The pressure values obtained are then used to solve explicitly for saturations values.

$$\begin{bmatrix} N & \cdots & E \\ \vdots & C & \vdots \\ W & \cdots & S \end{bmatrix} . P^{n+1} = Q \qquad (44)$$

Where N, W, E, C and S are the coefficients of the A matrix, Q is the coefficient of the b matrix and P^{n+1} are the explicit pressure values generated from solving the x matrix.

The methods applied to the simulator can be summarized in the following flowchart, **Figure 19**.

Multiphase formulation

Non linear PDE'S

Non linear Algebraic equations

linearization

Discretization

linear Algebraic equations

Iterations :
$dt = 0.5\ day$
$\Delta P < 0.01psi$

$$Ax = b$$

Solver

Implicit Pressures, Explicit Saturation values and Flow rates

Validation and Application
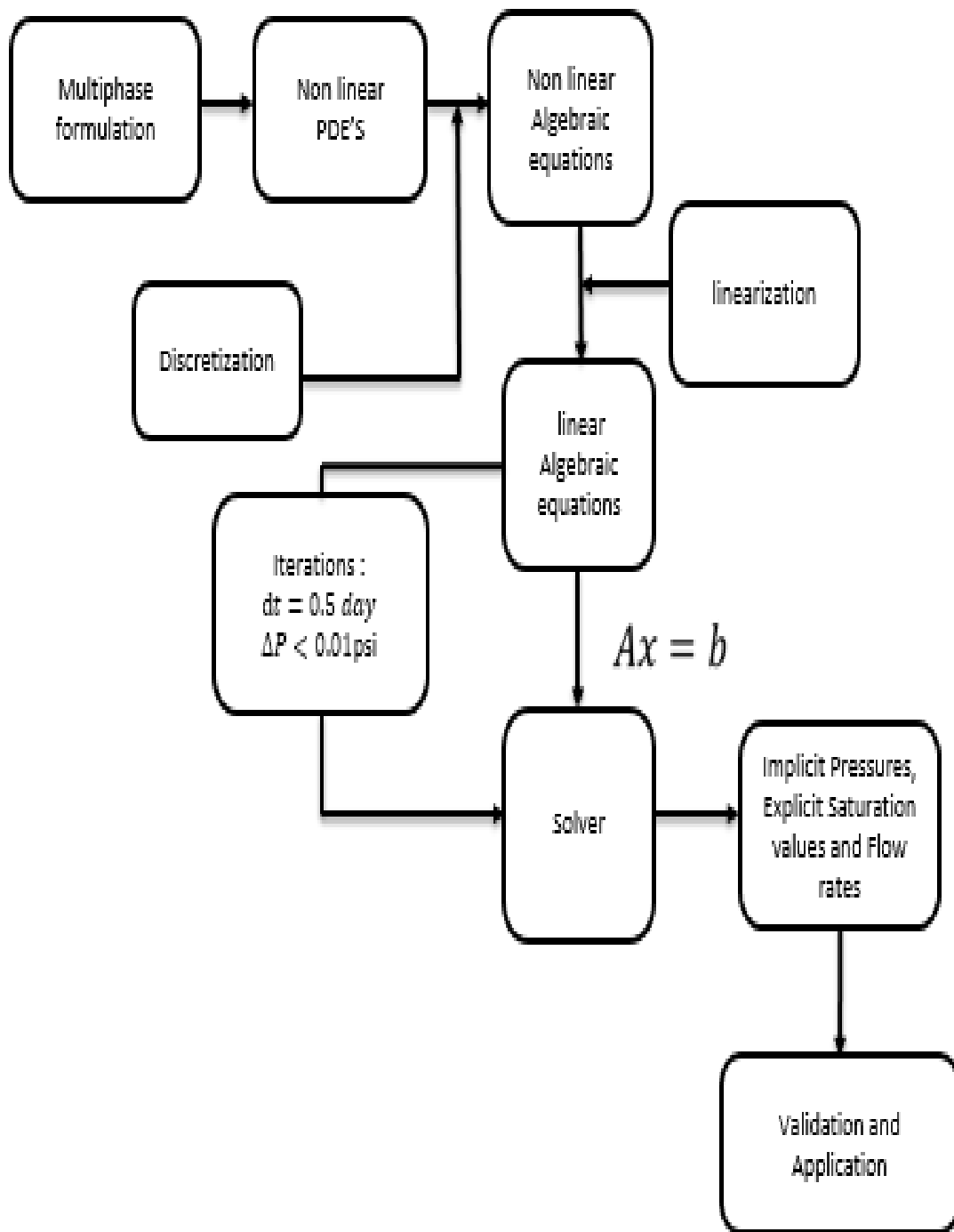
Figure 19. Program flow chart used in the development of black oil simulator

3.1.6.5 Transmissibility Calculations

Transmissibility is the measure of the conductivity of the formation corrected for the viscosity of the flowing fluid. Inter-block transmissibility for the A-1 formation are calculated from the following equations in the x and y directions

$$T_{lx_{i\pm1/2,j}} = G_{lx_{i\pm\frac{1}{2},j}} \left(\frac{k_{rl}}{\mu_l B_l}\right)_{i\pm1/2,j} \tag{45}$$

$$T_{ly_{i,j\pm1/2}} = G_{ly_{i,j\pm1/2}} \left(\frac{k_{rl}}{\mu_l B_l}\right)_{i,j\pm1/2} \tag{46}$$

Where the geometric factor G_l for anisotropic porous media is the pressure-independent term calculated as the harmonic average of area, permeability and grid block sizes of neighboring adjacent blocks.

$$G_{lx_{i\pm\frac{1}{2},j}} = \left(\frac{k_x A_x}{\Delta x}\right)_{i\pm1/2,j} = \frac{2A_{x_{i,j}} A_{x_{i\pm1,j}} k_{x_{i,j}} k_{x_{i\pm1,j}}}{A_{x_{i,j}} k_{x_{i,j}} \Delta x_{i\pm1,j} + A_{x_{i\pm1,j}} k_{x_{i\pm1,j}} \Delta x_{i,j}} \tag{47}$$

$$G_{ly_{i,j\pm\frac{1}{2}}} = \left(\frac{k_y A_y}{\Delta y}\right)_{i,j\pm1/2} = \frac{2A_{y_{i,j}} A_{y_{i,j\pm1}} k_{y_{i,j}} k_{y_{i,j\pm1}}}{A_{y_{i,j}} k_{y_{i,j}} \Delta y_{i,j\pm1} + A_{y_{i,j\pm1}} k_{y_{i,j\pm1}} \Delta y_{i,j}} \tag{48}$$

Transmissibility is set to zero for non- reservoir regions. Phase flow potential differences $\Delta\phi_l$ defined in **Equations 36, 37 and 38** are used in determining the direction of flow and allocating the appropriate fluid properties to grid blocks. Pressures and saturations are calculated at the interior of the grid blocks but transmissibility terms are evaluated at the grid block boundaries. For more accurate results, we must average the pressure dependent and saturation dependent properties between adjacent grid blocks. Single-point upstream weighting is used to calculate strong (f_s) and weak (f_p) nonlinearities in the flow terms that arise from the saturation dependent properties and pressure dependent properties respectively in the flow equations for a given block respectively. If $\Delta\phi_{l_{i+1/2,j}} \geq 0$, flow of phase l is from the upstream grid block ($i + 1, j$) to the downstream grid

block (i,j). If $\Delta \varphi_{l_{i+1/2,j}} < 0$, flow of phase l is from the downstream grid block (i,j) to the upstream grid block $(i+1,j)$. Allocation of pressure and saturation dependent fluid properties can be summarized as follows;

$$f_p, f_{s_{i+1/2}} = \begin{cases} f_p, f_{s_{i+1}} \ if \ \Delta \varphi_{l_{i+1,j}} \geq 0 \\ f_p, f_{s_i} \ if \ \Delta \varphi_{l_{i+1}} < 0 \end{cases}$$

(49)

where $f_p = \frac{Rs,y_l}{\mu_l B_l}$ and $f_s = (k_{rl}, P_{cl})$ are representing pressure and saturation dependent terms respectively.

3.1.6.6 IMPES Method for Three-Phase Black-Oil Model

The equations governing phase flow in a reservoir result from the combination of Darcy's law and mass conservation equation for that phase, generally expressed in the form

$$\nabla \bullet \left[\frac{kk_r}{B\mu} (\nabla p - \rho g \nabla D) \right] = \frac{\partial}{\partial t} \left(\phi \frac{S}{B} \right) - q$$

(50)

This equation is applicable for the oil and water phase. For the gas phase an extra term for gas solubility in oil (R_s) is included.

Implicit-pressure-explicit-saturation (IMPES) methods are used in solving linearized multiphase equations. This formulation treats inter-block flow rates implicitly in pressure, but explicitly in saturations and compositions. The simulator used the IMPES formulation with non-linear terms calculated at time level $(n + \frac{1}{2})$. For explicitly defined transmissibility, flow rates, capillary pressures, fluid gravities and coefficients of pressure difference in the well production rates, the finite difference expressions of **Equation 50** for grid block (n) and it's four neighbors (m) are expressed as in **Equations 51, 52, and 53**

$$\sum_{m \in \varphi n} [T_{o_{n,m}}^n (\Delta_m P_o^{n+1} - y_{o_{n,m}}^n \Delta_m Z)]$$
$$= C_{op_n} \Delta_t P_{o_n} + C_{ow_n} \Delta_t S_{w_n} + C_{og_n} \Delta_t S_{g_n} - q_{osc_n}^n$$

(51)

$$\sum_{m \in \varphi n} [T_{w\,n,m}^{\,n}(\Delta_m P_o^{n+1} - \Delta_m P_{cow}^n - yw_{\,n,m}^{\,n}\Delta_m Z)]$$

$$= C_{wp_n}\Delta_t P_{o_n} + C_{ww_n}\Delta_t S_{w_n} + C_{wg_n}\Delta_t S_{g_n} - q_{wsc_n}^n \tag{52}$$

$$\sum_{m \in \varphi n} [T_{g\,n,m}^{\,n}(\Delta_m P_o^{n+1} + \Delta_m P_{cgo}^n - yg_{\,n,m}^{\,n}\Delta_m Z) + (T_o R_s)_{n,m}^n(\Delta_m P_o^{n+1}$$

$$- yo_{\,n,m}^{\,n}\Delta_m Z)] = C_{gp_n}\Delta_t P_{o_n} + C_{gw_n}\Delta_t S_{w_n} + C_{gg_n}\Delta_t S_{g_n} - q_{gsc_n}^n \tag{53}$$

for oil, water and gas phases (free and solution gas) respectively, where

$$q_{gsc_n}^n = q_{fgsc_n}^n + R_{s_n}^n q_{osc_n}^n \tag{54}$$

Oil, water and gas equations defined above are combined to obtain the pressure equation for block (n), through the elimination of the saturation terms $\Delta_t S_{w_n}$ and $\Delta_t S_{g_n}$ that appear on the right hand side of the equations. This is achieved by multiplying the oil equation by $(B_o - B_g R_s)_n^{n+1}$, the water equation by $B_{w_n}^{n+1}$ and the gas equation by $B_{g_n}^{n+1}$, then summing all three equations. Coefficient matrices in Cartesian coordinates, $(W, E, N, S, C \text{ and } Q)$ are obtained from transmissibility values as follows

$$W_{i,j} = T_{ww,i,j-\frac{1}{2},}B_{w_n}^{n+1} + (B_o - B_g R_s)_n^{n+1}T_{ow,i,j-\frac{1}{2}} + B_{g_n}^{n+1}[T_{gw,i,j-\frac{1}{2}} + T_{ow,i,j-\frac{1}{2}}R_{so} \tag{55}$$

$$E_{i,j} = T_{we,i,j+\frac{1}{2},}B_{w_n}^{n+1} + (B_o - B_g R_s)_n^{n+1}T_{oe,i,j+\frac{1}{2}} + B_{g_n}^{n+1}[T_{ge,i,j+\frac{1}{2}}$$

$$+ T_{oe,i,j+\frac{1}{2}}R_{so(i,j)}] \tag{56}$$

$$N_{i,j} = T_{wn,i+\frac{1}{2},j}{B_w}_n^{n+1} + (B_o - B_g R_s)_n^{n+1} T_{on,i+\frac{1}{2},j} + {B_g}_n^{n+1}[T_{gn,i+\frac{1}{2},j} +$$

$$T_{on,i+\frac{1}{2},j} R_{so(i,j)}] \tag{57}$$

$$S_{i,j} = T_{ws,i-\frac{1}{2},j}{B_w}_s^{n+1} + (B_o - B_g R_s)_n^{n+1} T_{osi-\frac{1}{2},j} + {B_g}_s^{n+1}[T_{gs,i-\frac{1}{2},j} +$$

$$T_{os,i-\frac{1}{2},j} R_{so(i,j)}] \tag{58}$$

$$C_{i,j} = -[(B_o - B_g R_s)_n^{n+1} C_{op} + {B_w}_n^{n+1} C_{wp} + {B_g}_n^{n+1} C_{gp}) + \sum_{m \in \varphi n}(B_o - B_g R_s)_n^{n+1}$$

$$+ T_w {B_w}_n^{n+1} + {B_g}_n^{n+1}(T_g + T_o R_{so})]P_o^{n+1} \tag{59}$$

$$Q_{i,j} = -\left[(B_o - B_g R_s)_n^{n+1} C_{op} + B_{w+} C_{wp} + {B_g}_n^{n+1} C_{gp}\right) P_o^n - (B_o -$$

$$B_g R_s)_n^{n+1} q_{osc} - {B_w}_n^{n+1} q_{wsc} - {B_g}_n^{n+1} q_{gsc} + \sum_{m \in \varphi n}(T_w B_w \Delta_m P_{cow}) -$$

$$\sum_{m \in \varphi n}(T_g B_g \Delta_m P_{cgo}) \tag{60}$$

$$Q_{gi,j} = {B_g}_n^{n+1}(T_g y_g + T_o y_o R_{so}) + T_w {B_w}_n^{n+1} y_w + (B_o - B_g R_s)_n^{n+1} T_o y_o]\Delta_m Z \tag{61}$$

The coefficient equations C_{lu} where $l = o, w$ or g and $u = P_o, S_w, or$ S_g are defined in the Appendix A. Numerical differentiation procedures were implemented when the calculation of the derivatives of nonlinear terms were required.

Equations 51, 52, and 53 can be rearranged and expressed simply in the form

$$W + E + N + S - C = Q + Q_G \tag{62}$$

Fluid production rates $(q_{lsc} \; where \; l = o, w, g, L)$ that appear in the finite difference equations are related to each other through their relative permeabilities and flowing bottom-hole pressure of the well.

The pressure equation is written for all grid blocks $n = 1,2,3,4 \dots N$ and the resulting set of pressure equations is solved for block pressures in the next time step i.e. $P_o^{n+1} \; for \; n = 1,2,3,4 \dots N$. We iterate on $(B_{o_n}^{n+1}, B_{w_n}^{n+1}, B_{g_n}^{n+1}, \; R_{s_n}^{n+1}, C_{op_n}, C_{wp_n} \, and \, C_{gp_n})$ to preserve the material balance.

For a two dimensional grid system, the set of nonlinear equations to be solved for pressures is

$$e_{i,j}P_{i,j-1} + a_{i,j}P_{i-1,j} + b_{i,j}P_{i,j} + c_{i,j}P_{i+1,j} + f_{i,j}P_{i,j+1} = d_{i,j} \tag{63}$$

Water and gas saturations for grid block (n) in the next time step $(n+1)$ are solved for explicitly by substituting the pressure solution in the gas and water equations.

$$
S_{w_n}^{n+1} = S_{w_n}^{n} + \frac{1}{C_{ww_n}} \{ \textstyle\sum_{m \in \varphi n} [T_{o_{n,m}}^{n} (\Delta_m P_o^{n+1} - \Delta_m P_{cow}^{n} - y_{o_{n,m}}^{n} \Delta_m Z)] -
$$
$$
C_{wp_n}(P_o^{n+1} - P_o^{n}) + q_{wsc_n}^{n} \} \tag{64}
$$

$$
S_{g_n}^{n+1} = S_{g_n}^{n} + \frac{1}{C_{og_n}} \{ \sum_{m \in \varphi n} [T_{o_{n,m}}^{n} \Delta_m P_o^{n+1} - y_{o_{n,m}}^{n} \Delta_m Z)] - C_{op_n}(P_o^{n+1}
$$
$$
- P_o^{n}) - C_{ow_n}(S_{w_n}^{n+1} - S_{w_n}^{n}) + q_{osc_n}^{n} \} \tag{65}
$$

This new estimate for water saturation is used to update the capillary pressure for block (n), P_{cow}^{n+1} and P_{cgo}^{n+1} , these updated values will be used as P_{cow}^{n} and P_{cgo}^{n} in the following time step.

3.1.6.7   IMPES Stability for Three Phase Flow Cases

The IMPES stability criterion used in solving this Three-Phase Black oil simulation problem was derived by Coats [36, 37]. It accounts for viscosity, gravity and capillary forces in both structured and unstructured grids and gives a stable step size for each grid block. These stable steps are used to set the time step size in this IMPES formulation. Explicit treatment of saturations give rise to a conditional stability for IMPES,

$$CFL_i = \frac{F_i \Delta t}{V_{pi}} \leq 1 \tag{66}$$

Δt = Maximum stable time step and F_i = some function of rates that accounts for viscosity, gravity and capillary forces in concurrent and countercurrent three-phase flow, reservoir and fluid properties. The maximum stable time step is limited by the above condition with

$$F_i = \frac{1}{21} f11_i + f22_i + \sqrt{(f11_i + f22_i)^2 - 4\det(F_i)}| \tag{67}$$

where each (f) is a sum of J_i terms, one for each of the J_i neighbors of block $i, j = 1,2, \ldots \ldots J_i$ and is a function of transmissibility, phase mobility, capillary pressure and potential gradient.

Non-oscillatory stability are expected for choice of time steps that satisfy a CFL $= 1$, and values of $CFL_i > 1$ are less stable [37].

The use of finite difference equations in three phase flow modeling, results in truncation errors in time and space dimensions. These errors can be minimized if the time and distance increments are reduced. For simulating the A-1 reservoir, a time step of 0.5 day was used which satisfies the CFL condition and the results obtained are in good agreement with those simulated in the book.

3.1.6.8   Boundary Conditions

Boundary conditions specify how the reservoir interacts with its surrounding area. Simulation studies and flow equations developed for the A-1 reservoir took into account two kinds of boundary conditions.

3.1.6.8.1 External Boundary Conditions;

The A-1 reservoir boundary is subjected to two conditions, the Neumann boundary (No flow boundary) and the Dirichlet boundary (Constant pressure boundary) flagged as 2 and 3 respectively in the model. Results for the second condition were not analyzed in this problem.

Modifications made to Q and C were reported for one side of the block and were representative of changes made in all four directions.

3.1.6.8.1.1 No Flow Boundary:

This condition results from varnishing permeability at a reservoir boundary or because of symmetry about a reservoir boundary. We assume no fluid flow between boundary block (bB) and reservoir boundary (b).

$$q_{psc_{b,bB}}^{n+1} = 0 \tag{68}$$

If the reservoir left (west) boundary is bounded with a no flow boundary, the W term in matrix, would be updated by modifying C term and Q term. The Q term is updated with formation volume factors (FVF), transmissibility values and capillary pressures of phases present across the boundary, where both $gpby$ and $gpbx$ are assumed zero. Primarily,

$$C_{i,j} = C_{i,j} + W_{i,j}$$

$$\tag{69}$$

$$Q_{i,j} = Q_{i,j} + W_{i,j} * gpbx_{i-1,j} * dx_{i,j} - B_w T_{ww} \Delta_m P_{cow} + B_g T_{gw} \Delta_m P_{cgo} - E_g * \Delta_m Z \tag{70}$$

$$W_{i,j} = 0$$

$$\tag{71}$$

3.1.6.8.1.2 Constant Pressure Boundary:

Phase flow rates through this type of boundary condition is calculated using the following equation:

$$q_{psc_{b,bB}}^{n+1} = [\frac{k_l k_{rp} A_l}{\mu_p B_p \frac{\Delta l}{2}}]_{bB}^{n+1}(P_b - P_{bB}^{n+1}) - y_{bB}^{n+1}(Z_b - Z_{bB})]$$

$$(72)$$

If the reservoir's left (west) boundary is of constant pressure boundary (p_{const}), the W term in matrix, would be updated by modifying C and Q terms. The W term would be moved from the LHS to the RHS of the equation, the Q term would be modified to

$$Q_{i,j} = Q_{i,j} - W_{i,j}(2p_{const} - p_{i,j}) - B_w T_{ww} \Delta_m P_{cow} + B_g T_{gw} \Delta_m P_{cgo} - E_g * \Delta_m Z$$

$$(73)$$

$$W_{i,j} = 0$$

$$(74)$$

3.1.6.8.2   Internal Boundary Conditions;

For a well located in the central part of the field, the flow domain is the area between the limits of the reservoir and the wellbore. Well models are used to relate the pressure of the well block to the bottom hole flowing pressure at the well. This pressures are unequal because grid block dimensions are substantially larger than the wellbore radius (r_{wf}). All five wells ($W - 1\ to\ W - 5$) are treated as active wells and assumed to have no skin. Relevant well information, boundary conditions specified at each well location and phase relative mobility equations used in the successful simulation of this project are reported in **Table 4 and 5**.

Table 4. Well data used in black oil simulator

Name	Grid block	Type	Radius (r_{wf})	Specification
$W-1$	(7,7)	Producer	0.25	$q_{tsc} = -100000$ STB /D
$W-2$	(9,3)	Producer	0.25	$P_{sf} = 3400$ psia
$W-3$	(4,4)	Producer	0.25	$q_{osc} = -100$ STB/D
$W-4$	(3,2)	Producer	0.25	$q_{gsc} = -1000000$ SCF /D
$W-5$	(6,4)	Producer	0.25	$q_{Lsc} = -150$ STB/D

Table 5. Well rate specifications and definitions of phase relative mobility

Well Specification option	Well specification rate	Oil Phase F_o	Water Phase F_w	Gas Phase F_g
Op_1	P_{sf}	/	$P_{wf_{sp}}$	/
Op_2	q_{tsc}	$\dfrac{(1 + R_s\alpha_c)k_{ro}}{\mu_o B_o}$	$\dfrac{k_{rw}}{\mu_w B_w}$	$\dfrac{k_{rg}}{\mu_g B_g}$
Op_3	q_{osc}	$\dfrac{k_{ro}}{\mu_o B_o}$	/	/
Op_4	q_{gsc}	$\dfrac{R_s * k_{ro}}{\mu_o B_o}$	/	$\dfrac{k_{rg}}{\alpha_c\mu_g B_g}$
Op_5	q_{Lsc}	$\dfrac{k_{ro}}{\mu_o B_o}$	$\dfrac{k_{rw}}{\mu_w B_w}$	/

F_o, F_w and F_g, are the phase relative mobility's for the oil, water and gas phases respectively. q_{lsc}, represents the oil, gas, liquid and total rate well specifications *where* $l = o, t, g, L$ at standard conditions and P_{sf} is the specified sand face pressure.

3.1.6.8.2.1   Treatment of Rate Specified Wells ($Op_2 - Op_5$):

Well rate specifications of any phase implicitly dictates the production rates of the other phases. When the production rate of any phase is specified, calculating production rates of the phases that are not specified, as well as partitioning production rates back to individual phases when a liquid production rate or a total production is specified can be done with the following algorithm.

First we calculate the flowing sand face pressure in the well, from rate of phase specified q_{sp}

$$P_{wf} = P_{on} + \frac{q_{sp}}{G_{wn} * \Sigma\, F_{ln}} \tag{75}$$

where

- $l = o, w, g, L, t.$
- q_{sp} is the rate of phase specified ($Op_2 - Op_5$).
- G_{wn} = wellblock geometric factor for grid block (n)
- P_{on} is the average pressure in the circular area defined by r_e, the external radius.

Then we calculate the rates not specified or partition liquid/total production rates using

$$q_{lscn} = \left(\frac{k_{rl}}{\mu_l\, B_l}\right) \cdot \frac{q_{sp}}{G_{wn} * \Sigma\, F_{ln}} \tag{76}$$

for oil and water and

$$q_{fgscn} = \left(\frac{k_{rg}}{\mu_g\, B_g} + \frac{R_{so} k_{ro}}{\mu_o\, B_o}\right) \cdot \frac{q_{sp}}{G_{wn} * \Sigma\, F_{ln}} \tag{77}$$

$$q_{gscn} = q_{fgscn} + R_s q_{osc} \tag{78}$$

for free gas and gas in solution respectively.

After obtaining the individual flow rates, we update our Q matrix in the well bore with flow rates as in the following equation

$$Q = Q - \left(q_{wsc} B_w + q_{osc}(B_o - R_S B_g) + B_g q_{gsc} \right) P_{wf} \tag{79}$$

We use a negative sign convention for producing wells, a positive sign convention for injection wells and set the flow rates equal to zero for shut-in wells.

3.1.6.8.2.2 Treatment of Pressure Specified Wells (Op_1):

If the bottom hole pressure of a well P_{wf} is specified, the production rate of phase q_{lscn} where $l = o, w \ and \ fg$, from wellblock (n) can be computed from the following

$$q_{lscn} = -G_{wn} * \frac{k_{rl}}{\mu_l B_l} * [P_{on} * P_{wf}] \tag{80}$$

for oil and water and

$$q_{fgscn} = -G_{wn} * \left(\frac{k_{rg}}{\mu_g B_g} + \frac{R_{so} k_{ro}}{\mu_o B_o} \right) * [P_{on} * P_{owf}] \tag{81}$$

$$q_{gscn} = q_{fgscn} + R_s q_{osc} \tag{82}$$

for free gas and gas in solution respectively.

After obtaining the individual flow rates, we update our Q and C matrix in the well bore with the productivity index J_w and bottom-hole pressures as specified in the following equation

$$C = C - J_{ww} B_w + J_{wo}(B_o - R_S B_g) + J_{wg} B_g q_{gsc} \tag{83}$$

$$Q = Q - \left(J_{ww} B_w + J_{wo}(B_o - R_S B_g) + J_{wg} B_g \right) P_{wf} \tag{84}$$

where $J_w = G_{wn} F_l$, F_l being the phase relative mobilities and

$$G_{wn} = \frac{2\pi\beta_c k_h h}{\ln_{(\frac{r_{eq}}{r_w})} + s}$$

(85)

k_h, and r_w are the geometric mean permeability value in the radial direction and wellbore radius respectively. r_{eq}, is the equivalent radius at which steady state pressure in the reservoir equals the well block pressure as determined from the Peaceman's Model for non-square well blocks with anisotropic permeability.

$$k_h = (k_x k_y)^{1/2}$$

(86)

$$r_{eq} = \frac{\{[(\frac{k_y}{k_x})^{\frac{1}{2}}(\Delta x)^2] + [(\frac{k_x}{k_y})^{\frac{1}{2}}(\Delta y)^2]\}^{1/2}}{[(\frac{k_y}{k_x})^{\frac{1}{4}} + [(\frac{k_x}{k_y})^{\frac{1}{4}}]}$$

(87)

3.1.6.9   Material Balance

A material balance check is performed to check the conservation of mass over a fixed volume (hydrocarbon reservoir). The validity of this simulator is dependent on how the calculated pressures satisfy the material balance. We compare the values of the total volume of fluid entering the reservoir to the total volume of fluid leaving the boundaries of the reservoir. This check is trivial for flow of incompressible fluids because no fluid depletion or accumulation occurs within the reservoir. For slightly compressible fluid flow of oil or water, material balance equations are expressed as follows;

$$IMBo = \frac{\sum_{i=1}^{i=I} \sum_{j=1}^{j=J} \frac{Vb\emptyset So}{\alpha_c} \left(\frac{1}{B_o^{n+1}} - \frac{1}{B_o^n}\right)}{dt(n) * \sum_{i=1}^{i=I} \sum_{j=1}^{j=J} q_{osc}^{n+1}} \tag{88}$$

$$IMBw = \frac{\sum_{i=1}^{i=I} \sum_{j=1}^{j=J} \frac{Vb\emptyset Sw}{\alpha_c} \left(\frac{1}{B_w^{n+1}} - \frac{1}{B_w^n}\right)}{dt(n) * \sum_{i=1}^{i=I} \sum_{j=1}^{j=J} q_{wsc}^{n+1}} \tag{89}$$

and,

$$IMBg = \frac{\sum_{i=1}^{i=I} \sum_{j=1}^{j=J} \frac{Vb\emptyset Sg}{\alpha_c} \left(\frac{1}{B_g^{n+1}} - \frac{1}{B_g^n}\right) + \sum_{j=1}^{j=J} \frac{Vb\emptyset So}{\alpha_c} \left(\frac{R_S}{B_o^{n+1}} - \frac{R_S}{B_o^n}\right)}{dt(n) * \sum_{i=1}^{i=I} (\sum_{j=1}^{j=J} q_{fsc}^{n+1} + \sum_{j=1}^{j=J} R_S^{n+1} q_{osc}^{n+1})} \tag{90}$$

for compressible fluid flows (gas flows).

3.1.6.10   GMRES Solver

The matrices generated by the finite difference method (FDM) are usually symmetric and very sparse. Thus the solutions for these problems are very efficient and well developed. In the event where we need to solve a non-symmetric system of equations, a more efficient technique is required to solve matrices for minimal errors and computing time. Generalized minimal residual solvers (GMRES) have been developed and are very efficient in solving non symmetric matrices. GMRES is an iterative method for the numerical solution of a non-symmetric system of linear equations. It approximates the solution by the vector in a krylov subspace by minimizing the residual vector. The Arnoldi iteration is used to find this vector [38]. We denote the system of equations to be solved by **Equation 91.**

$$Ax = b \qquad\qquad (91)$$

The IMPES solution method described above is used to obtain the linearized set of flow equations for all blocks which can then be solved using the GMRES solver to obtain the solution for one-time step. Matrix A denotes the coefficients (N, S, W, E and C) calculated at a current time step (n) and Matrix b represents Q matrix. This solver solves for matrix x to obtain the pressures at the next time step ($n + 1$). For more complicated methods such as the higher-order boundary element method (HOBEM), preconditioners such as Jacobian, SSOR, Incomplete Cholesky Factorization and Neumann polynomial are usually applied to GMRES to make it more efficient.

3.2   Phase II–Simulation of the Cleanup Process in Hydraulically Fractured Wells

Tight gas sands now constitute roughly 75% of unconventional production, posing a huge potential for future investments. However, cost-effective production from these reservoirs has been very challenging due to extremely low porosity and permeability (micro-Darcy range) that restrains gas production rates. As such, advanced stimulation techniques such as hydraulic fracturing have been applied to increase wellbore contact and optimize return from low-permeability gas reservoirs. During the fracturing process, millions of gallons of water, sand and chemicals are injected into the reservoir under high pressure to crack the rock open and increase contact between the wellbore and the producing formation. The choice of fracturing fluid is critical to the success of the fracture treatment. It must be viscous enough to initiate and propagate the fracture, transport the proppants (sand particles) down the fracture and be easily broken down after the injection phase. These sand particles help to keep the fissures open to allow natural gas flow up into the well.

The ideal propping agent should be strong, resistant to crushing, resistant to corrosion, cheap and have a low density. Increasing the viscosity of the fracturing fluid decreases the proppant settling velocity and the volume of fluid lost to the reservoir matrix. Proppant settling velocity in a vertical fracture is calculated using Stokes law [39] as follows

$$\frac{(\rho_p - \rho_f)gd^2}{18\mu} \tag{92}$$

ρ_p , is the density of proppants (kg/m^3), ρ_s density of fluids (kg/m^3), d proppant diameter (m), μ viscosity of the fluid (kg$m^{-1}s^{-1}$) and g the acceleration due to gravity (m/s^2).

When fluid is lost to the matrix, filter cakes of high polymer concentration conceal the faces of the propped fracture. Productivity increases with increasing amounts of proppants placed in the fracture for both unconventional and conventionally hydraulic fractured wells [40, 41]. Guar-based fluids are typically used as fracturing fluids during injection. These are shear thinning fluids, whose viscosities decrease with increasing shearing. Cross-linkers and breakers are usually added to the fluid to degrade the polymer gel and filter cake. The filter cake formed is supposedly broken in a non-uniform fashion [42, 23]. However, unless the correct breakers are used, the viscous fluids

fail to break, thereby damaging the fracture, impairing conductivity and significantly curtailing production.

3.2.1 Fractured Well Model

To study the effect of increasing breaker concentration on broken gel viscosity and yield stress of filter cake, capillary pressure, fracture conductivity, aqueous phase trapping, fracture length and formation damage on long-term fluid recovery, the three-phase IMPES black oil simulator developed in chapter three was used to model fracturing fluid clean up and simulate the performance of fractured wells in tight gas reservoirs with homogeneous and isotropic properties. Bennet-type grid distribution [22] is applied to have finer grids near the fracture, wellbore and fracture tip. The length of the fracture L_{x_f}, the length of grid to external boundaries L_{i_e} and the fracture width b are very crucial in determining the grid block sizes. Finer grids should be applied to the model near the well for more accurate pressure and saturation calculations and equally near the fracture tip to model large pressure gradients accurately [22]. Away from the fracture larger values of Δx and Δy are used which are largely dependent on L_{i_e}. The algorithm for choosing suitable grids for fractured wells as determined by Bennett is included in Chapter 8.2, **Figure 89.**

We assumed a symmetric fracture that extends equal distances on both sides of the wellbore and spans the complete thickness of the formation, as such only $1/4$ of the drainage area from the fracture was simulated. **Figure 20** shows the schematic of the fractured well model used in this study.
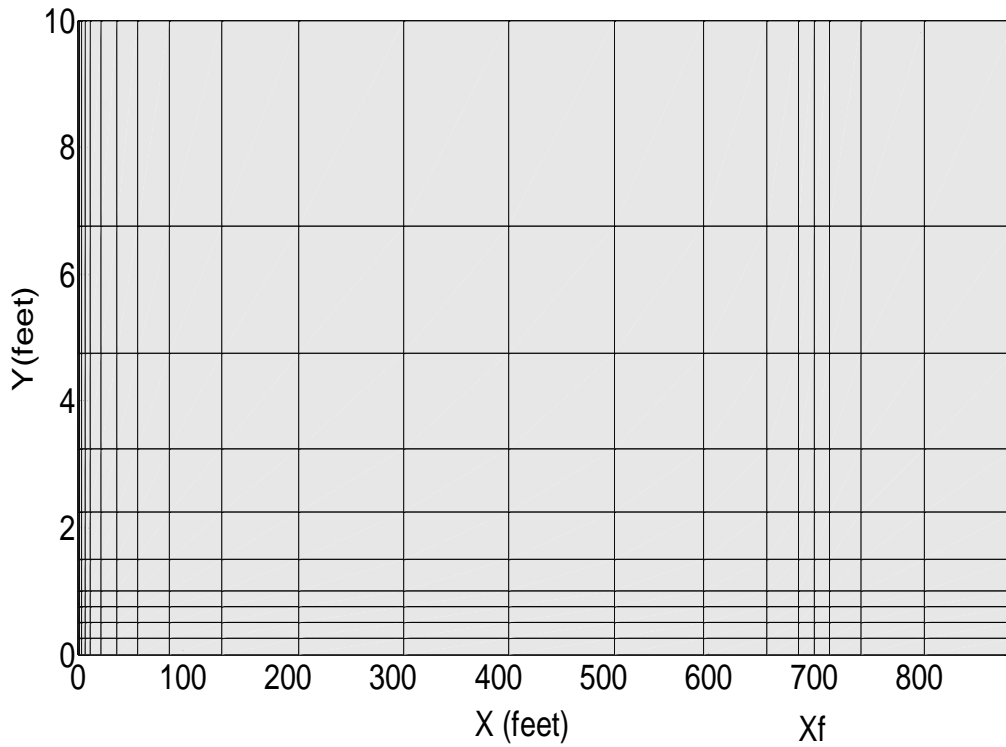
Figure 20. Schematic diagram of fractured well model used in simulation study [22].

3.2.2 Model Properties

The three phases simulated in this project include gas, water and fracturing fluid. Reservoir fluid properties were gotten from the data set in Yilin Wang's dissertation [7]. Stone's second method was applied to compute the relative permeability of the gel phase. Capillary curves used in the reservoir formation were obtained from Holditch [43] as seen in **Figure 21**. Linear relative permeability curves and zero capillary pressures were applied in the fracture, **Figures 23 and 24**. The gel phase was restricted to the fracture and only the gas and water phase was simulated in the formation. The two phase relative permeability curve used in the formation is shown in **Figure 22**.

$$k_{rw} = S_w \tag{93}$$
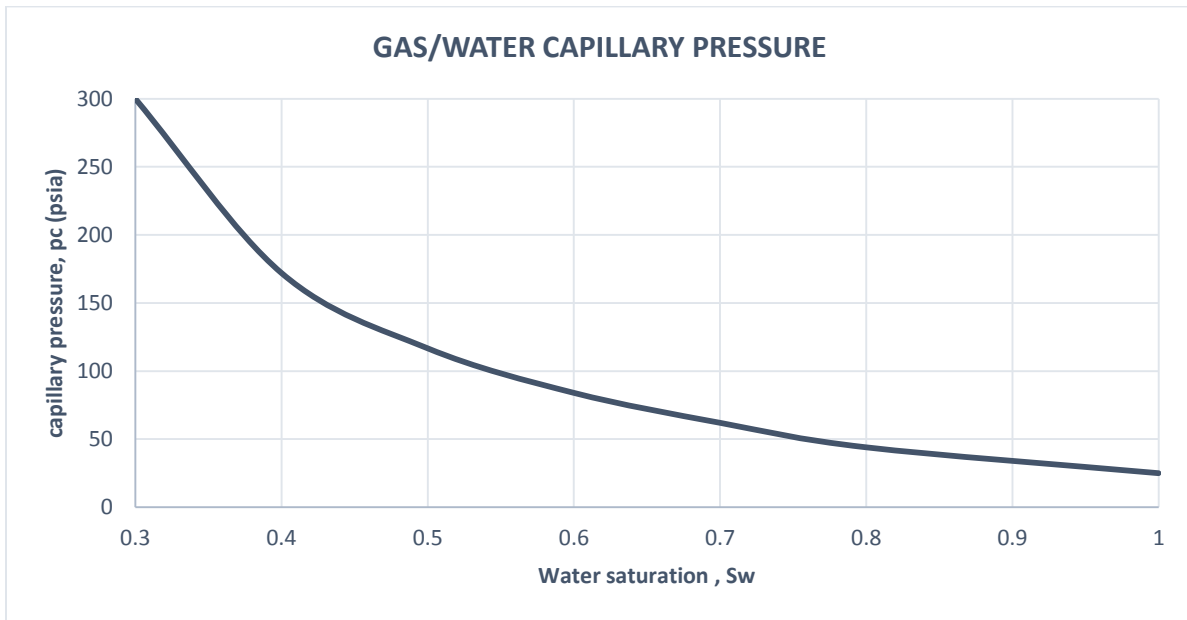
$$k_{rg} = 1 - S_w \tag{94}$$

Figure 21. Gas-water capillary pressure curve used in fractured well simulation [44]
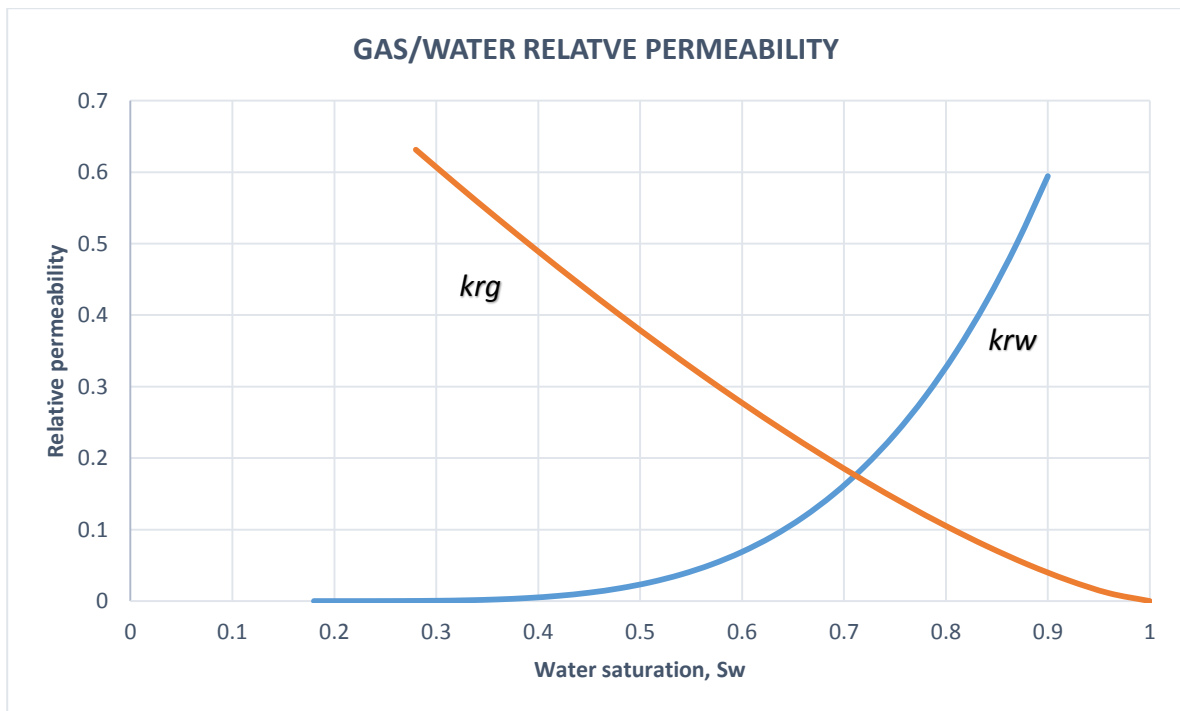

Figure 22. Gas-water relative permeability curve used in fractured well simulation
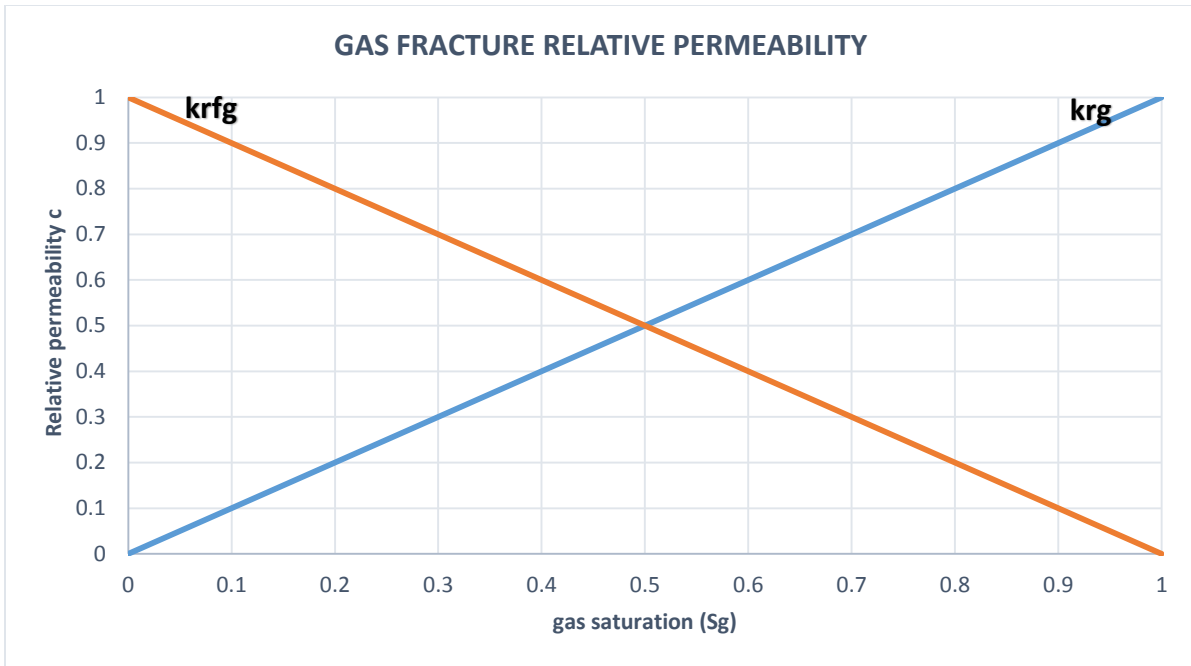
Figure 23. Gas-fracture relative permeability curve used in fracture simulation
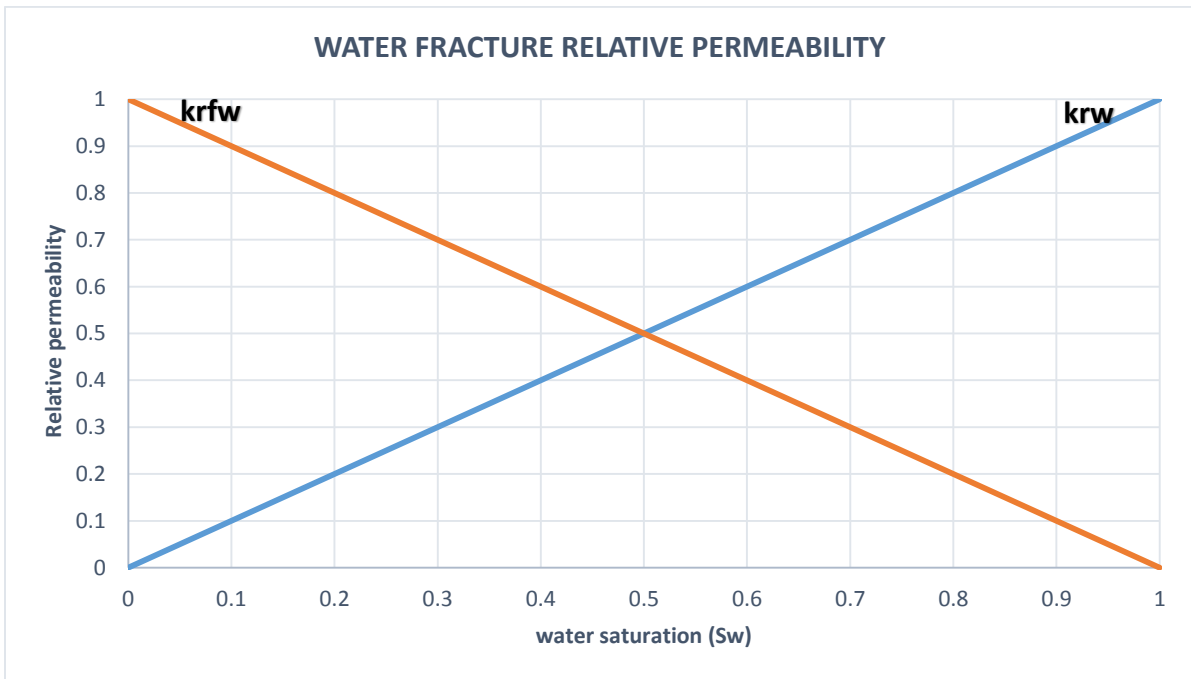

Figure 24. Water-fracture relative permeability curve used in fracture simulation

Table 6. Properties for Fractured Model

Parameter	Value
Initial model dimensions (feet)	2000 x 2000
Reservoir thickness (feet)	40
Formation permeability (md)	0.05
Formation porosity (%)	10
Fracture porosity (%)	50
Formation depth (feet)	8000
Reservoir pressure (psi)	5830
Reservoir temperature (F)	190
Fracture half length (feet)	210, 410, 700, 1000
Fracture half width (feet)	0.25
Dimensionless fracture conductivity	0.1, 1, 5, 10
Bottom hole pressure	580
Gas specific gravity	0.6
Water compressibility (psi^{-1})	3.00E-06
Rock compressibility (psi^{-1})	3.00E-06
Initial water saturation	0.5
Initial gas saturation	0.5
Leak off volume (bbls)	200
Irreducible gel saturation	0
Fluid flow behavior index	0.5, 0.8, 1, 10
Fluid yield stress (Pa)	0-19.49
Fluid consistency index (dyne-$s^{n'}/cm^2$)	40-2000
Wellbore radius rw_f (feet)	0.01
Damage ratio ($\frac{k_d}{k}$)	1, 0.1 , 0.01, 0.001

3.2.3 Methodology

A two-phase gas/water model was used to establish the initial conditions for the fracturing cleanup model. Gas was assumed as the non-wetting phase and capillary pressure in the formation was calculated from the following

$$P_{cgw} = f(S_w) = P_g - P_w \tag{95}$$

Damage to the formation is accounted for by increasing the water saturation in the invaded zone (aqueous phase trapping) and reducing the permeability in the formation six inches away from the fracture face (mechanical damage).

3.2.3.1 Leak off Model

Water was injected for 0.05 and 0.1 of a day under high pressure of 5830 psi, and the well was shut-in for roughly equal amounts of time to initiate fracture closure and proppant embedment. 200 barrels of water was injected to create the leak off profile and model formation damage. Hydraulic damage created was analyzed for its influence on post-fracture well performance. The leak off fluid was distributed by increasing the fracture conductivity along the specified fracture length and time. By specifying the total injection time and the total length of the fracture, the fracture length at each time was calculated by use of the following equation [12, 23] ,

$$\frac{x_f(t)}{t^{0.5}} = \frac{x_f}{t_{end}^{0.5}} \tag{96}$$

Pressure dissipation and saturation distribution through the reservoir during injection and shut-in time are shown in **Figures 25, 26, 27 and 28**. Images are magnified for a clearer representation of changes near the fracture and wellbore.

During shut-in period, overpressure in the fracture causes water to continually imbibe into the formation creating a damage zone around the fracture and lowering the water saturation in the fracture. The extent of this damage zone is dependent on exposure time of fluid to the formation and the rock/fluid properties of the formation. Continuous water influx from fracture into reservoir lowers the pressure in the fracture as a result of the low water compressibility in the formation. However, this process is equally restricted by the low matrix permeability of the reservoir. Simulating the fracturing fluid by a fictitious water injection process has a limitation in that in a real case scenario, its properties are altered by enzymes/breakers, temperature/pressure changes as well as mixing processes. Moreover, there is mechanical damage from fluid invasion into the reservoir matrix, filter cake formation, clay swelling from mineral interaction as well as broken polymers/ fine migration into the matrix [43]. The bottom-hole pressure drops quickly, restoring pressure conditions to a near initial condition in the formation.
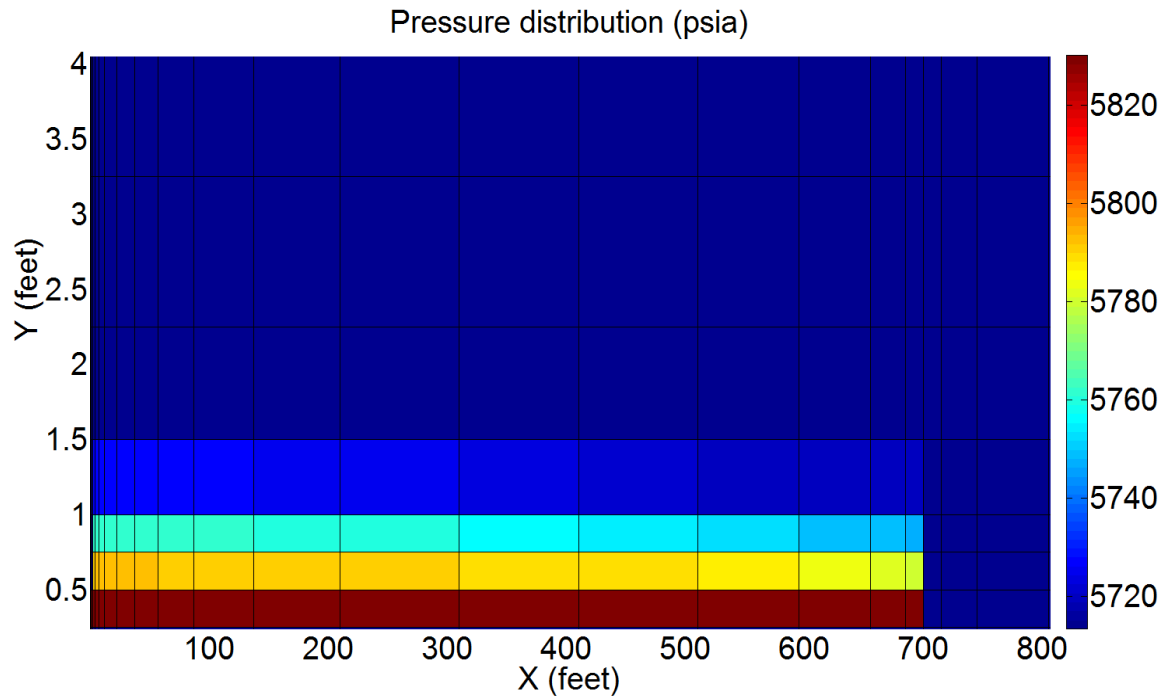
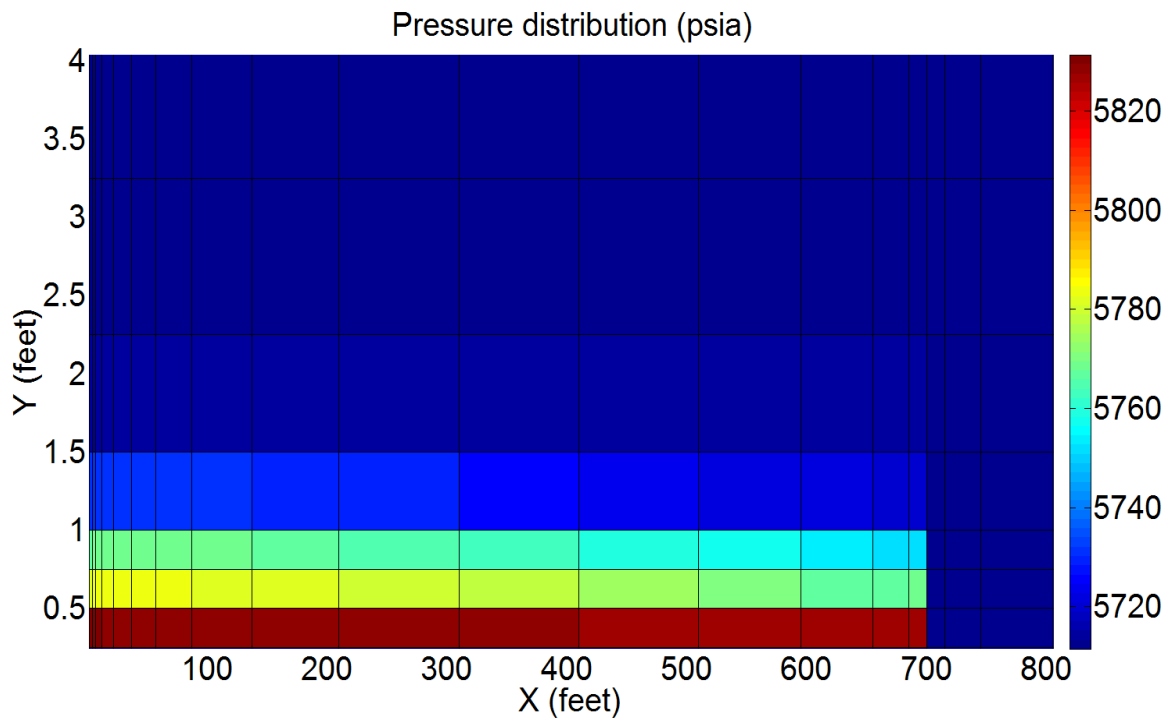*Figure 25. Pressure distribution at the end of 1.2 hours of fluid injection k =0.05md, C_{fd} =1, (magnified).*

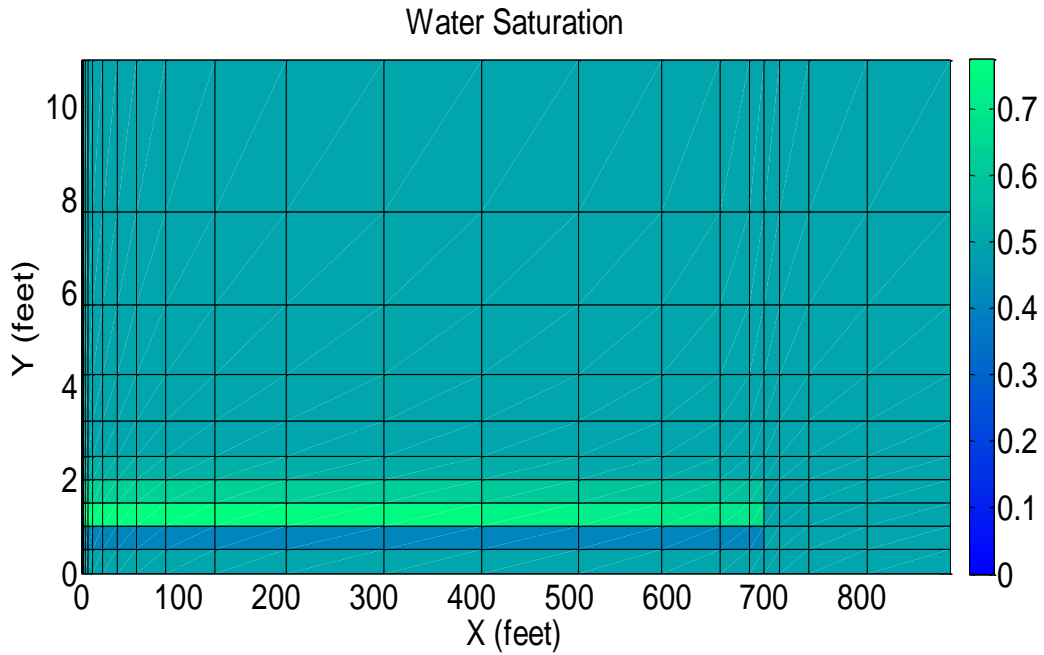*Figure 26.   Pressure distribution at the end of 1.2 hours of shut-in for k=0.05md, C_{fd}= 1, (magnified).*

Figure 27. Water saturation at the end of 1.2 hours of fluid injection for k=0.05md C_{fd}= 1, (magnified).

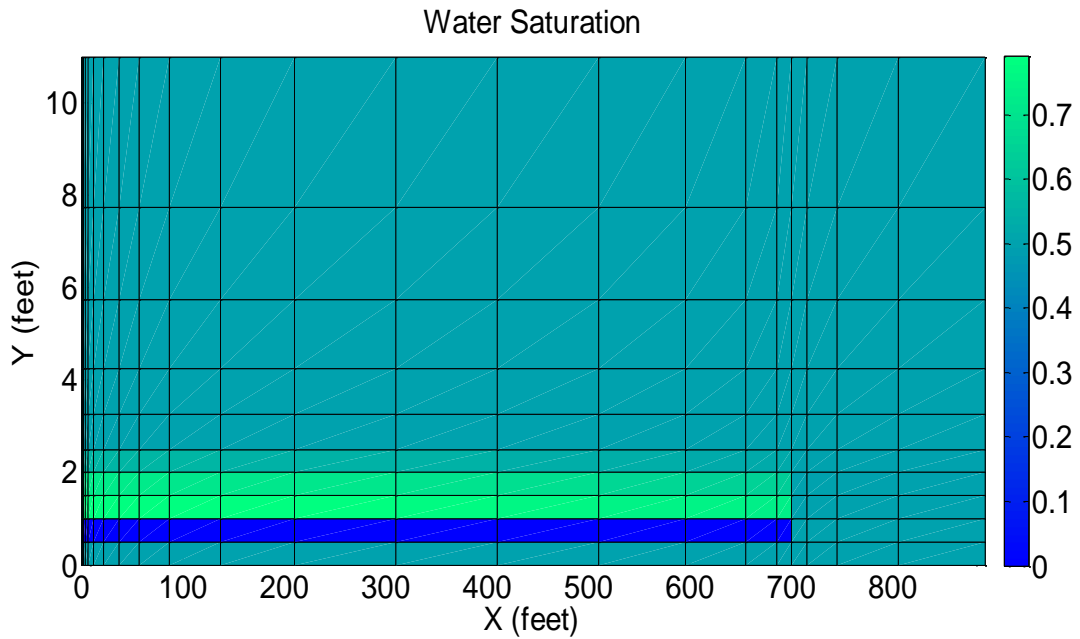*Figure 28. Water saturation at the end 1.2 hours of shut-in for k=0.05md, C_{fd}= 1, (magnified).*

The dimensionless rate q_D for constant flowing bottom hole pressure condition, dimensionless time t_{Dxf} and dimensionless fracture conductivity C_{fD} are expressed as follows;

$$q_D = \frac{141.2b\mu q(t)}{kh(P_i - P_{wf})} \qquad (97)$$

$$t_{Dxf} = \frac{2.637 \; x \; 10^{-4}kt}{\phi c_t \mu L_{xf}^2} \qquad (98)$$

$$C_{fD} = \frac{k_f b}{kL_{xf}} \qquad (99)$$

Where k_f , is the fracture permeability (md), k is the formation permeability(md), and b is the fracture width $(feet)$.

3.2.3.2   Polymer Model

Our reservoir is assumed saturated with connate water saturation before stimulation. Gas, water and gel coexist to fill the pore volume of the reservoir and are related through the following constraint equation.

$$S_o + S_w + S_{gel} = 1 \qquad (100)$$

Fracturing fluid cleanup is simulated using a three phase model for Herschel-Buckley fluids. Production in the cleanup model is simulated after the shut-in period, using pressure and saturation distributions from shut-in as initial conditions. Bottom-hole pressure is assumed 10% of initial reservoir pressure. The water inside the fracture was replaced by the fracturing fluid by setting the gel saturation equal to 1 ($S_{gel} = 1$). Gas and water saturations are set equal to zero within the fracture. In the formation only two phases are assumed to exist (gas and water phase), as such we model zero transmissibility of the gel phase between fracture and formation, zero gel saturation in the formation and a 50-50 pore space occupancy of gas and water in the formation.

The objective of our fracture treatment is increase gas production, this can only be achieved if the fracturing fluid used is viscous enough carry proppants along the created fracture length. In the event of a low viscous fluid the proppants get deposited way before the intended fracture length is achieved, adversely affecting the fracture conductivity. Work done by Cooke [45] , reiterates the

effect of fracturing fluid on fracture conductivity. Polymer deposition on the faces of the fracture forms a filter cake over time which helps to retain the polymer in the fracture, **Figure 29**. The width of the filter cake formed is a function of the leak off rate, fluid efficiency and gel loading [46] . Once our fracture treatment is completed, we expect the fluid to break down rapidly to a low viscosity fluid to prevent pore plugging and facilitate the clean-up process. The rheological properties of the fluid in the fracture at the end of fracture treatment are very different from that initially pumped into the fracture [11].

The filter cake formed if not broken down will develop a yield stress that increases with polymer concentration after leak off. Ben et al. [47] measured the yield stress with increasing Guar concentrations from $40\ to\ 200lb/Mgal$ without breakers. The yield stress was found to be very low at low polymer concentrations but increases sharply as the guar concentration was increased as can be seen in **Figure 30**. The polymer concentration is increased as fluid leak-off occurs and can become very high at the end of a treatment [47]. Local polymer concentration changes along the fracture with exposure times to fracturing fluid [48]. Thus it was concluded that the high yield stress of a fluid can influence the fracturing fluid cleanup process and result in serious gel damage.

Figure 29. Filter cake build up after flowing 35 ppt CMHPG Zr XL fluid with breaker (StimLab Consortium Notes [49])
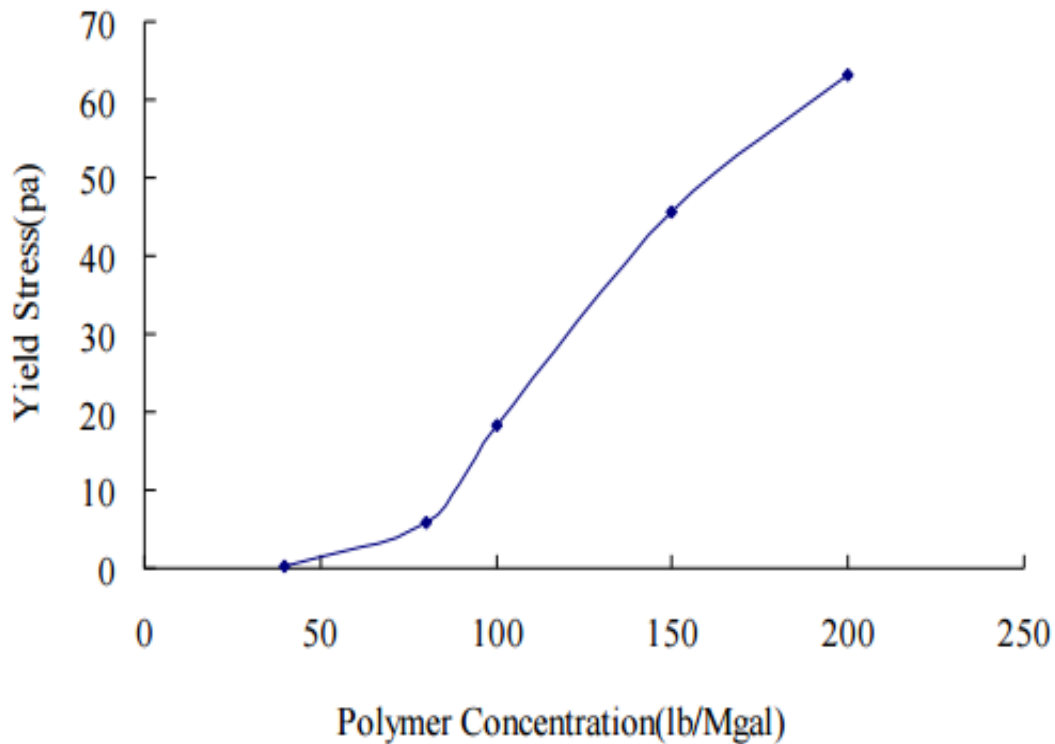
Figure 30. Yield stress with different polymer concentration [47]

They equally ran a couple of other test for which breakers where added to the fracturing fluid. Polymer concentration was varied between $80\ to\ 200\ lb/Mgal$ and the yield stress of fracturing fluid was measured for different concentration of polymer and breaker, **Figure 31**. It was observed that the yield stress becomes smaller with increasing breaker concentration for every concentration of guar and that the yield stress is higher with higher guar concentration for the same concentration of the breaker [47]. An almost linear relationship is established between the guar concentration and the needed breaker concentration to curb the yield stress to zero from the analysis of their experimental results.
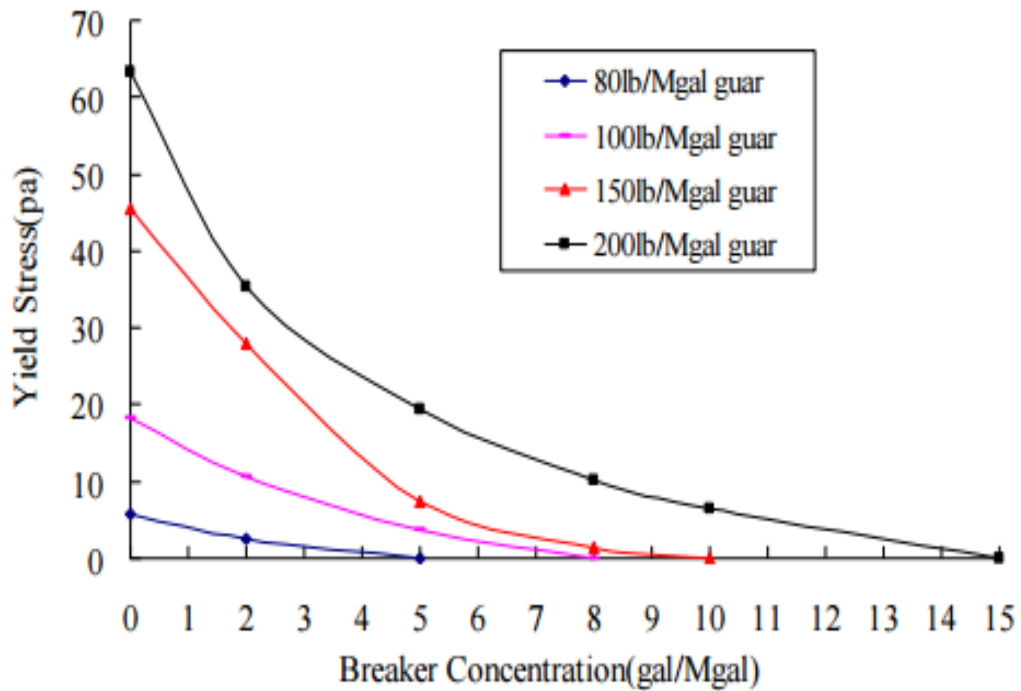
Figure 31. Effect of varying breaker concentration on yield stress [47]

The yield stress range for typical fracturing fluids used on field scale is $(0.04 - 17\ pa)$, Ayoub et al. [42]. Rheological models for the different types of fluids are shown in **Figure 32**. A modified power law model, Herschel-Buckley model is used to describe the fluid flow behavior of our fracturing fluid for finite values of yield stress. Alfariss et al. [21] proved that gels tend to behave like Herschel-Buckley fluids when sheared thus requiring a minimum stress to flow.
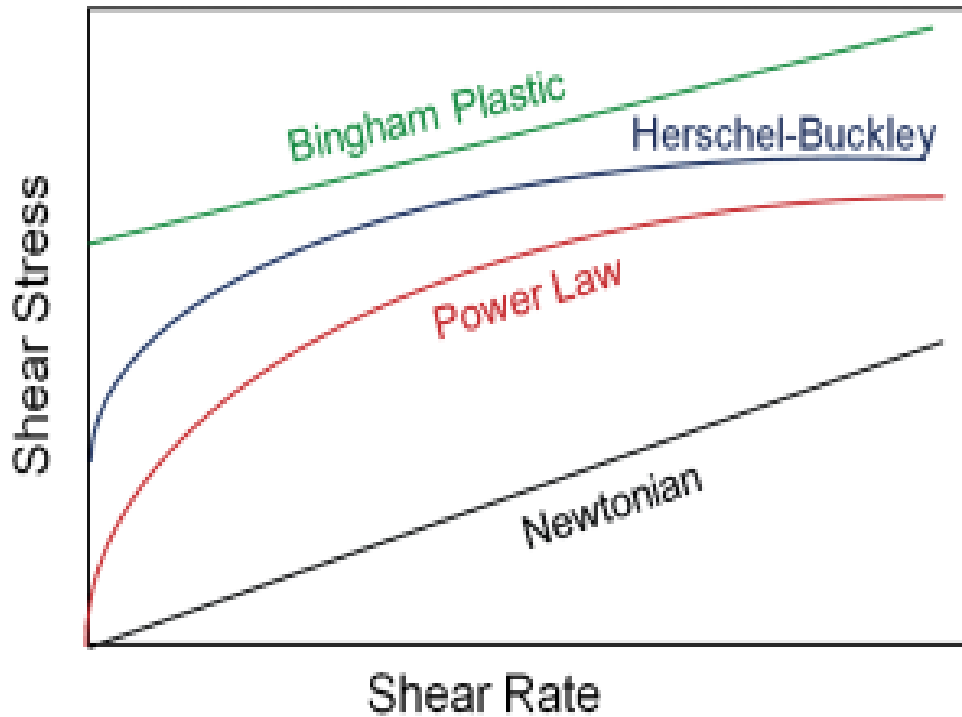
Figure 32. Rheological models [50]

Equations of yield stress and power-law behavior of the gel were used following the work of Yi [51]. Three parameters characterize the non-linear relationship between the strain and the stress experienced by a Herschel–Buckley fluid; the fluid consistency index K', the flow behavior index n', and the fluid yield stress (τ_0) .The yield stress is a measure of the force that must be applied to a material for it to flow. $\frac{dv}{dr}$, the shear rate is a measure of the rate of change of velocity at which one layer of fluid crosses over an adjacent layer.

$$\tau = \tau_0 + K'(\frac{dv}{dr})^{n'} \qquad (101)$$

$$\mu_{eff,nn} = \frac{K'}{12}(9 + \frac{3}{n'})^{n'}(72C\Phi(S_{nn} - S_{ir,nn})kk_{r,nn})^{\frac{1-n'}{2}} \qquad (102)$$

$$\beta = N_n\sqrt{\frac{\Phi C(S_{nn} - S_{ir,nn})}{2kk_{r,nn}}} \qquad (103)$$

$$\mu_{nn} = \begin{cases} +\infty & \left(-\frac{\partial\Phi}{\partial L}\right) < \beta\tau_0 \\[4mm] \dfrac{kk_r\left(-\frac{\partial\Phi}{\partial L}\right)}{[\frac{kk_r}{\mu_{eff,nn}}((-\frac{\partial\Phi}{\partial L}) - \beta\tau_0)]^{\frac{1}{n'}}} & \left(-\frac{\partial\Phi}{\partial L}\right) > \beta\tau_0 \end{cases} \qquad (104)$$

$$N_n = \frac{3n' + 1}{3n' + 1} - \frac{3(3n' + 1)(1 - n')}{16(2n' + 1)^2(n' + 1)} \qquad (105)$$

The viscosity value μ_{nn} assigned to a fracture grid is grossly dependent on the potential gradient and the yield point of the gel in that grid. A certain threshold pressure gradient is required to initiate flow. If the potential gradient $\frac{\partial\Phi}{\partial L}$ is greater than the yield stress of the gel, the fracturing fluid will flow to the wellbore. If the potential gradient $\frac{\partial\Phi}{\partial L}$ is less than the yield point of the gel, the fracturing fluid behaves as a solid, it remains inside the fracture reducing its conductivity. A large viscosity value of $1000000\ cp$ is assigned to the fracturing fluid for our simulation study when the potential gradient is less than the yield stress. For $n' < 1$, the fluid is shear thinning, for $n' > 1$ the fluid is shear thickening and for $n' = 1$, a Newtonian fluid is obtained.

4   Simulation Results and Analysis

4.1   Phase I Results

The reservoir under consideration is 7,473 feet long, 3,738 feet wide and has a cross-sectional area of 29,000 ft^2. For a total simulation time of 60 days, the following results were obtained;
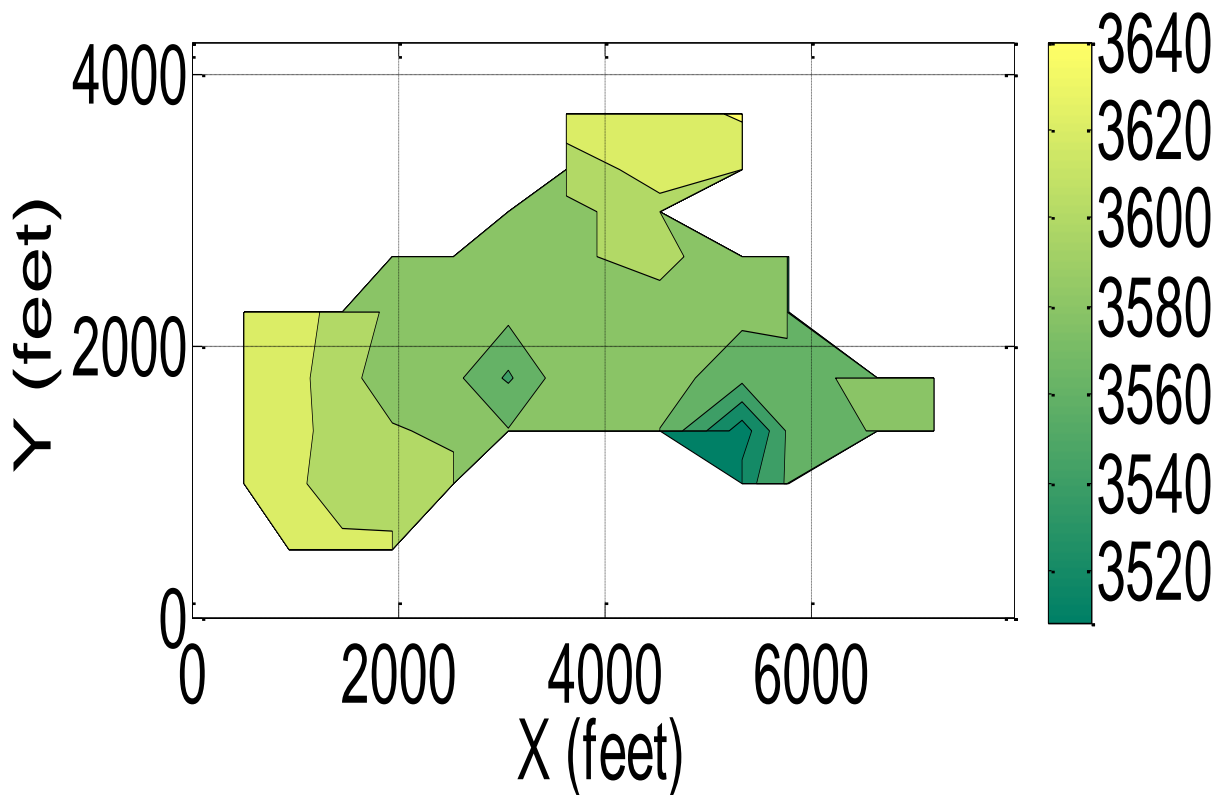
4.1.1 Pressure Maps

Figure 33. Oil pressure dissipation in A-1 reservoir after 60 days of production
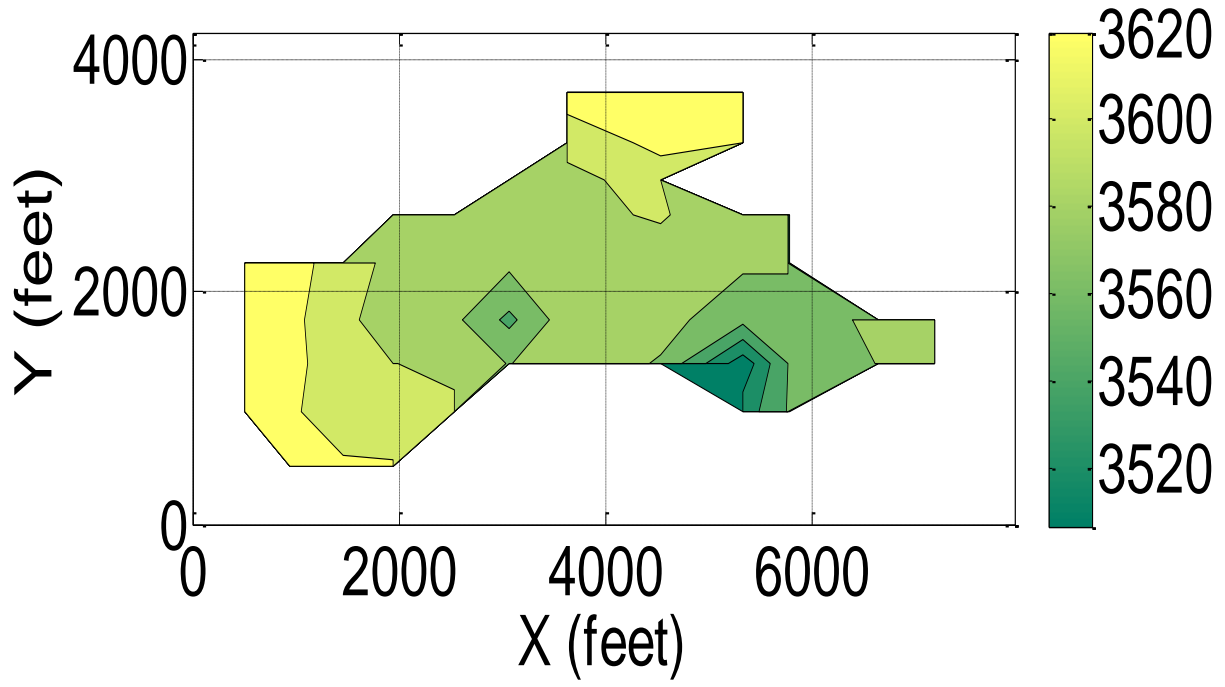
Figure 34. Water pressure dissipation in A-1 reservoir after 60 days of production
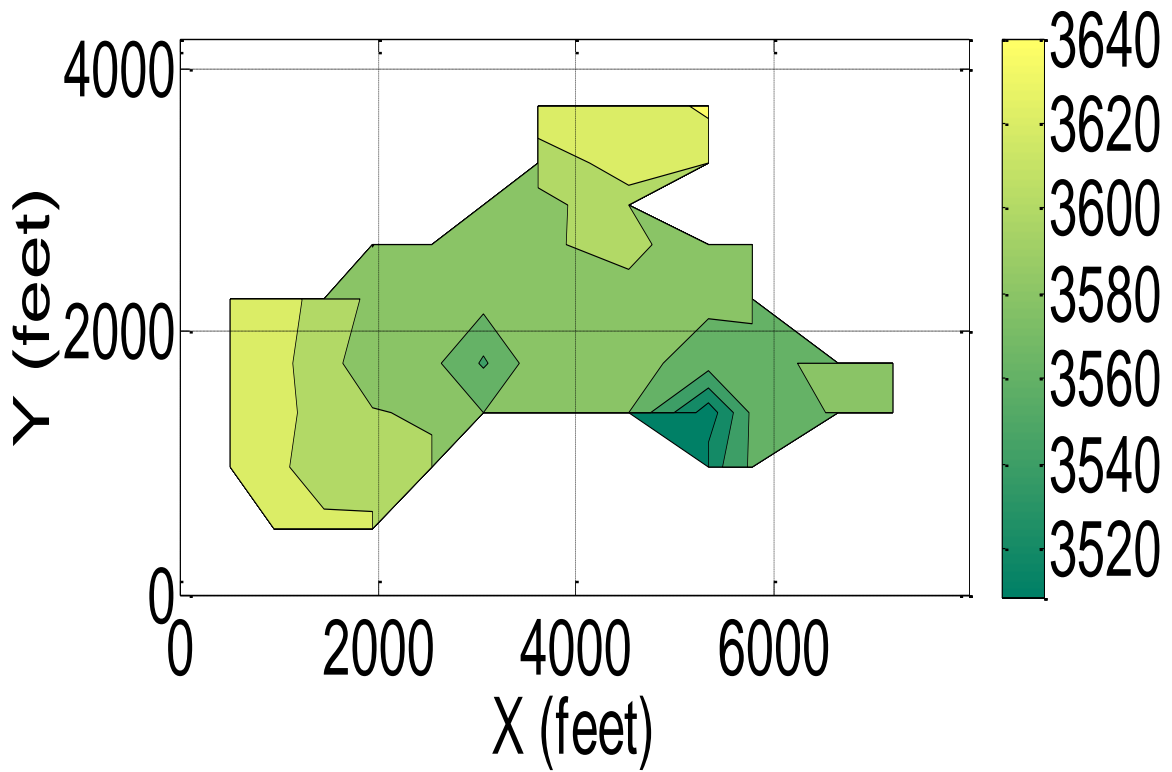

Figure 35. Gas pressure dissipation in A-1 reservoir after 60 days of production

Figures 33, 34 and 35, shows the calculated pressure distribution maps for each phase at the end of 60 days of simulation. Lowest pressure values relative to surrounding four neighboring blocks can be seen in the Well blocks hosting the five producing wells. Highest pressure values are observed on the western portion and decrease significantly towards the eastern portion of the field.
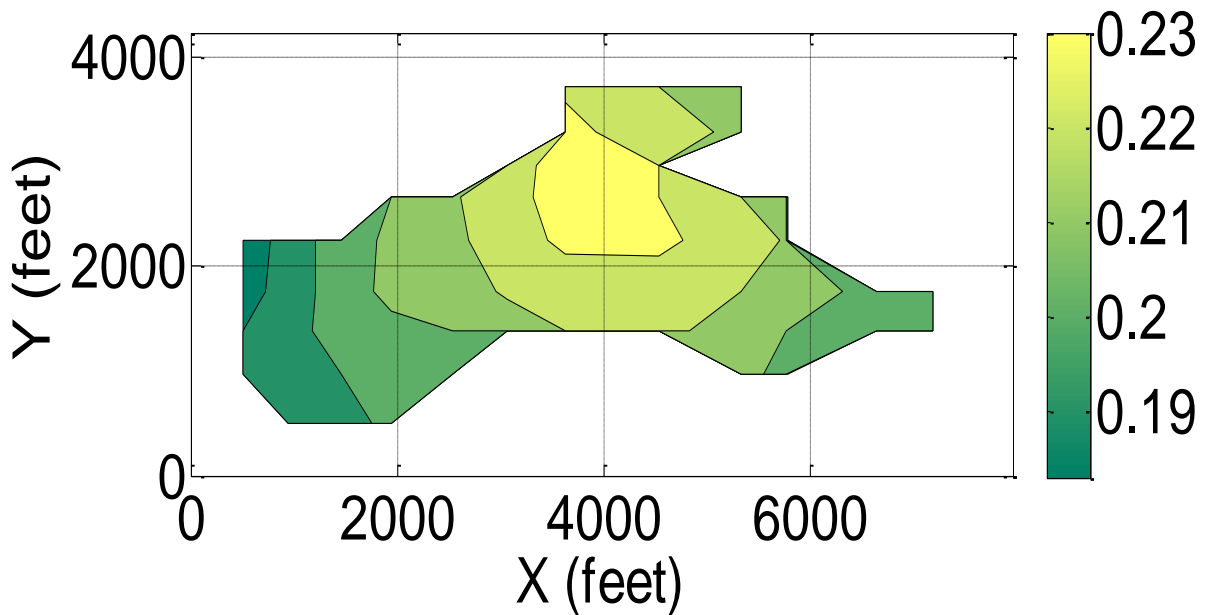
4.1.2 Porosity Maps

Figure 36. Field porosity distribution in A-1 reservoir after 60 days of production

Figure 36 shows the effect of pressure on the porosity of a reservoir rock as can be seen in **Equation 11,** when compared with the initial porosity distribution map **Figure 3.** Porous rocks buried underneath are subject to both internal and external stresses. External stresses come from the weight of the overburden (typically 1 psi/foot) while internal stresses are as a result of fluid pore pressure. Both stresses have opposing effects as external stresses tend to compress rock reducing pore volume whereas internal stress resist pore volume production. When fluids are produced from reservoir pore space, pore pressure decreases significantly, as such the external stresses tend to override the effect of internal stresses, resulting in decrease in pore volume and effective porosity as can be seen in the final porosity map **Figure 36.**
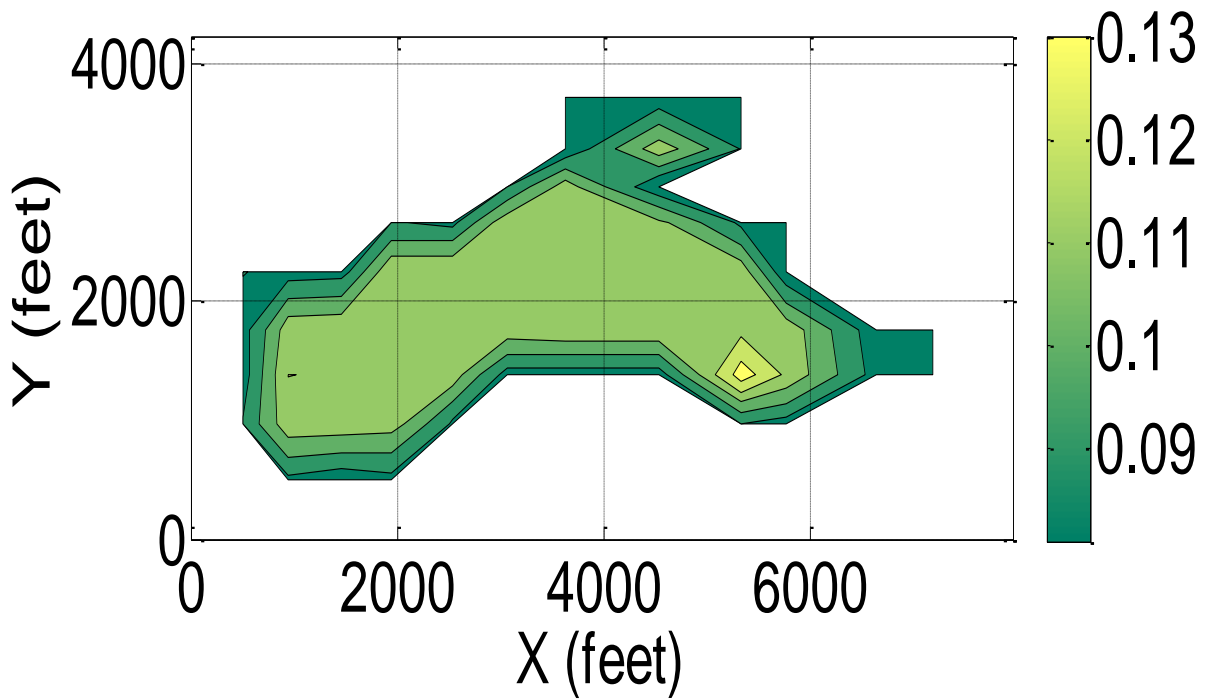
4.1.3 Saturation Maps

Figure 37. Gas saturation distribution in A-1 reservoir after 60 days of production
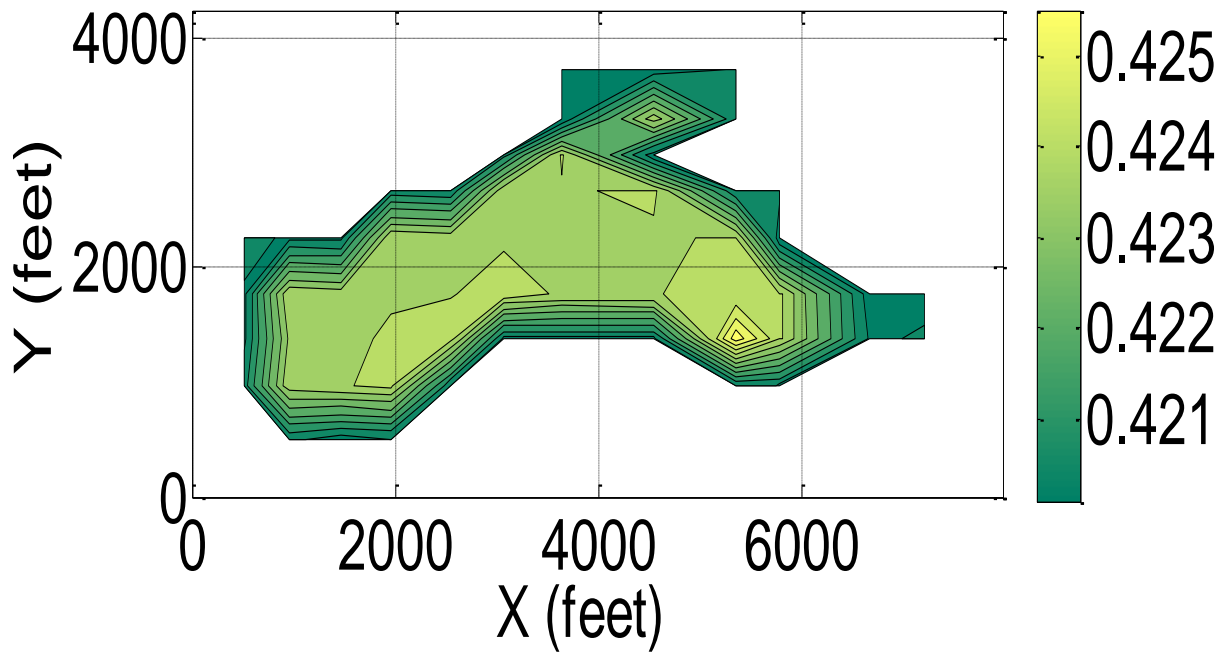

Figure 38. Water saturation distribution in A-1 reservoir after 60 days of production
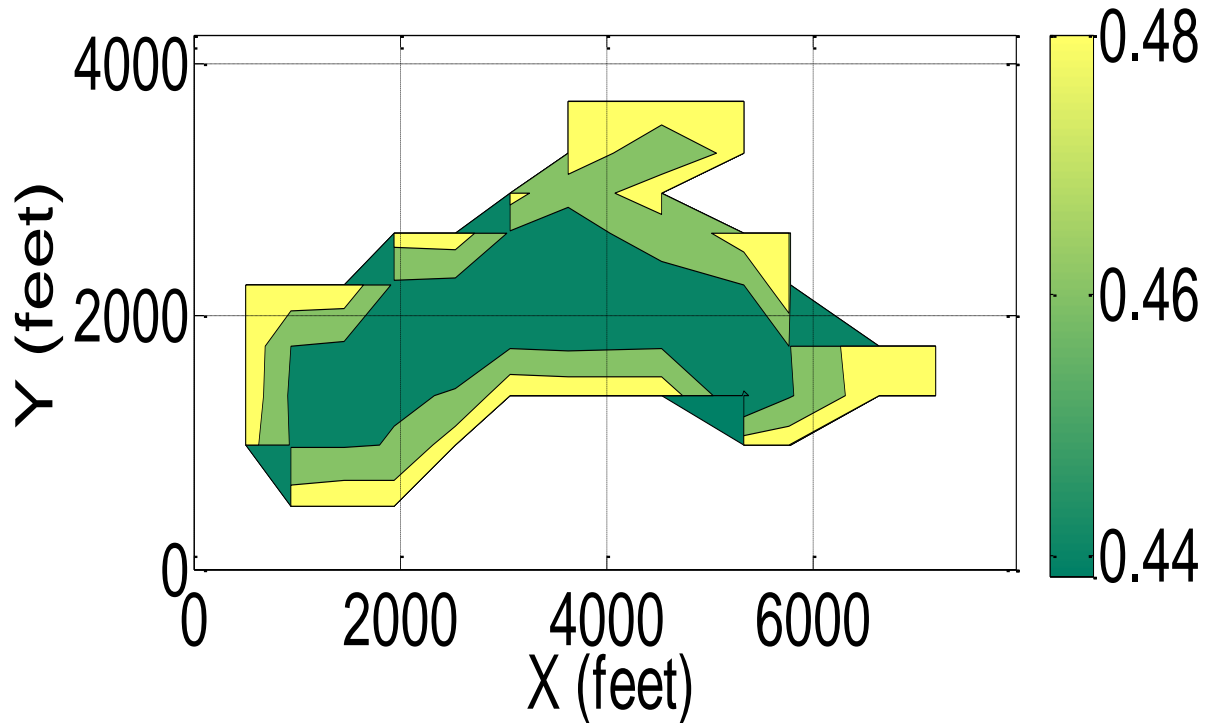
Figure 39. Oil saturation distribution in A-1 reservoir after 60 days of production

Figure 37, 38 and 39, gives the calculated saturation distribution maps for each phase at the end of 60 days of simulation. Phase saturations are fairly distributed throughout the field except for the region where the pressure specified well is located that shows some disparity. Fluid production decreases reservoir pressure, more gas is released from solution which expands to occupy a larger fraction of the pore space. As a result, oil saturation decreases by 8 to 12% on average, and is compensated for by an increase in gas phase saturation. Peak values of gas and water saturations can be seen in the far northern and southern portions of the reservoir. Oil saturation is somewhat evenly distributed within the field, ranging from 44 to 48 % and averaging 46% for the field. Water saturation values range from 42 to 42.58% and gas saturation values from 8 to 13%.

4.1.4 Production History

The production history is emblematic of solution- gas expansion drive reservoirs. Initial production rates were high with a rapid decline in production and bottom-hole pressures. Since 1961, the field production has declined annually and presently only eight wells are producing, the rest of which are either shut-in or converted to water injection wells. Casing was run through the sands and the zones of interest were perforated from reviewing both electrical and Micro logs. Perforated wells were placed on pump using no artificial stimulation. Only five of these wells were considered for this simulation study and the reservoir was analyzed only for primary production.

Feasibility studies conducted for either a gas injection or a waterflood as a secondary recovery program were debated. The field was unitized in 1958 and in 1959, the Engineering committee settled for a water flooding scheme [52].
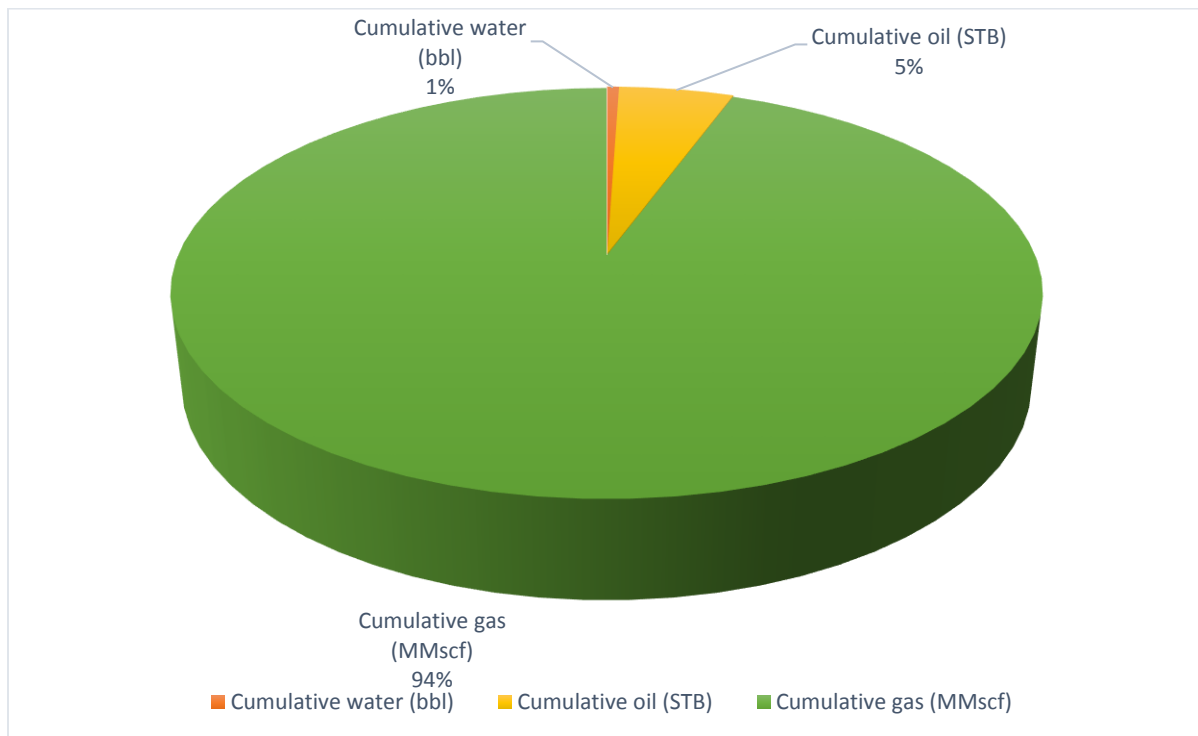

Figure 40. Phase cumulative production for 60 days

Figure 40 shows the amount of fluids realized for each of the phases at the end of the required simulation time of study. Primary recovery factor (RF) for oil, water and gas phase for the A-1 reservoir is obtained from the following expression as the ratio of the cummulative producion of phase (Cum_phase) to the original amount of phase present (OIP).

$$RF(\%) = \frac{Cum\_phase}{OIP} X\ 100 \tag{106}$$

Table 7. Recovery Factor Calculations at the end of 60 days of simulation

Phase Bbl/SCF	Cumulative of phase	Amount of phase initially present	Recovery factor (RF) %
Oil	33083	3471380	0.95
Water	3390	4159756	0.08
Gas	611230016	1457383658	42

For a period of 60 days, 40 % of the initial gas in place was recovered together with very negligible amounts of oil and water initially in place as can be seen in the above table.

The ratio of water produced compared to the total volume of liquids produced per well (f_w) was calculated from the following expression and corresponding fractional flow curves for all five wells were plotted as in **Figure 41**.

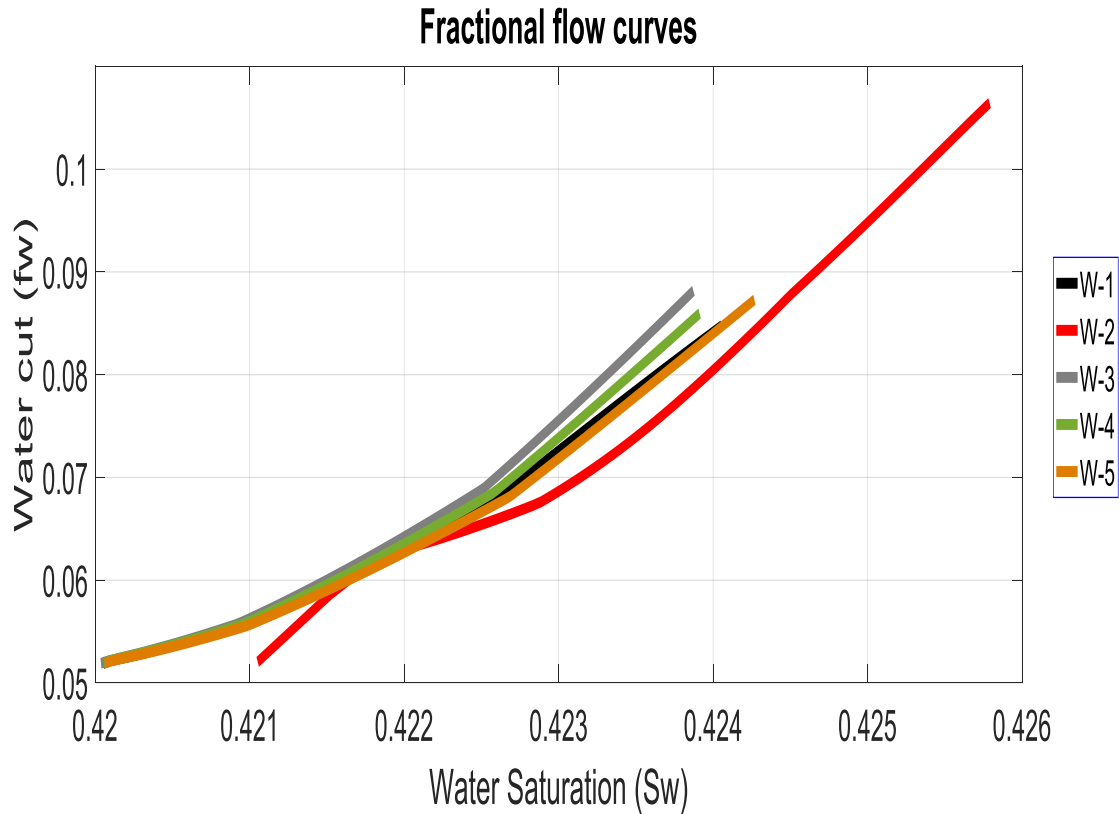$$f_w = \frac{B_w q_{wsc}}{B_o q_{osc} + B_w q_{wsc}} \tag{107}$$

Figure 41. Fractional flow curve portraying the rate at which water moves through the porous medium.

More gas was produced relative to oil and water in this field. The pressure specified well $(W - 2)$ had the highest amounts of oil, water and gas production recorded in the field over a period of 60 days.

Flow rates and bottom-hole pressures simulated per well were matched with those recorded in literature [27]. Suitable matching in production data was obtained which validated the model. Mobility method of allocation was used in partitioning flow rates. This method eliminated stability issues by assuming negligible capillary pressures at the well blocks, **Equations 76 and 77**. However, this assumption could be responsible for the slight discrepancies observed between results in the literature and those simulated. History matched data for two wells are reported below, the rest of which are included in Chapter 8.

4.1.4.1 History Matching for Field Wells
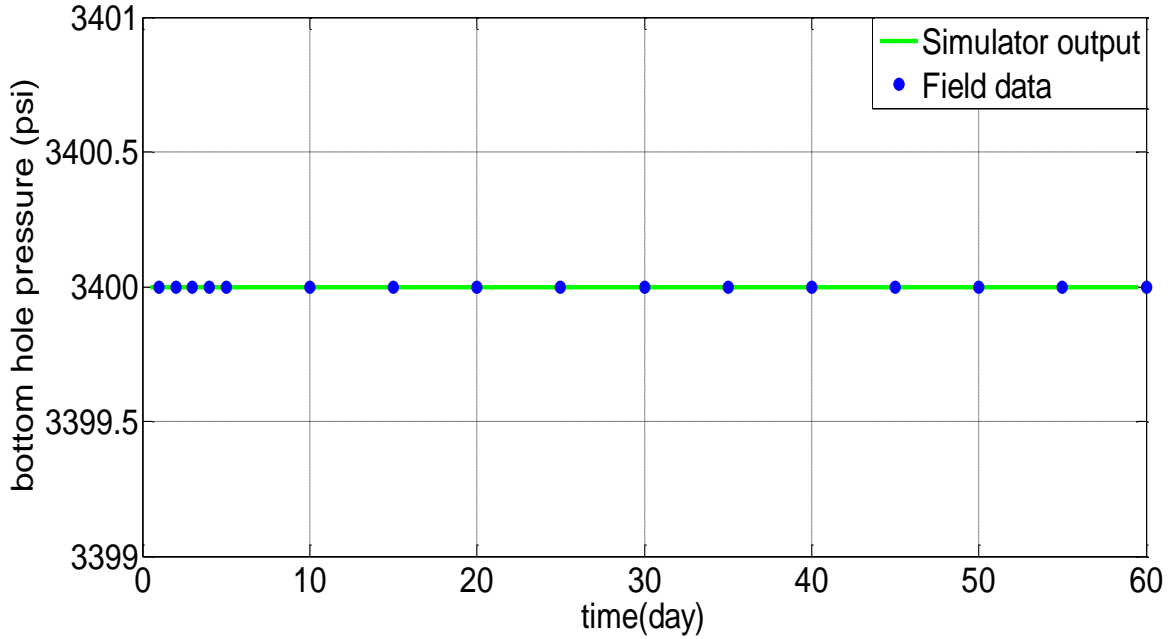
4.1.4.1.1 Pressure Specified Well

Figure 42. Bottom-hole pressure for pressure specified well, (W-2)
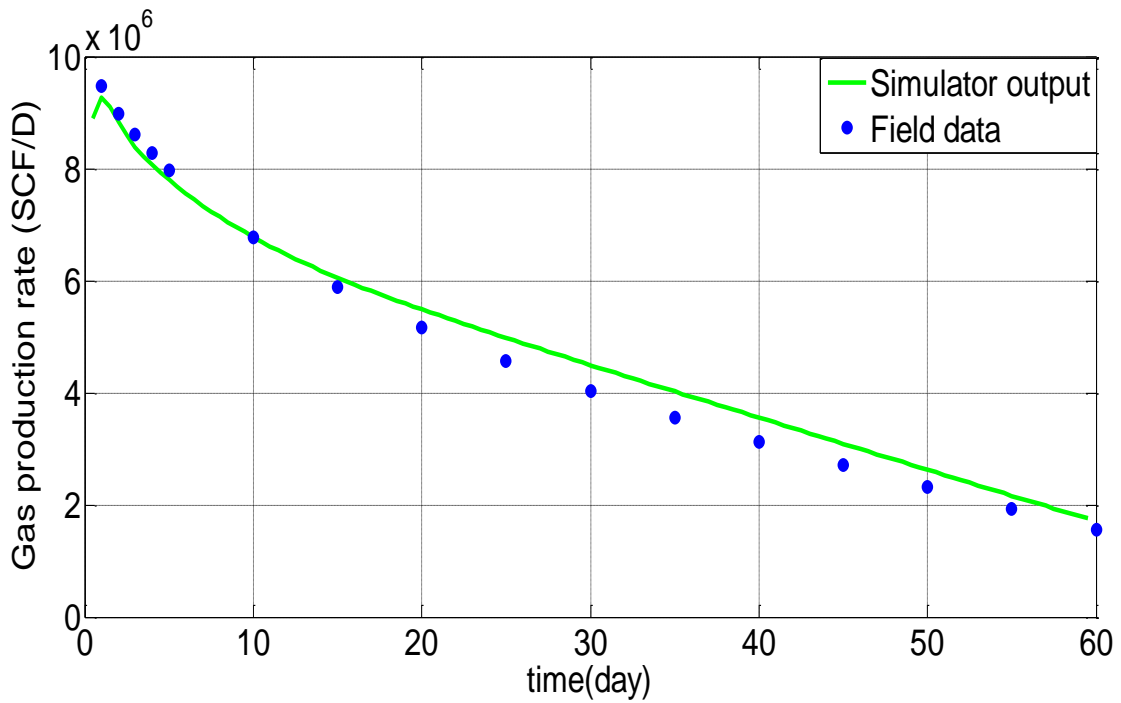

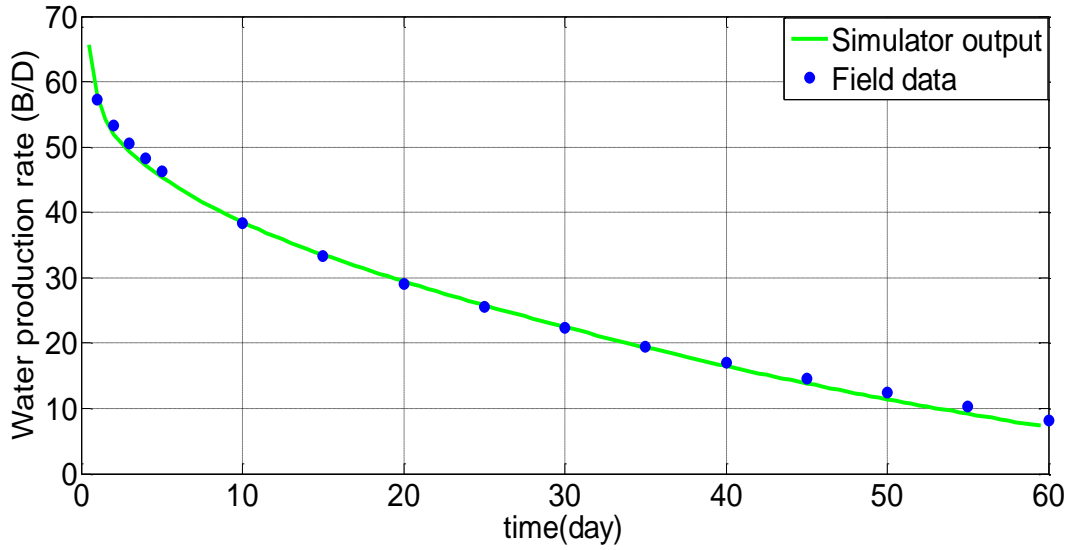*Figure 43. Gas production rate for pressure specified well, (W-2)*

Figure 44. Water production rate for pressure specified well, (W-2)

Figure 45. Oil production rate for pressure specified well, (W-2)

Figures 42, 43, 44 and 45 shows the bottom-hole pressures, oil, water and gas production rates realized for $(W - 2)$. In this well, the boundary condition specification is that of a constant flowing sand face pressure of 3400 psia. Well $(W - 2)$ responds to this boundary specification by producing on average 5.75 million standard cubic feet of gas, 38 barrels of water and 525 stock tank barrels of oil. Oil, water and gas production rates for this well were the highest observed for the field.

4.1.4.1.2   Gas Rate Specified Well

Figure 46. Bottom-hole pressure for gas rate specified well, (W-4)

Figure 47. Gas production rate for gas rate specified well, (W-4)

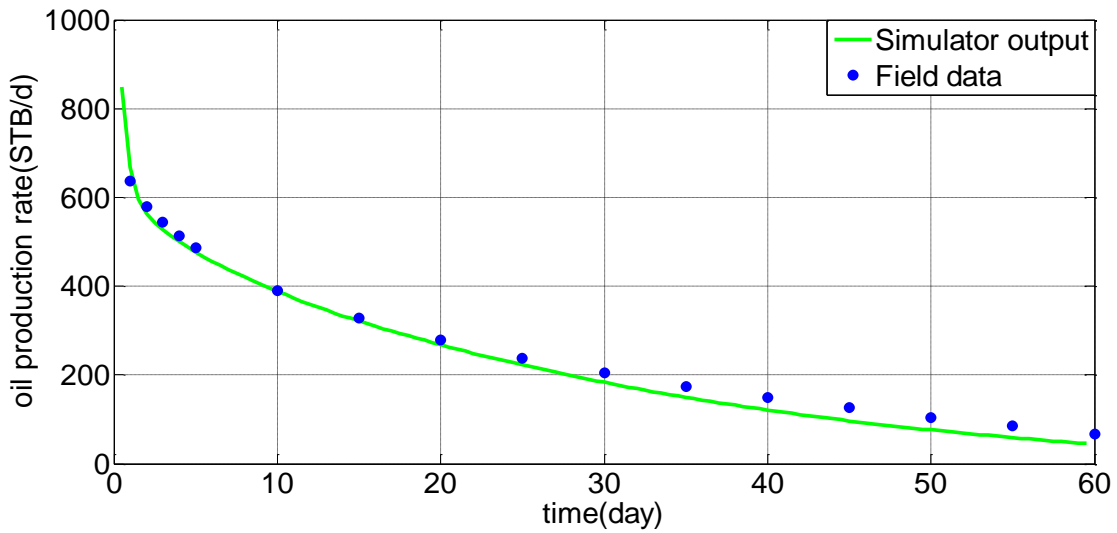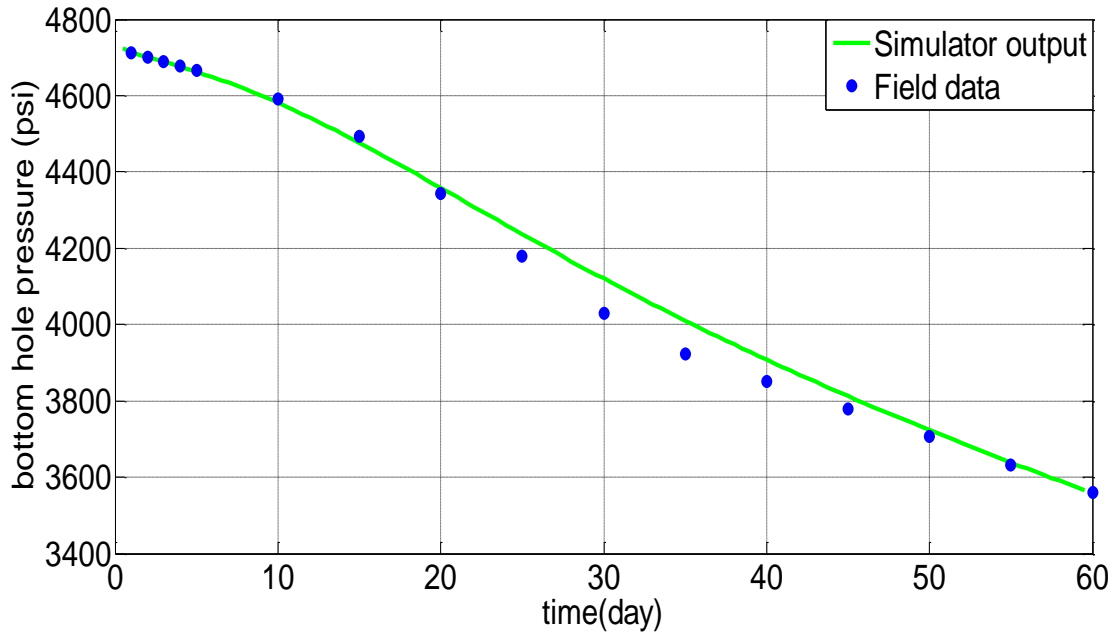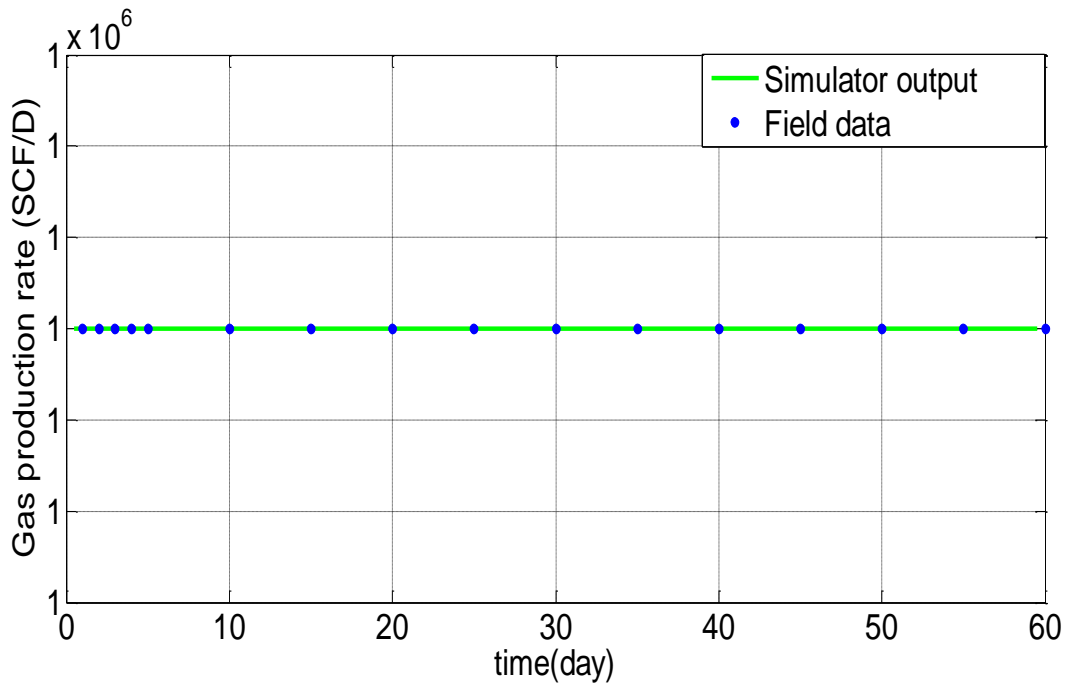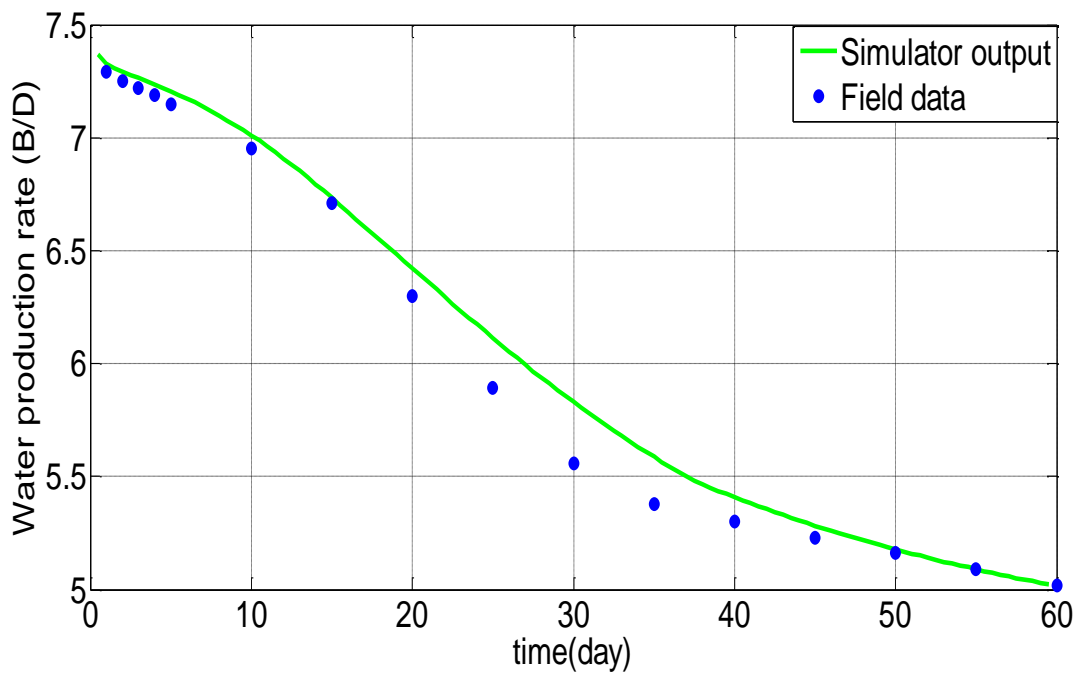*Figure 48. Water production rate for gas rate specified well, (W-4)*
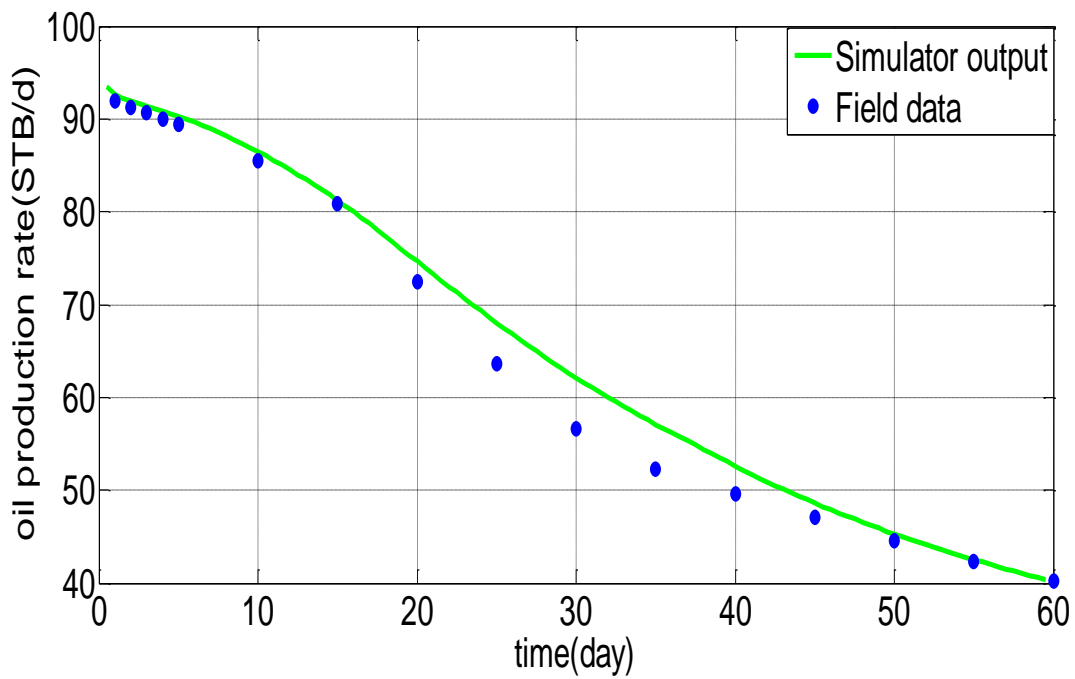
Figure 49. Oil production rate for gas rate specified well, (W-4)

Figures 46, 47, 48 and 49 shows the bottom-hole pressures, oil, water and gas production rates realized for $(W - 4)$. In this well, a gas rate production of 1MM STB/D was specified. Well $(W - 4)$ responds to this boundary specification by producing on average 66 stock tank barrels of oil and only a few barrels of water. Oil production decreased significantly from 92 STB after the first day to 40 STB at the end of 60 days. Similarly, water production decreased from 7.4 barrels after the first day to 5 barrels at the end of 60 days whereas gas production remained constant at 1 million standard cubic feet of gas. **Figure 50** is a comparison of the average fluid production rate realized for all five wells simulated in this study.
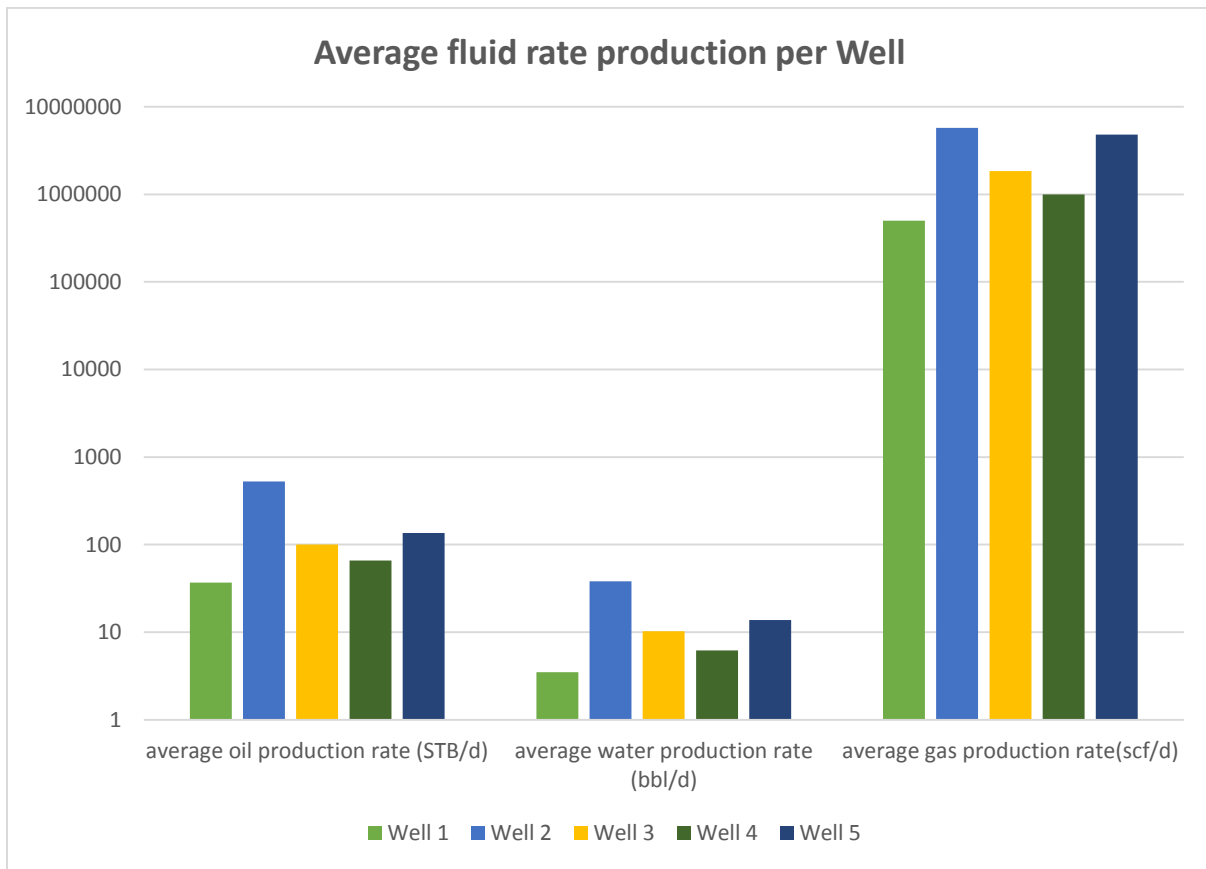
Figure 50. Comparison of average rate production per well after 60 days of run time.

4.1.5 Material Balance Check
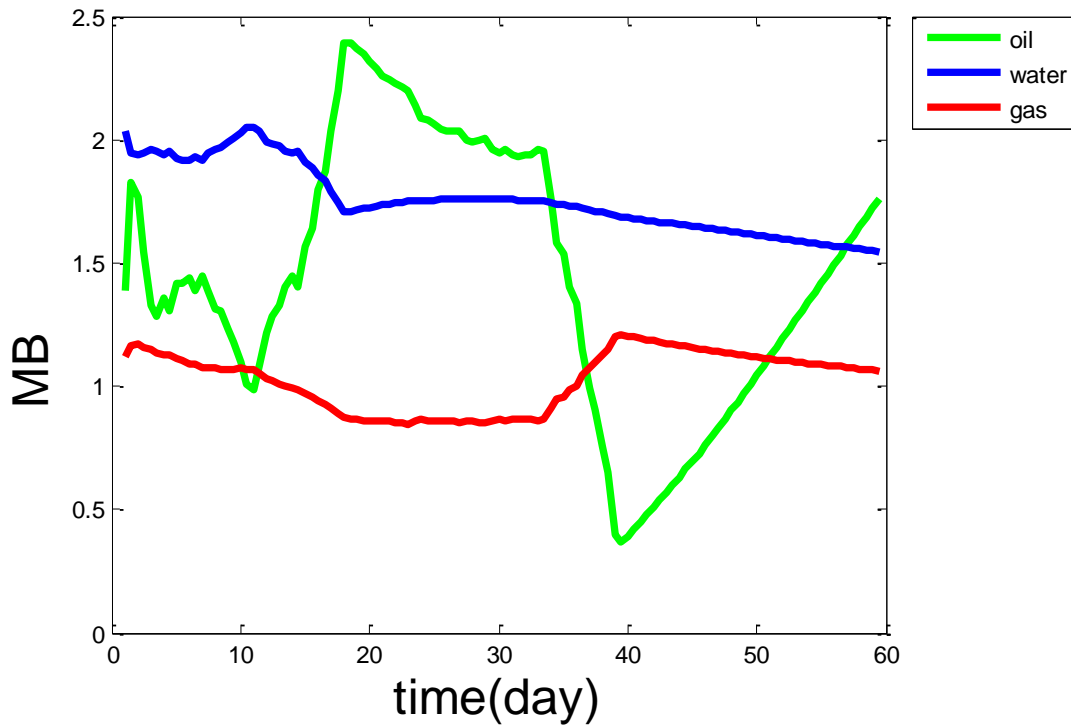
Figure 51. Fluid balance check for fluid flow through control volume (A-1 reservoir).

A perfect material balance of unity is achievable if the mass entering the reservoir is equal to the mass leaving the reservoir. Material balance checks conducted on the A-1 reservoir for oil, water and gas flow has values that fluctuate from 0.5 to 2.5 as can be seen in **Figure 51** . These inadequacies could be as a result of the numerous approximations made in the solution process and computer errors.

4.2   Phase II Results

4.2.1 Factors Affecting Fracturing Fluid Cleanup

At the close of a fracture treatment process, gel residue resides in and around the fracture obstructing the free flow of hydrocarbons. A fracturing cleanup process is needed to transport these residues from the fracture back to the Earth's surface. Several factors have been investigated and reported in the literature to significantly affect the effectiveness of the fracturing fluid cleanup process and gas production in tight gas reservoirs. The objective of this study has been to analyze the effect of increasing breaker concentration on broken gel viscosity and yield stress of filter cake, capillary pressure, fracture conductivity, fracture length, aqueous phase trapping and formation damage on the fracturing fluid cleanup process. However the effect of non–Darcy flow and stress dependency of tight reservoir rocks has been neglected for the sake of simplicity. The gas relative permeability is permanently cut due to water retained in the invasion zone [53]. Inadequate fracturing fluid cleanup results in a lag in gas breakthrough at the wellbore, gas production is only observed after the first few time steps. The fracture width is slightly increased to maintain numerical stability in the model and the porosity decreased to preserve the material balance. 200 barrels of water was distributed around the fracture to create the initial conditions for all the runs. The total gel volume in the fracture at the end of fluid injection was 638 bbls. The factors under consideration which significantly hamper fluid recovery were investigated for a total simulation time of 100 days and the observed trends are reported as follows;

4.2.1.1 Effect of Fracture Conductivity

Fracture conductivity is a measure of how easily fluids flow through a fracture. It is a product of fracture permeability k_f and the propped fracture width reported in md/ft. Dimensionless fracture conductivity is the ratio of fracture conductivity to reservoir permeability k and fracture half length L_{xf}. It provides a means of optimizing fracture conductivity by varying fracture permeability. Overtime, the conductivity of a fracture can be significantly reduced by proppant crushing, proppant embedment into the formation, increasing stress on proppants, formation damage resulting from gel residue or fluid loss additives, non-Darcy and multiphase flow [46]. The effect of fracture conductivity for constant rheology of fracturing fluid was investigated by varying the permeability in the fracture while keeping fracture length constant.
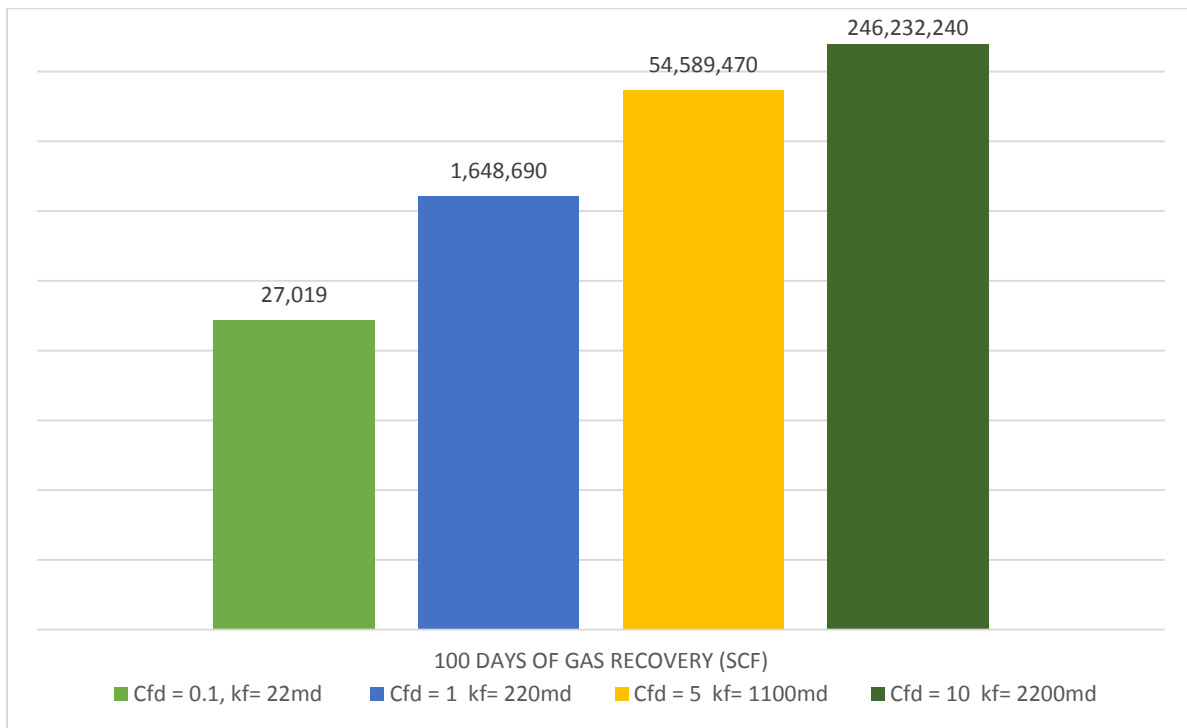
Figure 52. Cumulative gas production in (SCF) at different fracture conductivities after 100 days of run time, for τ_0=5 Pa, n=0.5 and k '=200 $mPa.\,s^{n'}$
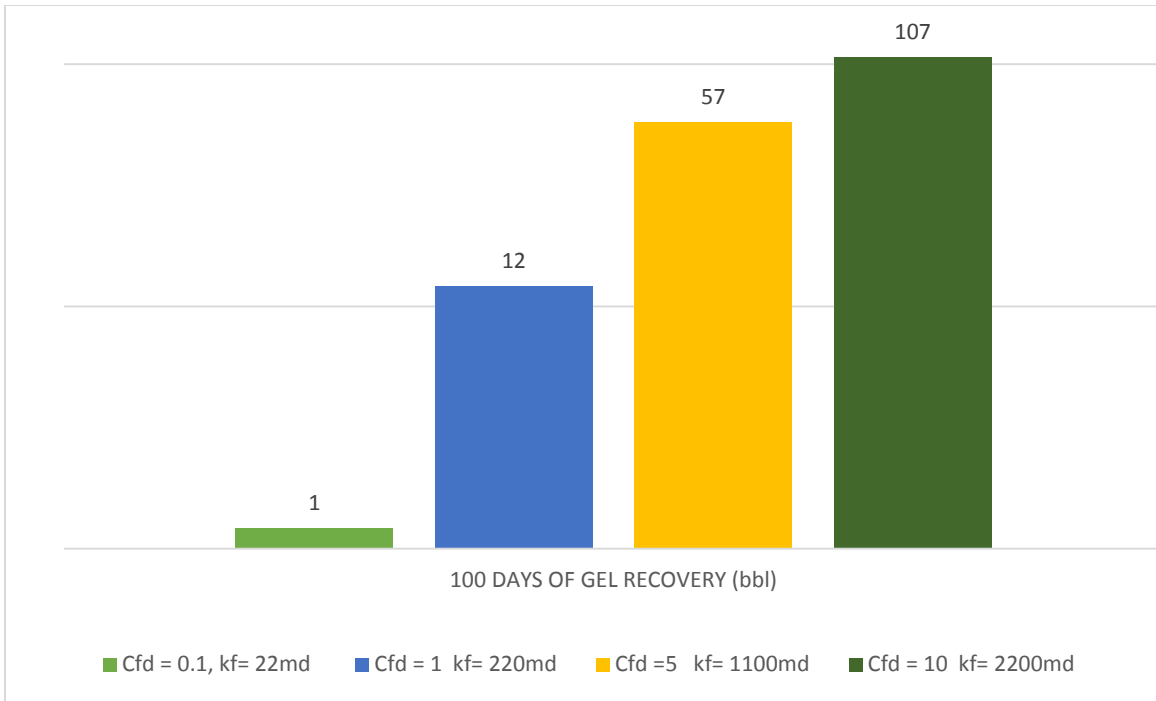
Figure 53. Cumulative gel production in (bbl) at different fracture conductivities after 100 days of run time, for τ_0=5 Pa, n=0.5 and k'=200 $mPa.s^{n'}$

Table 8. Summary of cumulative production for the different fracture conductivities.

Fracture conductivity (C_{fd})	Fracture permeability (k_f/md)	Formation permeability (k/md)	Cumulative gas (scf)	Cumulative gel (bbl)
0.1	22	0.05	27019	1
1	220	0.05	1648697	12
5	1100	0.05	54589477	57
10	2200	0.05	246232247	106

Figure 54. Effect of fracture Conductivity on gel saturation distribution along the fracture for k =0.05 md, K' = 40, τ_0=1Pa, n' = 0.5 after 100 days of run time.

Fluid flow rate in a fracture is proportional to its conductivity, by increasing the fracture conductivity, the fracture cleans up faster and both gas and gel production increase as can be seen in **Figures 52 and 53**. However, the gel production will continue to increase only if the pressure gradient along the fracture grids remains greater than the yield stress required for the fluid 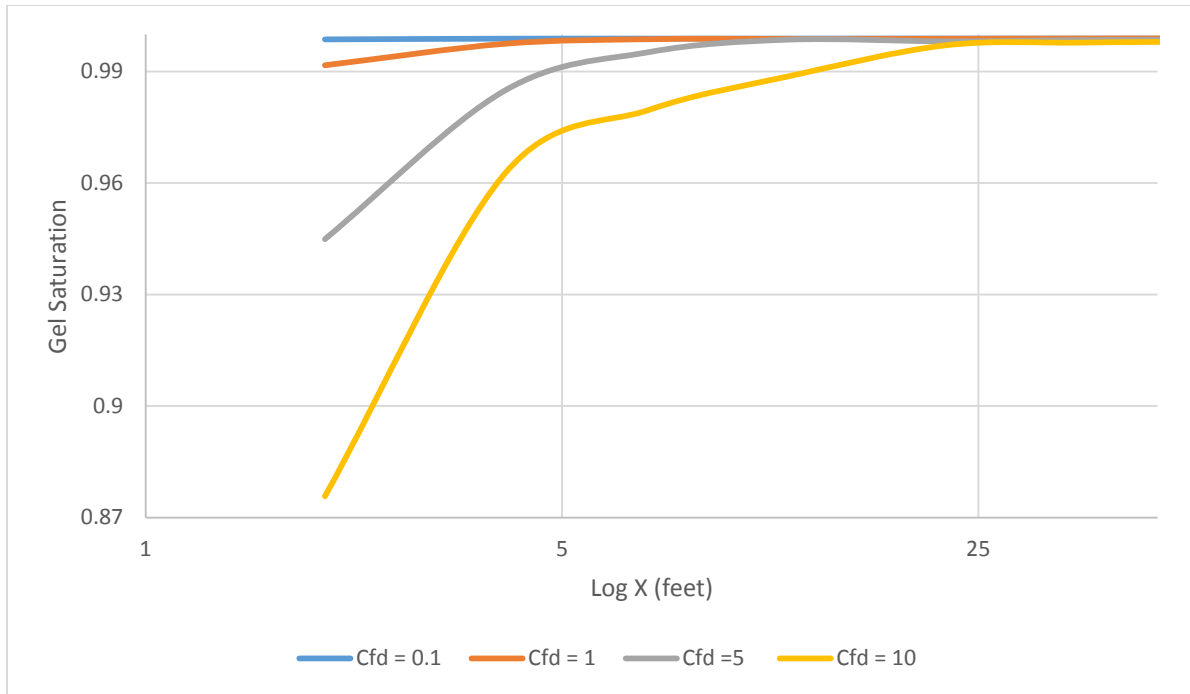to move [23]. **Figure 54** shows quite a bit of an effect of fracture conductivity on gel saturation distribution along the fracture face. Increasing dimensionless fracture conductivities from (0.1 to 1) has a lower effect on cumulative gel production compared to the increase from (1 and 10) as can be seen in **Figure 53**. No water production is observed within this production period due to the high capillary forces in the formation. Increasing the fracture conductivity from 1 to 10 shows a terrific increase in cumulative gas production relative to an increase in fracture conductivity from 0.1 to 1. However, increasing the dimensionless fracture conductivity for a tight gas reservoir to values higher than 10 would not considerably increase gas flow rates [7], neither does the effect of dimensionless fracture conductivity increase with increasing reservoir-matrix permeability [23]. The created fracture permeability is extensively greater than the formation permeability as such fracture networks have the potential for being highly effective pathways for conducting fluid [54].

4.2.1.2   Effect of Increasing Breaker Concentration on Yield stress and Broken Gel Viscosity

Most fracturing fluids are yield stress fluids having a tendency to a dual state depending on the magnitude of the shear applied. They are inclined to act as solids before yielding and as fluids only when their yield stress is exceeded. It is more realistic to regard a yield stress substance as a fluid whose viscosity as a function of applied stress has a discontinuity as it drops sharply from a very high value on exceeding a critical yield stress [54]. Herschel Buckley model proposed by Yi [51] allows for power law behavior even after the fluid yield stress is exceeded. Cumulative gas production for an initial guar concentration of $200 \ lb/Mgal$ were simulated for the effect of increasing breaker concentration on yield stress of filter cake using correlations reported in Ben et al [47] , and shown in **Figures 30 and 31**.

$$y = -3 * 10^{-5} \ x^3 + 0.0123 \ x^2 - 0.9313 \ x + 19.828$$

$$(108)$$

where y and x are yield stress in Pa and polymer concentration in $lb/Mgal$ respectively. This equation is valid for polymer concentrations in the range of $0 - 200 \ lb/Mgal$.

$$v = -0.0439 \ u^3 + 1.3548 \ u^2 - 14.6 \ u + 62.179$$

$$(109)$$

and v and u are polymer concentration in $lb/ Mgal$ and breaker concentration in $gal/Mgal$. This equation is valid only for a polymer concentration of $200 \ lb/Mgal$.

Figure 55. Cumulative gas production in (SCF) showing the effect of increasing breaker concentration on fracturing fluid yield stress (constant values) and gel viscosity after100days of run time, for Cf_d = 1, k= 0.05 md
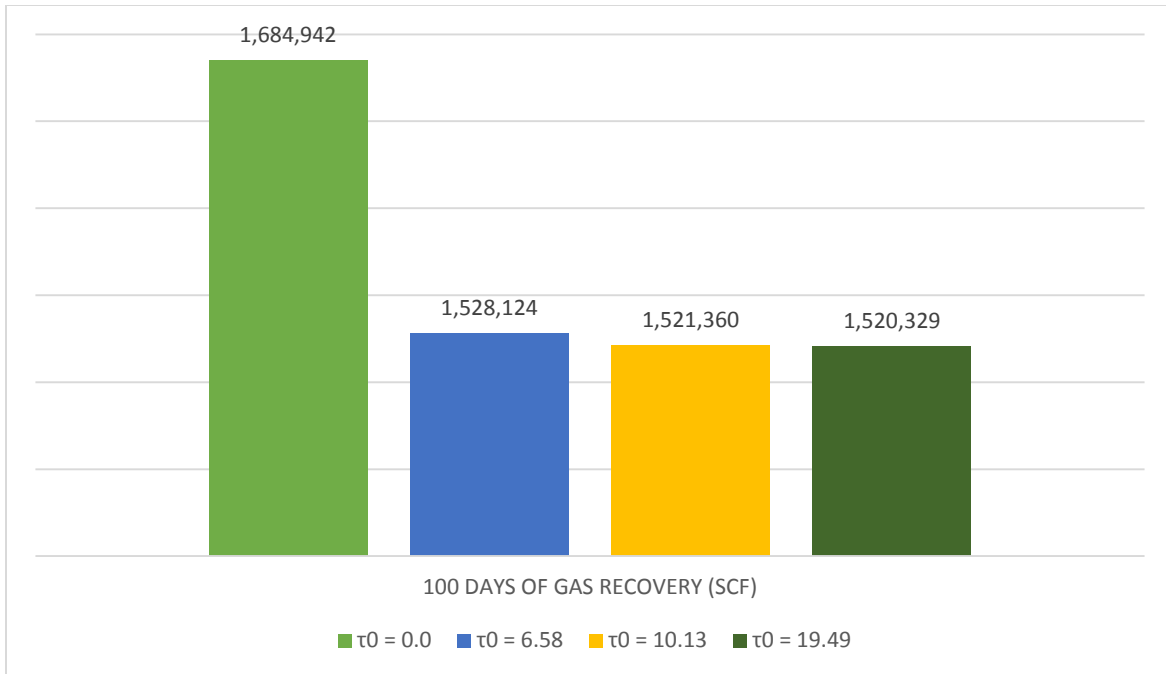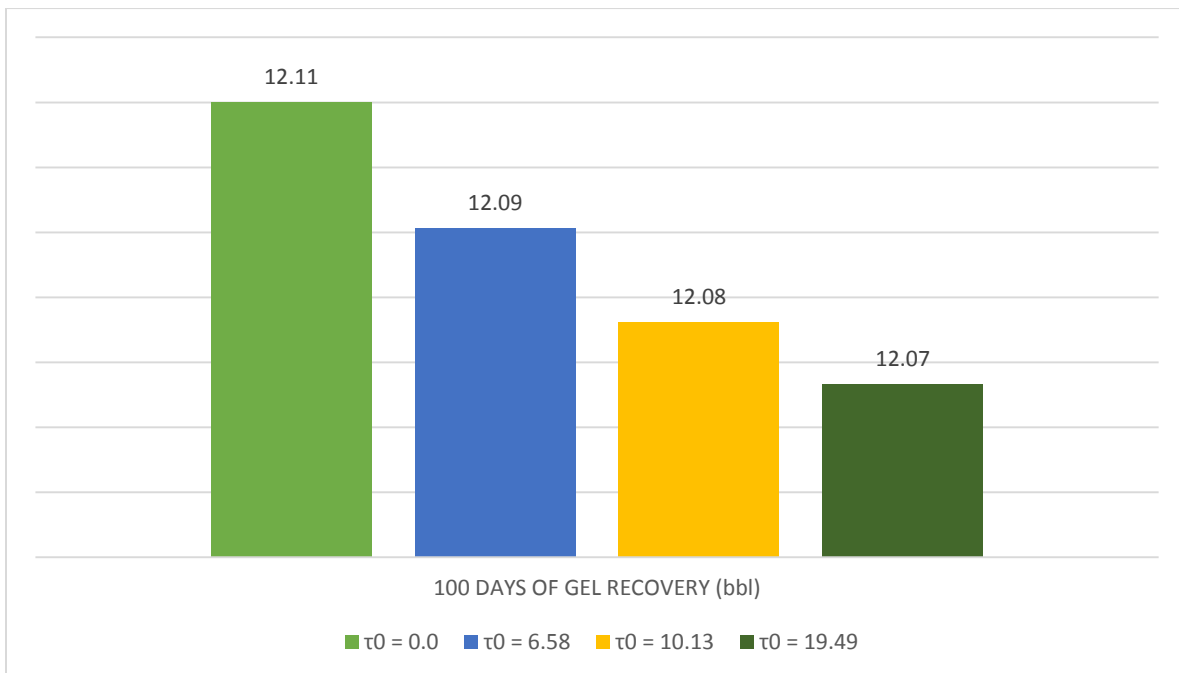

Figure 56. Cumulative gel production in (bbl) showing the effect of increasing breaker concentration on fracturing fluid yield stress (constant values) and gel viscosity after 100 days of run time, for Cf_d = 1, k= 0.05 md

Table 9. Cumulative fluid production showing the effect of increasing breaker concentration on fracturing fluid yield stress (constant values) and gel viscosity, for Cf_d = 1, k= 0.05 md

Breaker Conc. $(gal/Mgal)$	Fluid yield stress (τ_0/Pa)	Fluid consistency index (k') $(mPa.s^{n'})$	Fluid flow behavior index (n')	Cumulative gas (scf)	Cumulative gel (bbl)
15	0.0	40	0.5	1684942	12.11
10	6.58	60	0.5	1528124	12.09
8	10.13	75	0.5	1521360	12.08
5	19.49	80	0.5	1520329	12.07

Increasing the breaker concentration/enzyme activity reduces the yield stress of gel as per the correlation of Ben et al [47], resulting in an overall increase in cumulative gas and gel production **Table 9**. A breaker concentration of 15 $gal/Mgal$ was required to fully degrade yield stress of polymer gel, thus resulting in a near Newtonian fluid. **Figures 55 and 56** shows cumulative gas and gel production for increasing values of yield stress and viscosity respectively. Increasing the yield stress and viscosity of the fracturing fluid adversely affects gas and gel production. For lower values of yield stresses ($\tau_0 = 0.0\ Pa$), the fracture cleans up faster and cumulative gel production is higher compared to when the yield stress is increased to ($\tau_0 = 6.58, 10.13, 19.49\ Pa$). Similarly, cumulative gas production is highest for the lowest value of yield stress ($\tau_0 = 0.0\ Pa$) than for when it is increased to higher values ($\tau_0 = 6.58, 10.13, 19.49\ Pa$) for a total simulation time of 100 days. Filter cake formation and gel residue pore blocking is one of the major factors affecting the efficiency of a fracturing fluid cleanup process. If the pressure drawdown in the fracture is not high enough as to overcome the yield stress of the fluid, the gel stays in the fracture and reduces the pore space or the permeability open to gas flow. As such the correct breakers are required to completely degrade the gel for the fracture treatment process to be successful.

High Capillary forces in the formation causes water to be further imbibed into the formation. Fluid loss volume decreases as we move further down the fracture face away from the injection well, creating the invaded zone as seen in **Figure 57**.
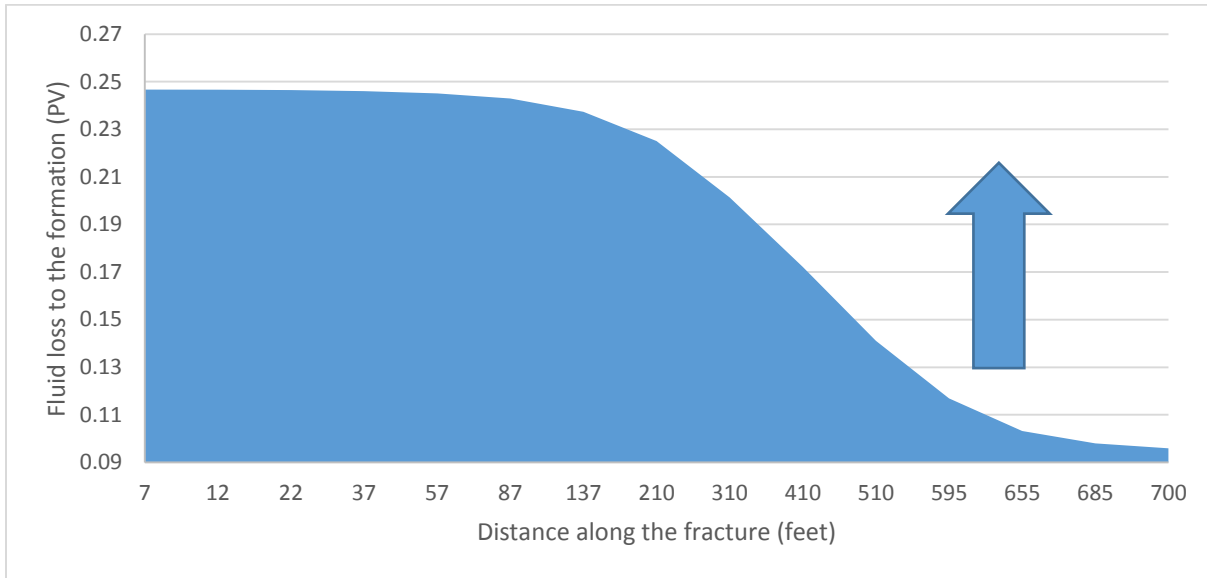

Figure 57. Invasion zone created as fluid is continuously being lost into the formation.

For Aqueous fracturing fluids, continuous water imbibition from the fracture face into the formation results in increased polymer concentration on the fracture face (filter cake build up) and consequently higher residual or yield stress values. Assuming an initial Guar concentration of $40 lb/Mgal$, the concentration of the polymer gel remaining in the fracture after 7.2 hours of fracturing fluid injection can be calculated from the following material balance equation. This is assuming that the pores are small enough that no polymer invasion occurs into the formation. This assumption is valid for tight and ultra-tight formations.

$$C_{frac} = \frac{C_i V_i}{V_{frac}} \tag{110}$$

Where C_i, the initial concentration of polymer injected and C_{frac} the concentration of polymer gel left behind in the fracture in $lb/Mgal$, V_i, the total volume of injected fluid and V_{frac}, the volume of fluid contained in the fracture pores.
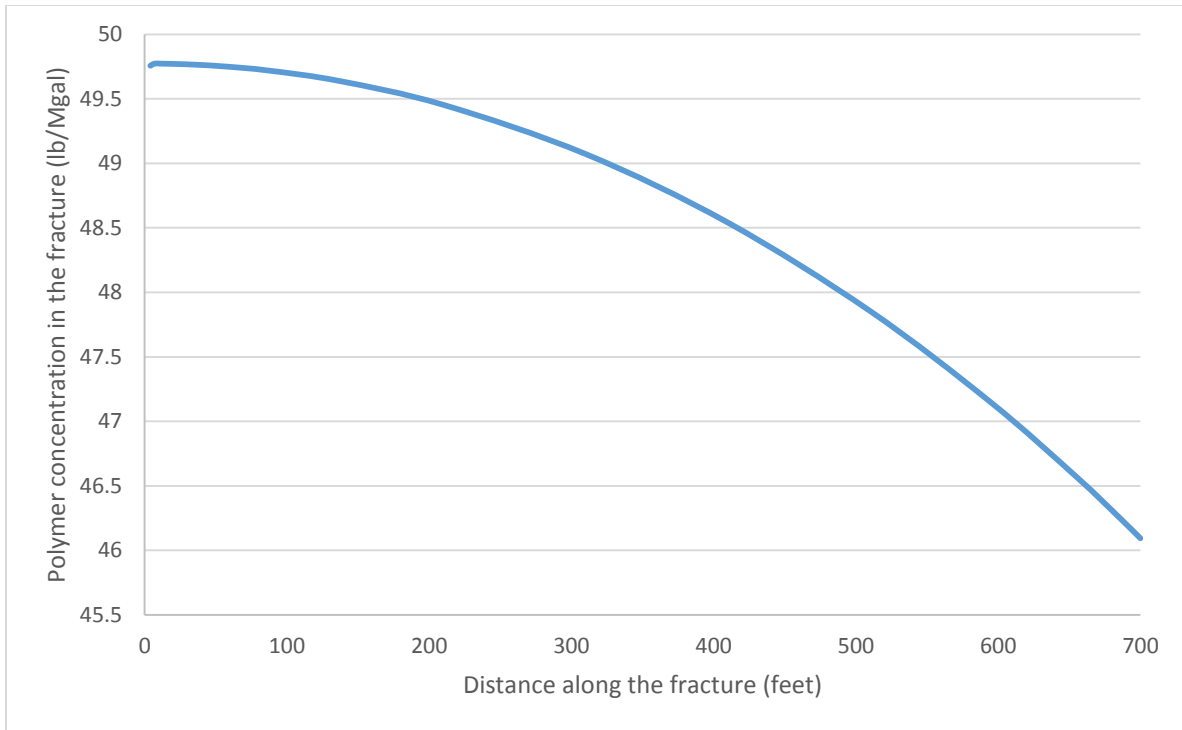
Figure 58. Polymer concentration variation with distance along the fracture face for an initial guar concentration of $40\ lb/Mgal$.

$$C_{frac} = -0.000008\ x^2 + 0.0002x + 49.765 \tag{111}$$

Figures 58 and 59 shows how polymer concentration is changing along the fracture face with distance and time. Polymer concentration decreases as we move further down the fracture and away from the injection well because the fluid volume lost to the formation decreases further down the fracture **Figure 57.** Guar concentration increases with injection time as gel residue deposited along the fracture face accumulates over time resulting in higher yield stress values. **Equations 111 and 112** are expressions which relate polymer concentration in the fracture with distance down the fracture and injection time.
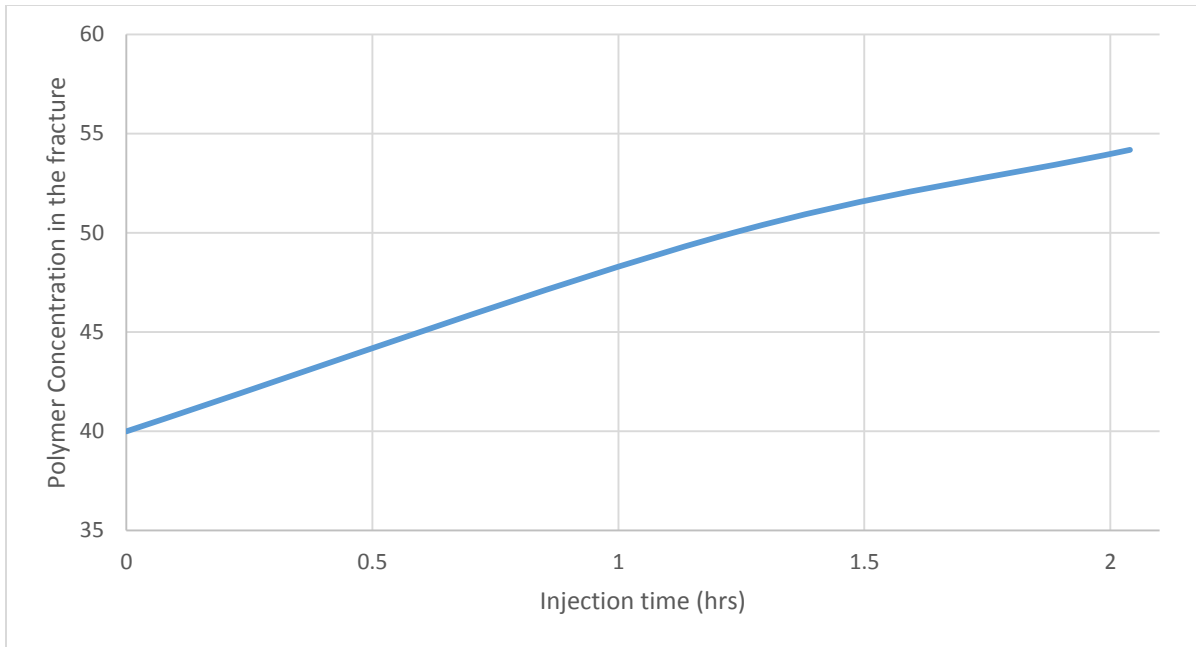
Figure 59. Average polymer concentration within the fracture face variation with injection time for an initial guar concentration of $40\ lb/Mgal$.

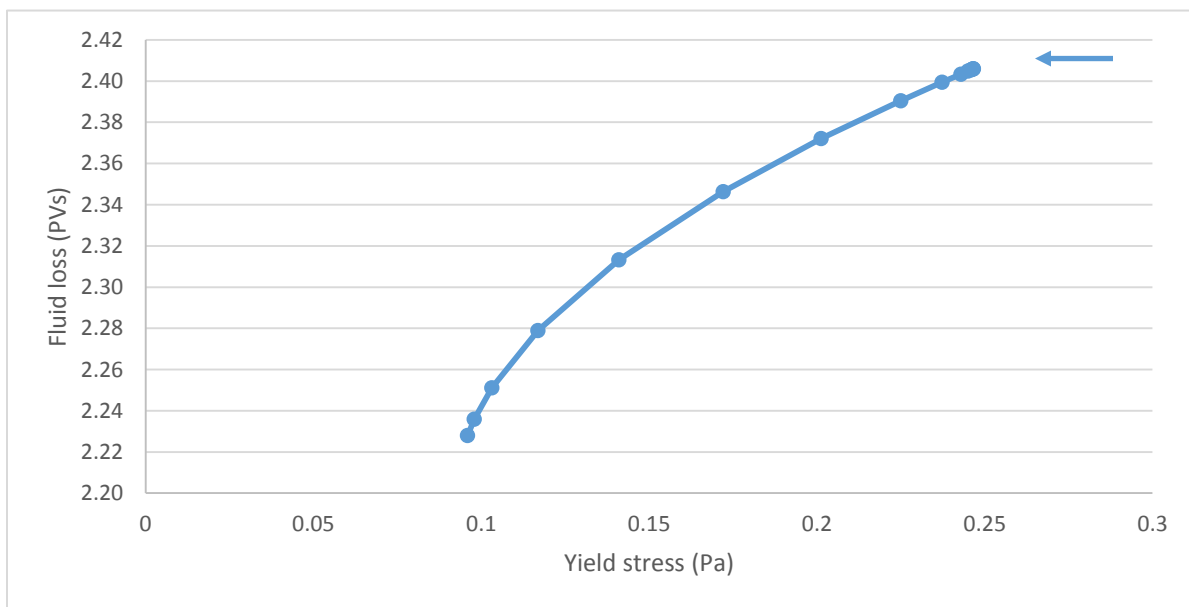$$C_{frac} = -1.4212\ t^2 + 9.85t + 40 \qquad (112)$$

Figure 60. Yield stress increasing as more fluid is being lost along the fracture face for an initial guar concentration of $40\ lb/Mgal$.

Yield stress values along the fracture face are calculated from polymer concentration according to Ben et al [47] correlation. The yield stress along the fracture face is found to increase with increasing fluid loss to the formation as in **Figure 60**. The rate at which the yield stress (τ) is increasing or the filter cake is building up is proportional to the square of the volume of fluid lost (PVs) to the formation as given by the following expression.

$$\tau = 3.4146 \, PVs^2 - 14.97PVs + 16.511 \tag{113}$$
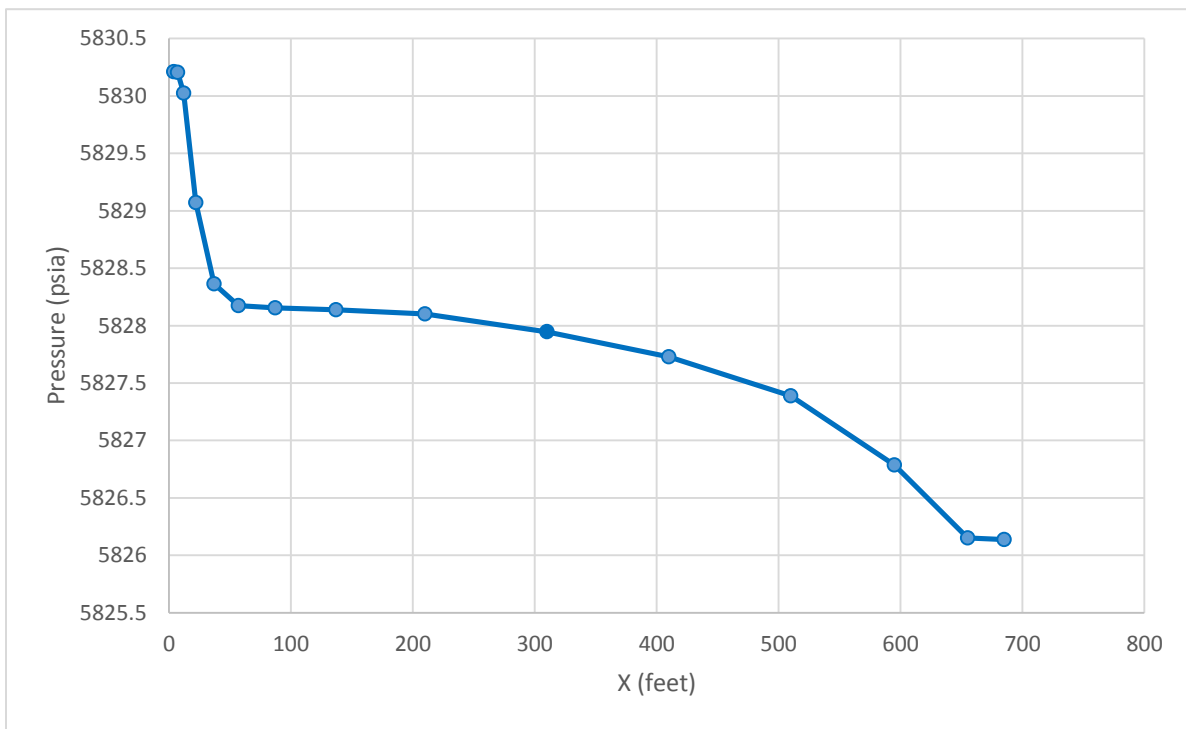
Figure 61. Pressure distribution along the fracture face for an initial guar concentration of 40 $lb/Mgal$

Pressure distribution along the fracture face for an initial guar concentration of 40 $lb/Mgal$ shows a sharp decline in pressure a few feet away from the producing well and decreases exponentially as we move further down the fracture face, **Figure 61.**

Figure 62. Yield stress variation with fluid loss volume along the fracture face for different initial guar concentrations

Figure 63. Yield stress variation with polymer concentration along the fracture face for different initial guar concentrations
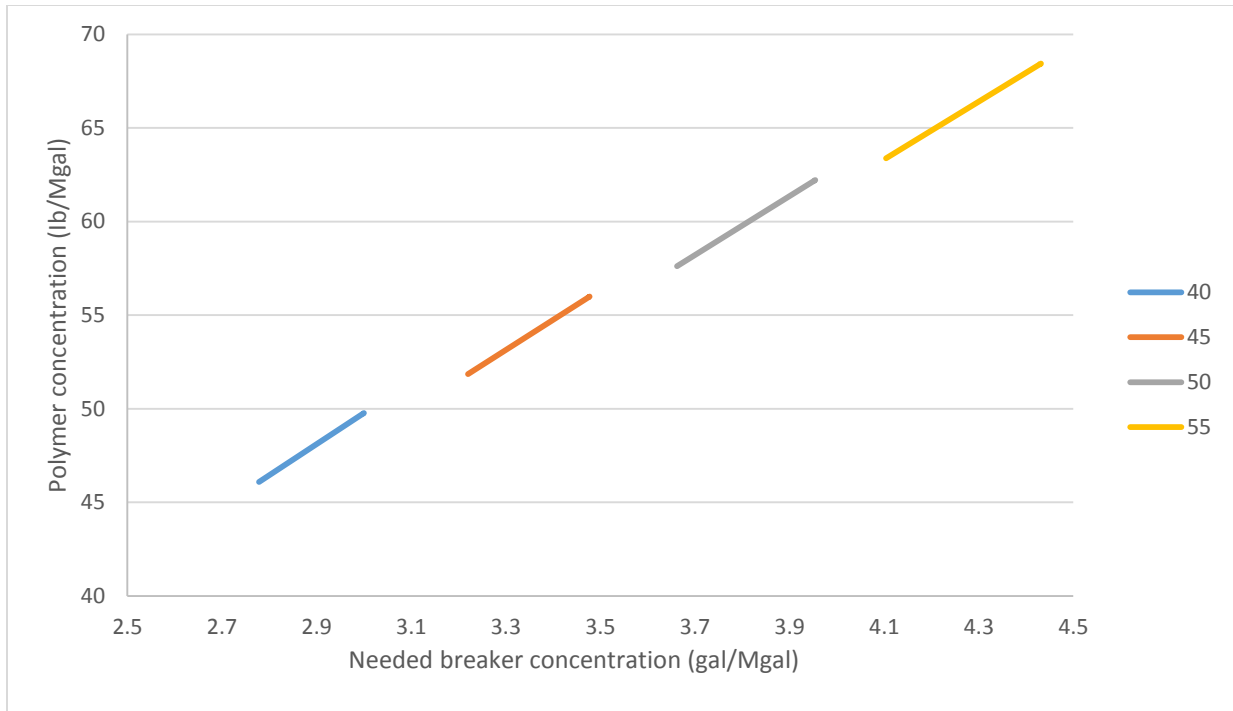
Figure 64. Showing the required breaker concentration to curb the yield stress generated along the fracture to zero for different initial guar concentrations

Several values of initial guar concentration were tested, yield stress variation with fluid loss volume, **Figure 62** and polymer con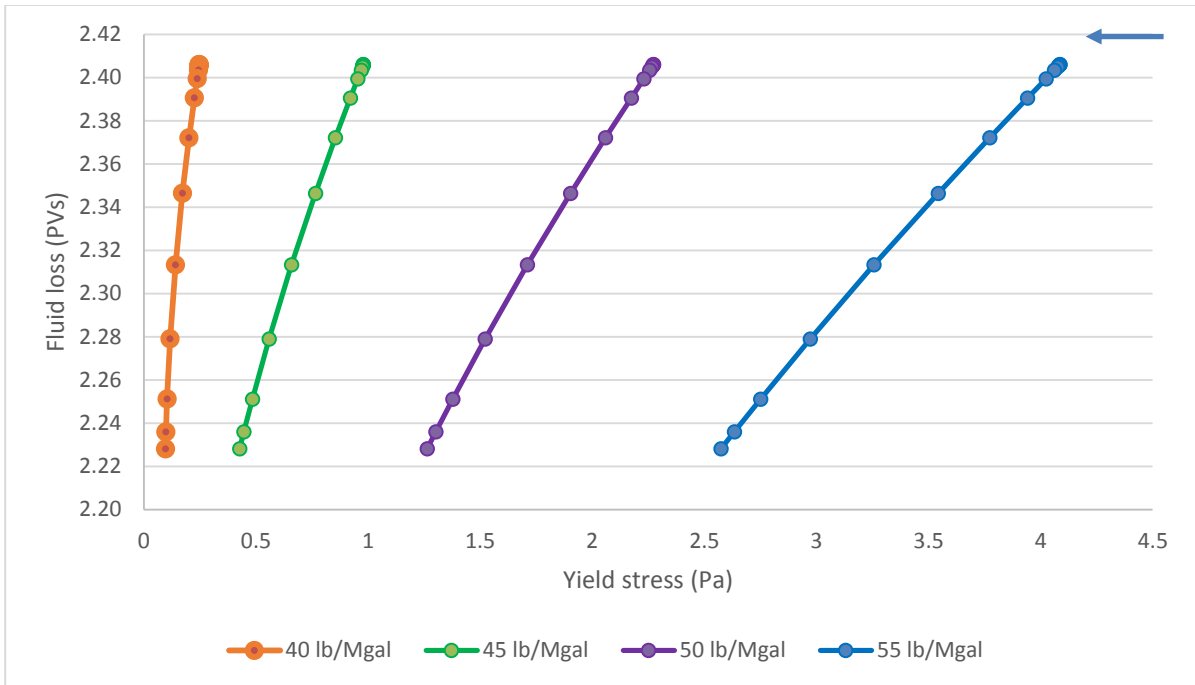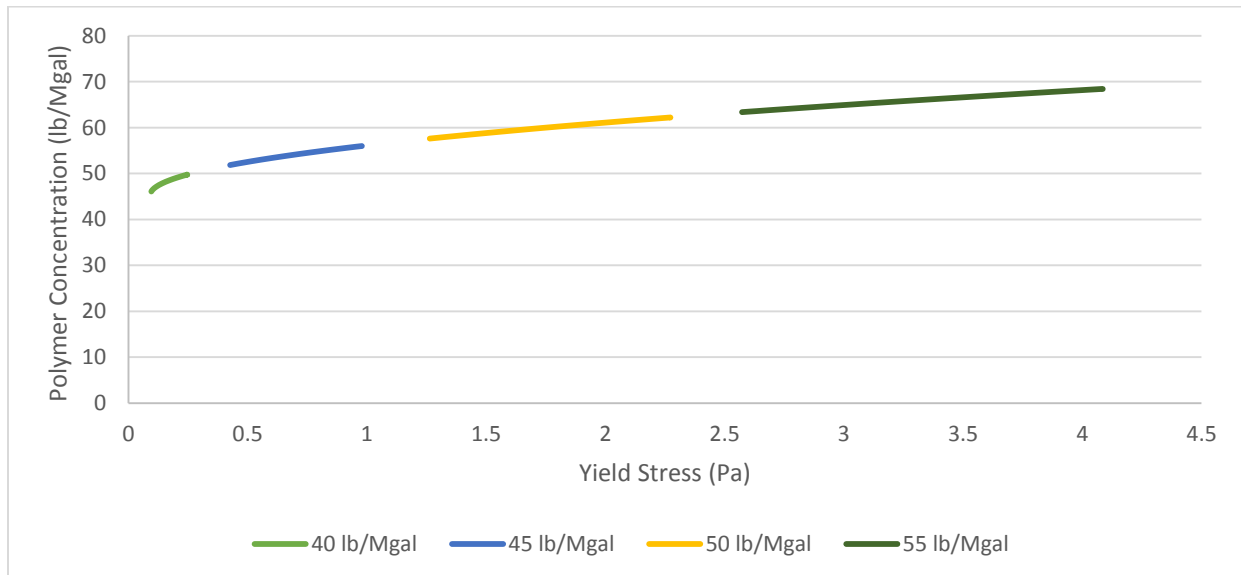centration, **Figure 63** along the fracture face were calculated. The variation in yield stress distribution along the fracture face becomes more significant with increasing polymer concentration. The relationship between polymer concentration variations with yield stress along the fracture face becomes more linear for increasing values of initial guar concentration. Also, there exist a critical breaker concentration value for which the yield stress of the fracturing fluid generated along the fracture face is reduced to zero. This cut-off breaker concentration increases linearly with guar concentration, **Figure 64**. This is in conformity with the results reported in Ben et al. [47]. Cumulative gas production for each of these scenarios were simulated and reported as in **Figure 65**.
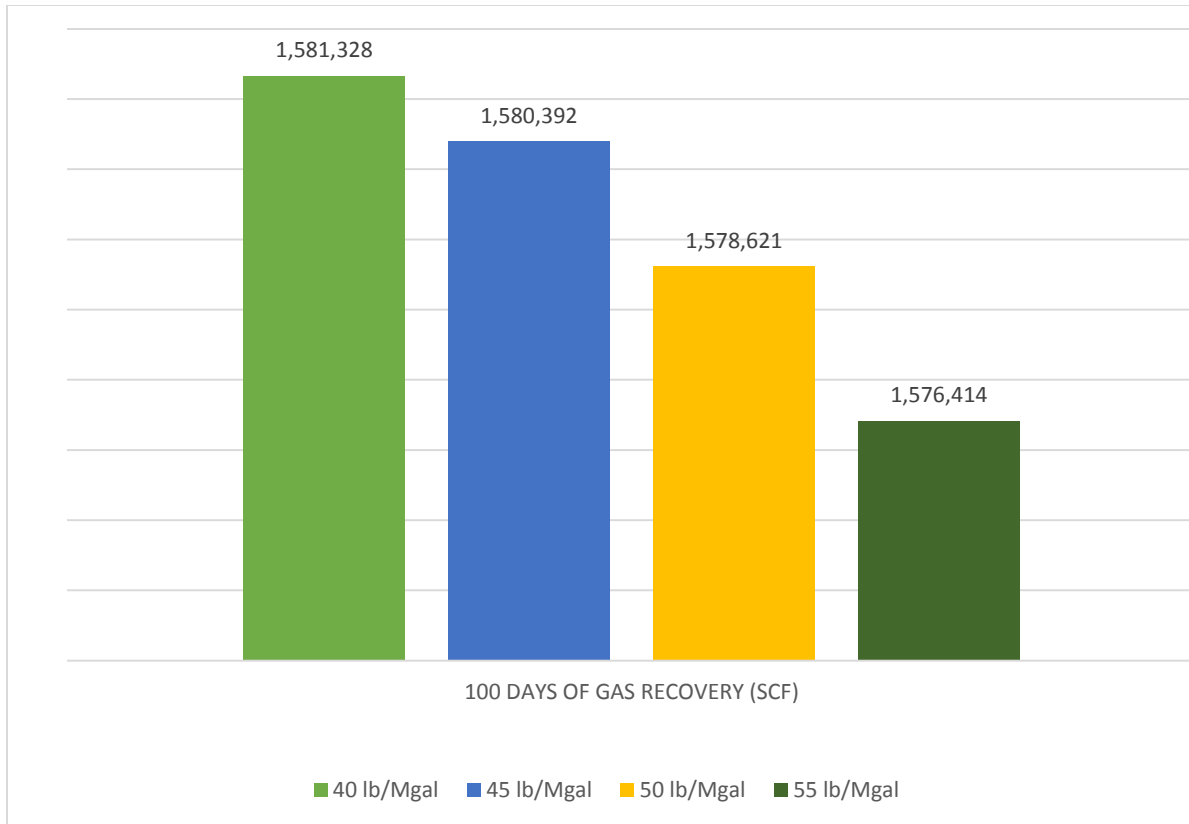
Figure 65. Cumulative gas production in (SCF) at different initial guar concentrations resulting in varying yield stress along the fracture face after 100 days of run time.

4.2.1.3   Effect of Fracture Length

In order to enhance the performance of hydraulically fractured wells, accurate estimates of fracture lengths (i.e. created, propped and effective lengths) are important in the choice of fracture design configurations and consequently, a major determinant of the overall success of the fracture treatment in tight gas reservoirs. The created fracture length is the fracture length propagated during the fracture treatment while the propped fracture length is a measure of how far down the fracture are proppants deposited. However, the effective or producing fracture length is most important as it greatly influences fluid recovery. The effective fracture length is that part of the fracture containing proppants where the fracturing fluid has cleaned up so natural gas can flow to the wellbore. The propped length is usually 70% or more of the created length while the effective

length is often only 10 to 50% of the propped length [7]. Fracture half lengths estimated from pressure transient test are roughly only 5 to 11% of the designed lengths while fracture lengths determined from reservoir simulation history matching average about 68% of the designed lengths [53]. Effective fracture lengths calculated from Pressure test analysis are significantly lower than the actual values due to damage caused by gel residues and non-Darcy effects and are affected more by fracture conductivities than by formation permeability [55].
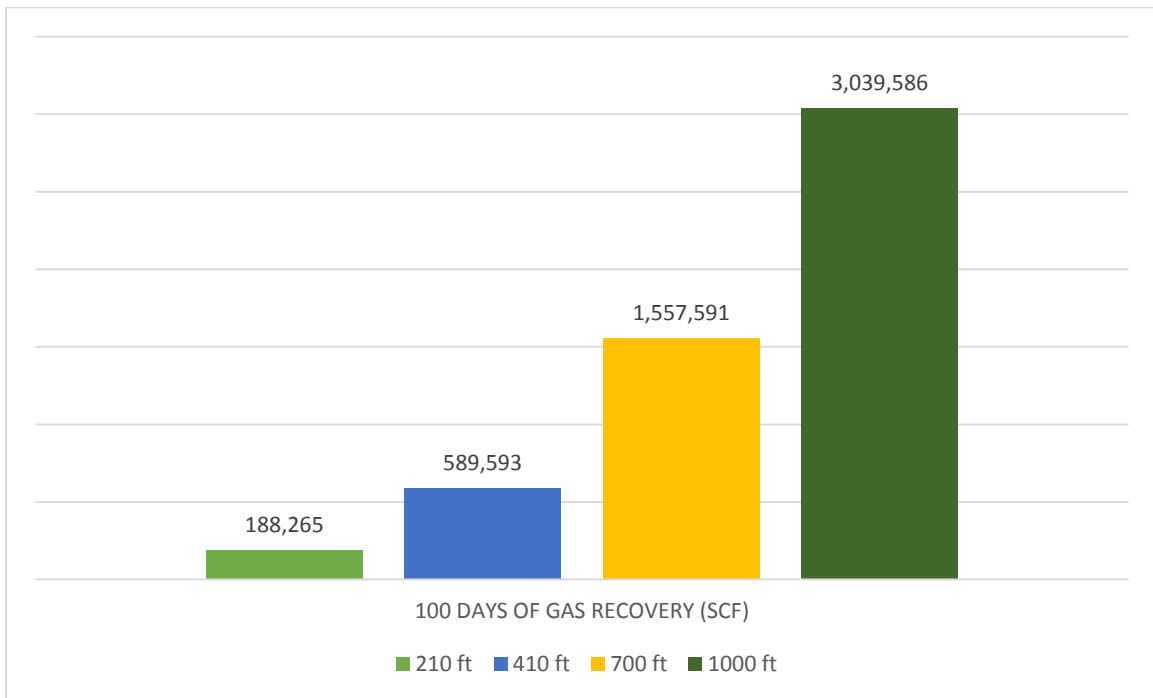

Figure 66. Cumulative gas production in (SCF) for different propped fracture lengths after 100 days of run time, k= 0.05 md, τ_0=5Pa, n=0.5 and k'=200 $mPa.s^{n'}$
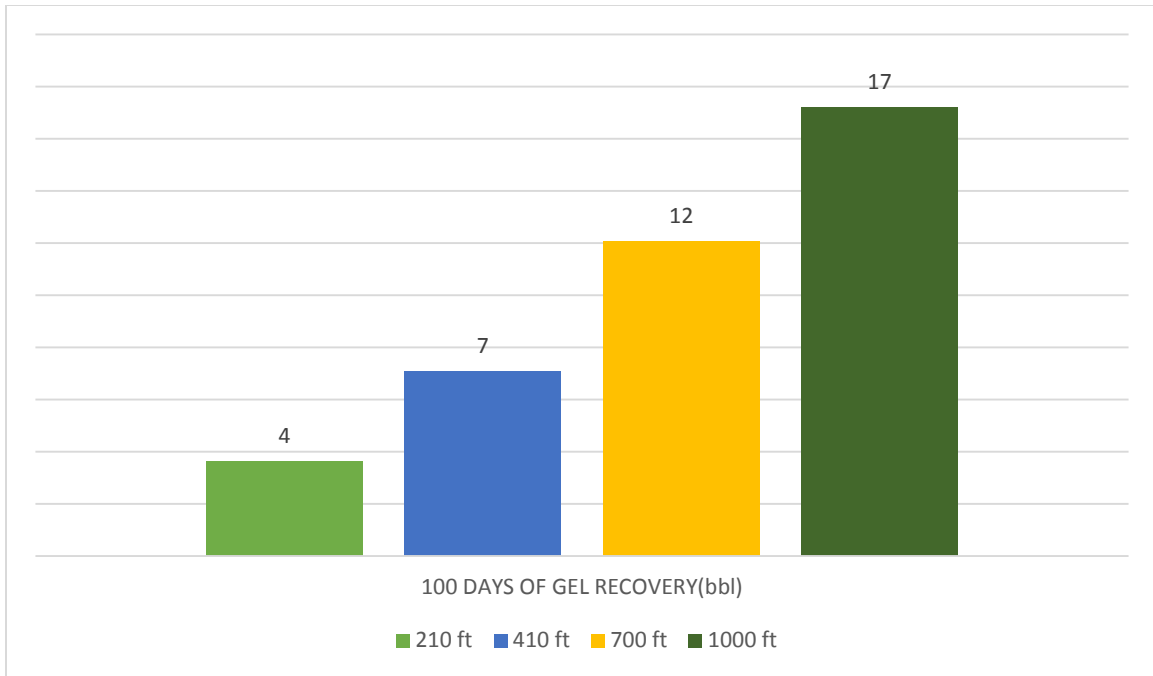
Figure 67.Cumulative gel production in (bbl) for different propped fracture lengths after 100 days of run time, k= 0.05 md, τ_0=5 Pa, n=0.5 and k'=200 $mPa.s^{n'}$

Effective fracture lengths is a property that increases with time as the fracturing fluid is gradually cleaned up. A hydraulic fracturing treatment is designed to create an extensive or highly conductive path for flow back of fluid to the wellbore. Usually only up to 50% of the injected polymer can be recovered during the cleanup process. Core plugging and proppant pack permeability reduction resulting from incomplete gel degradation is the main cause of the disparity that exists between effective and propped fracture lengths.

The longer the effective fracture length created, the greater the effective stimulation of the well as more of the formation is exposed to the wellbore resulting in higher fluid recovery. Assuming the fracture lengths simulated in this study to be quite representative of the expected effective fracture lengths, it is easy to see that cumulative fluid production increases with increasing effective fracture lengths **Figures 66 and 67.** In designing fracture treatments, it is important to take into account proppant retardation for both water and conventional gel fracturing fluids for a good estimate of the effective fracture lengths [56].

Table 10.Cumulative production for different fracture half lengths

Fracture Category	Fracture length (L_{xf}) (feet)	Formation permeability (k_f/md)	Cumulative gas (scf)	Cumulative gel (bbl)
Short	210	0.05	188265	3.6
Intermittent	410	0.05	589593	7.1
long	700	0.05	1557591	12.1
Very long	1000	0.05	3039586	17.2

4.2.1.4   Effect of Aqueous Phase Trapping and Mechanical Damage

The injection of conventional water based fluids into the formation causes water to be trapped in the near well bore region and clays to swell in the event of poor rock-fluid compatibility. These eventually result in positive skin factors and considerable cutbacks in the permeability of the invaded zone. Capillary pressures cause water to continuously imbibe into the formation during shut-in. This increase in water saturation reduces the relative permeability to gas in the invaded zone. Aqueous phase trapping is one of the main damage mechanisms in tight gas reservoirs that significantly curtails well productivity. The gravity of the reduction is dependent on the difference in initial and true irreducible water saturation, wettability of the porous medium and the depth of the invasion zone [57]. However, the damage zone permeability must be reduced by several orders of magnitude and the capillary pressure altered for the effects of water blockage on gas flow to become significant [43]. Capillary pressure forces in the formation are the main reason for fluid retention in the formation. Lowering reservoir permeability would result in higher capillary forces as per the Leverett J-function in **Equation 1**. Low initial water saturation gas reservoirs, strongly oil-wet oil reservoirs and reservoirs where sub-irreducible water saturation exists are very susceptible to damage from water blockage. The combined effect of aqueous phase trapping and mechanical damage were simulated in this study through increasing exposure time of rock to fracturing fluid and reducing the formation permeability six inches away from the fracture face. A

linear relationship exists between the fluid loss volume and the square root of exposure time of the rock to fracturing fluid [58] .

$$Q = 0.0312\ R^2 \sqrt{\frac{K_v \Delta p}{\mu T}}$$

(114)

Where, Q is the gallons per minute of fluid lost from the fracture, K_v is the vertical permeability and T the time required for treatment in minutes.

Three scenarios were considered; the effect of increasing exposure time with no loss in formation permeability, the effect of capillary pressure changes in invaded zone and reservoir matrix and the effect of increasing mechanical damage to the formation through reducing the permeability of the damaged zone by factors of 1, 10, 100 and 1000.
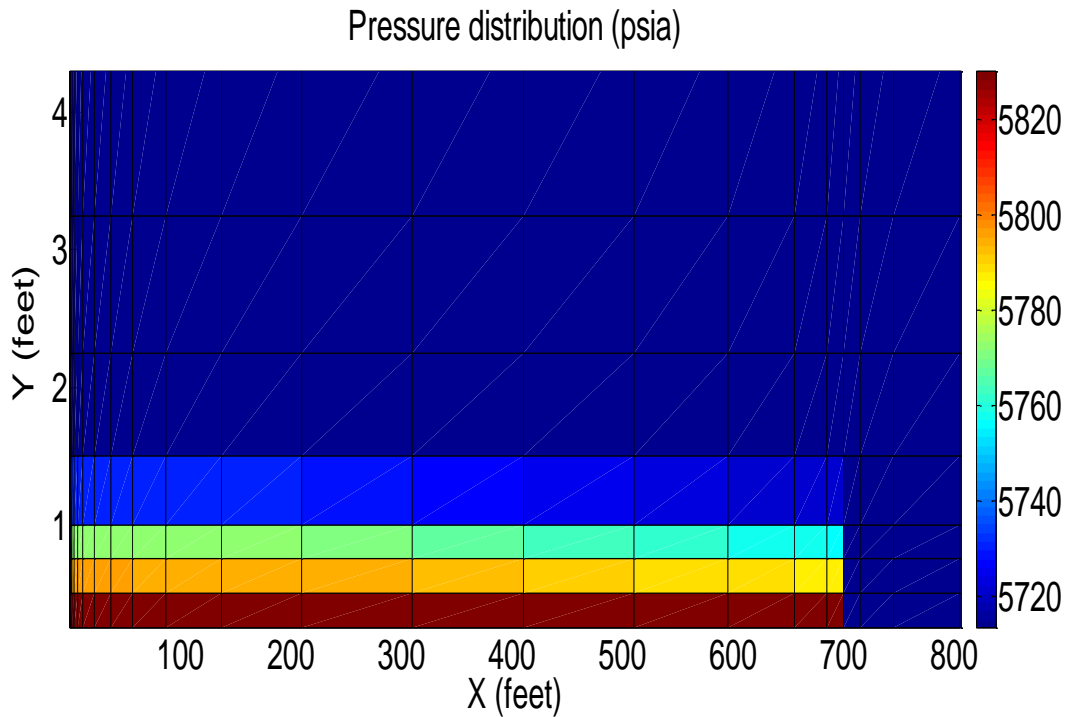

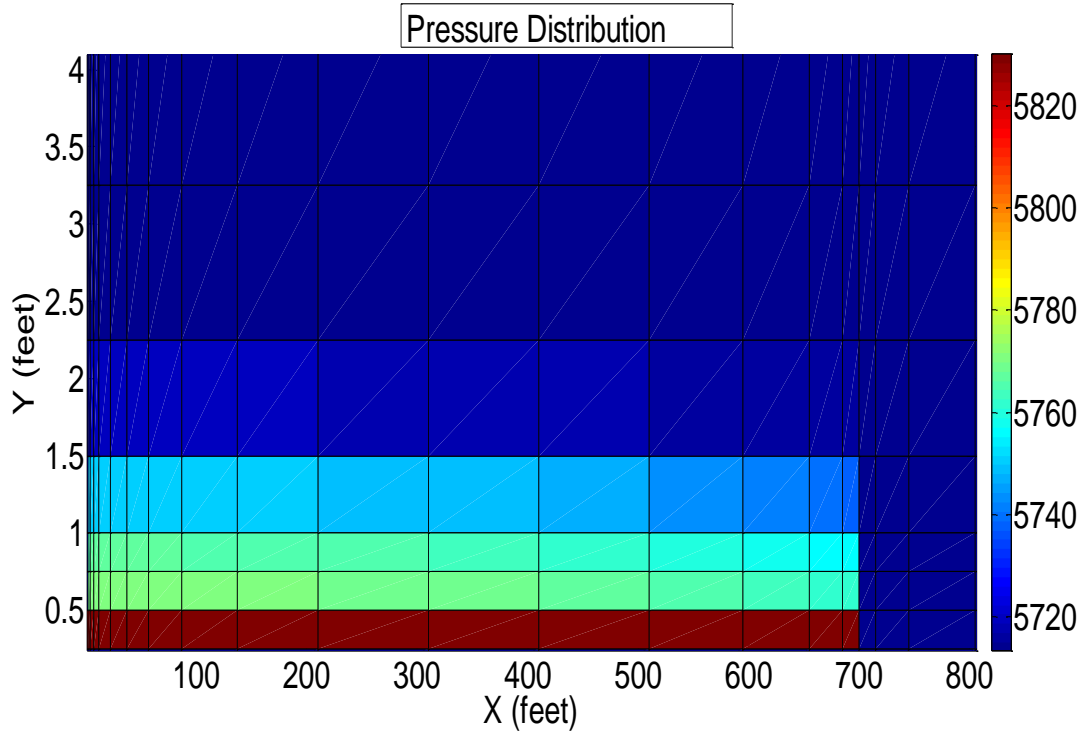*Figure 68. Pressure distribution at the end of 2.4 hours of fluid injection k =0.05md, C_{fd} =1*

Figure 69. Pressure dissipation at the end of 7.2 hours of shut-in k =0.05md, C_fd =1

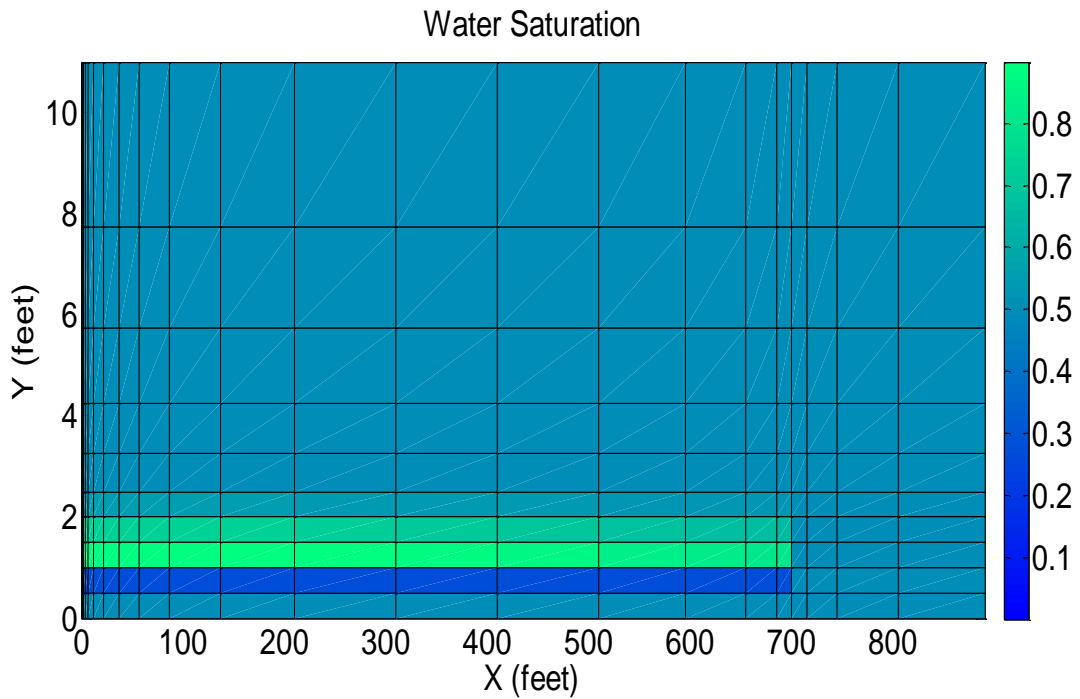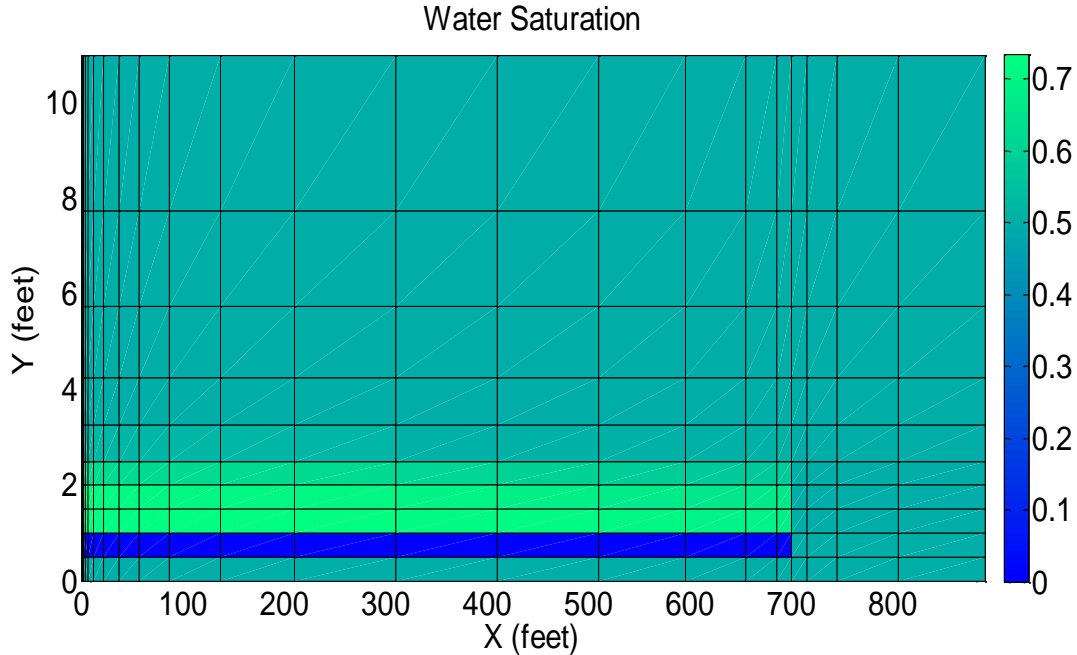*Figure 70. Water saturation at the end of 2.4 hours of fluid injection k =0.05md, C_{fd} =1*

Figure 71. Water saturation at the end of 7.2 hours of shut-in k =0.05md, C_{fd} =1

Increasing the injection time from 1.2 to 2 hours causes the water saturation around the fracture face to increase by roughly 16%, **Figure 70.** However, with increasing shut-in time from 1.2 to 7.2 hours, the high capillary forces in the formation causes the high water saturation around the fracture face to be further imbibed into the matrix. Thus the immediate water saturation around the fracture face after the second shut-in period is reduced by roughly 7.5 % relative to the first shut-in period, **Figure 71.** This cut in water saturation results in higher gas relative permeability, higher gas saturation around the fracture face and consequently higher gas production for the period under consideration, **Figure 72**. However, increasing the shut-in time increases the depth of the invaded zone as the water saturation moves further into the formation, **Figure 71.** The huge pressure buildup around the fracture at the end of injection period is equally dissipated through the formation to near initial conditions at the end of shut-in period, **Figure 69.** Clearly, aqueous phase trapping or water blocking is an important damage mechanism as the high water saturation clogging the pores around the fracture face could severely impede gas flow during recovery. However, its impact could be mitigated by shutting in the well for longer periods after injection to enhance production from tight gas formations.

Figure 72. Showing the effect of increasing shut-in time on cumulative gas production in (SCF) after 100 days of run time, for C_{fd} *=1, k= 0.05 md,* $n' = 0.5, k'= 200\ mPa.s^{n'},\ \tau_0 = 5\ Pa$

The effect of capillary pressure on fluid recovery was simulated in this study by progressively reducing the capillary forces in the formation. Capillary forces in the invaded zone and matrix are responsible for fluid retention and depend greatly upon the interfacial tension and the contact angle. Lowering the capillary pressure forces in the formation had quite an effect on fluid recovery: raising the pressure on the lower density fluid (gas) and consequently resulting in higher cumulative gas production. The effect of capillary pressure showed more than a 10% decrease in gas production as seen in **Figure 73.**

Figure 73. Showing the effect of capillary pressure on cumulative gas production in (SCF) after 100 days of run time, for $C_{fd} =1$, k= 0.05 md, $n' = 0.5$, k'= $200\ mPa.s^{n'}$, $\tau_0 = 5Pa$

Table 11. Effect of capillary pressure on cumulative production k=0.05md, $C_{fd}=1$, $n' = 0.5$, k'= $200\ mPa.s^{n'}$, $\tau_0 = 5Pa$

Effect of Capillary pressure changes				
Capillary pressure(P_c) psi P_{cmax}	Injection time (t/day)	Shut-in time (t/day)	Formation permeability (k_f/md)	Cumulative gas (scf)
11.7	0.05	0.05	0.05	1618657
58.4	0.05	0.05	0.05	1580408
116.7	0.05	0.05	0.05	1557591
350.1	0.05	0.05	0.05	1466260

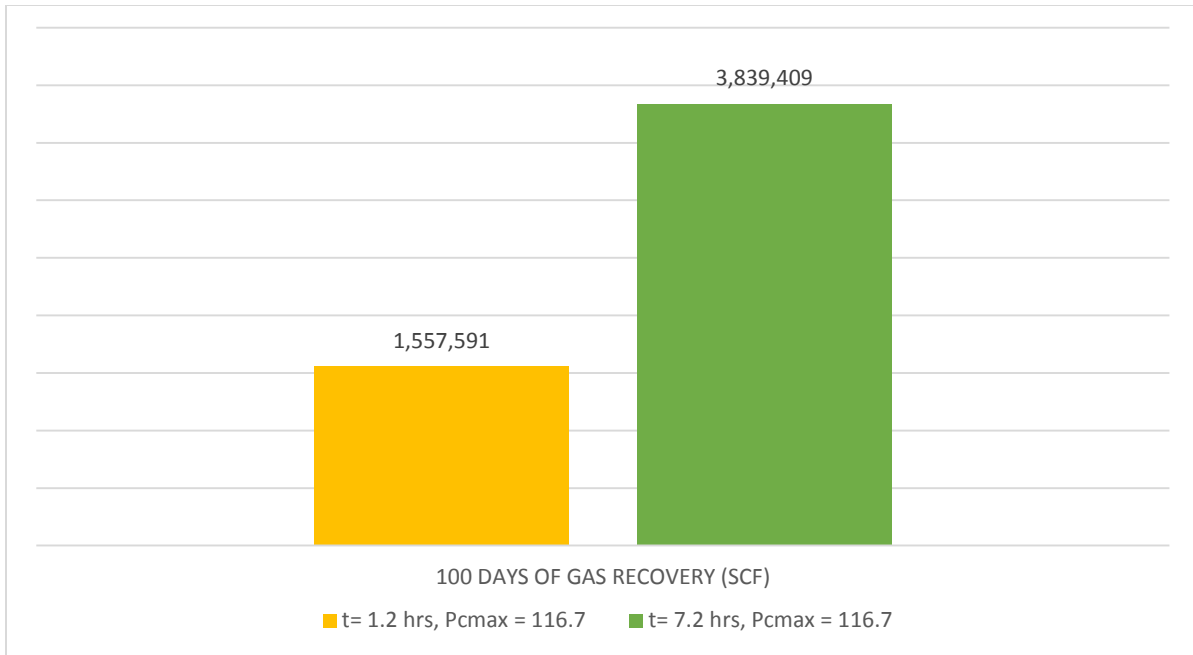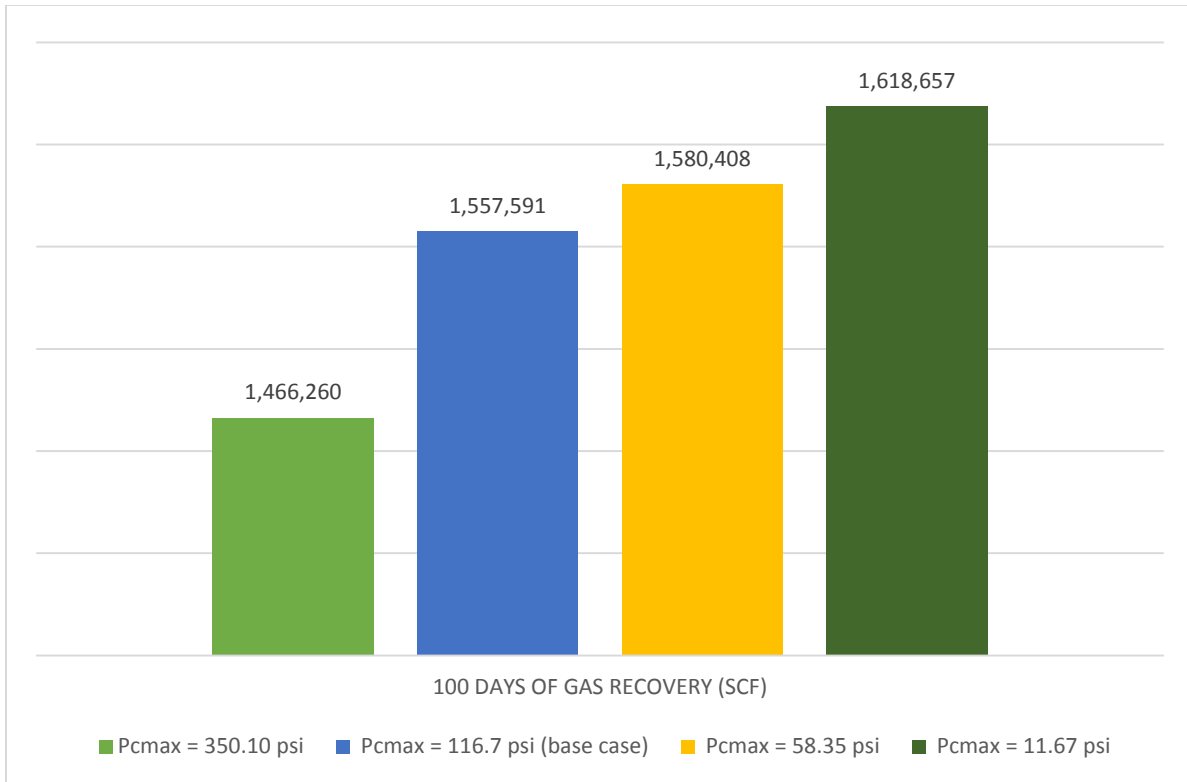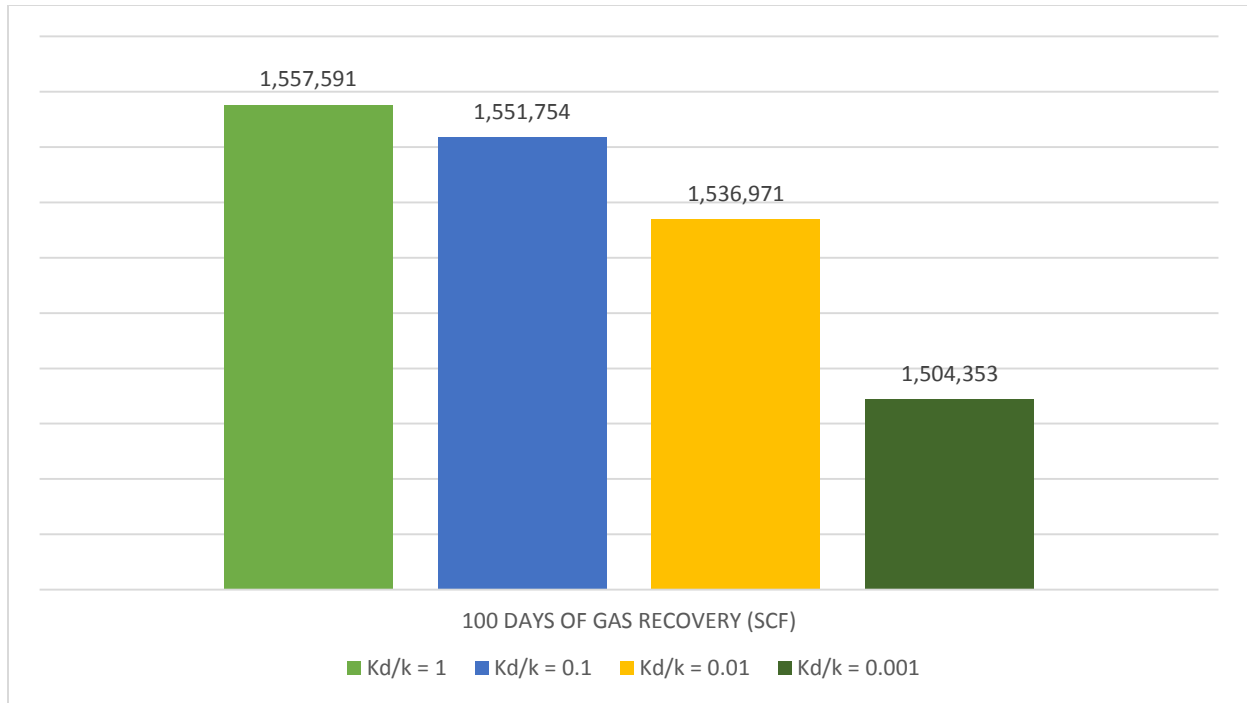*Figure 74. Showing the effect of mechanical damage on cumulative gas production in (SCF) after 100 days of run time, for C_{fd}=1, k= 0.05 md, n'= 0.5, k'= 200 $mPa.s^{n'}$, τ_0=5 Pa*

Table 12. Effect of mechanical damage on cumulative production k =0.05md, C_{fd} =1

mechanical damage resulting in loss in formation permeability			
Shear thinning properties	Damage ratio (DR) $$DR = \frac{k_d}{k}$$	Damage zone permeability (k_d/md)	Cumulative gas (scf)
τ_0=5 Pa, n=0.5 and k'=200 $mPa.s^{n'}$	1	0.05	1557591
τ_0=5 Pa, n=0.5 and k'=200 $mPa.s^{n'}$	0.1	0.005	1551754
τ_0=5 Pa, n=0.5 and k'=200 $mPa.s^{n'}$	0.01	0.0005	1536971
τ_0=5 Pa, n=0.5 and k'=200 $mPa.s^{n'}$	0.001	0.00005	1504353

The effect of mechanical damage for constant rheology (non-Newtonian) of the fracturing fluid was simulated by reducing the permeability of a small layer (6 inches away from the fracture face) by factors of 1, 10, 100 and 1000. Significant reductions in cumulative gas production were only observed when the formation permeability in the damaged zone (k_d) was reduced by several orders of magnitude (>100) and the capillary pressure in the formation altered as per the Leverett function defined in **Equation 3** and reported in **Table 12 .** For a damage ratio of 0.001 and a damage depth of 0.5 feet, cumulative gas production is curbed by 3.5% relative to an undamaged matrix. Capillary pressure in the damaged zone increases with increasing levels of damage resulting in lower gas rates and cumulative gas production. Lowering the permeability of the damaged zone equally prevents significant imbibition of water into the undamaged matrix during production, resulting in lower gas relative permeability and consequently lower gas production. From **Figure 74,** it is easy to see that higher values of capillary pressure in the invaded zone can enhance the negative effects of mechanical damage along the fracture face with a yield stress fluid present.
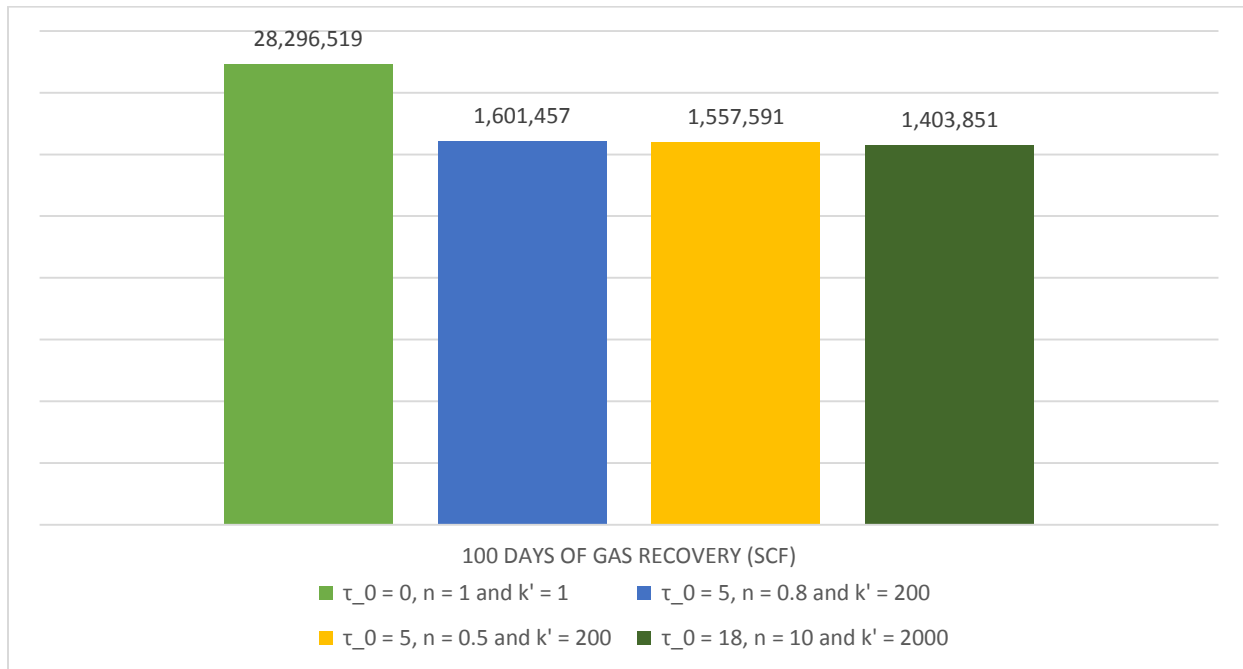
Figure 75. Effect of fluid type on cumulative gas production in (SCF) after 100 days of run time.

Table 13. Effect of fluid type on cumulative production k =0.05md, C_{fd} =1

113

Effect of fluid type		
Fluid type	Shear thinning/thickening properties	Cumulative gas (scf)
Newtonian	τ_0=0 Pa, n=1 and k'=1 mPa. $s^{n'}$	28296519
Shear thinning	τ_0=0 Pa, n=0.5 and k'=50 mPa. $s^{n'}$	1640929
Shear thinning	τ_0=5 Pa, n=0.5 and k'=50 mPa. $s^{n'}$	1628653
Shear thinning	τ_0=5 Pa, n=0.8 and k'=200 mPa. $s^{n'}$	1601457
Shear thinning	τ_0=5 Pa, n=0.5 and k'=200 mPa. $s^{n'}$	1557591
Shear thickening	τ_0=18 Pa, n=10 and k'=2000 mPa. $s^{n'}$	1403850
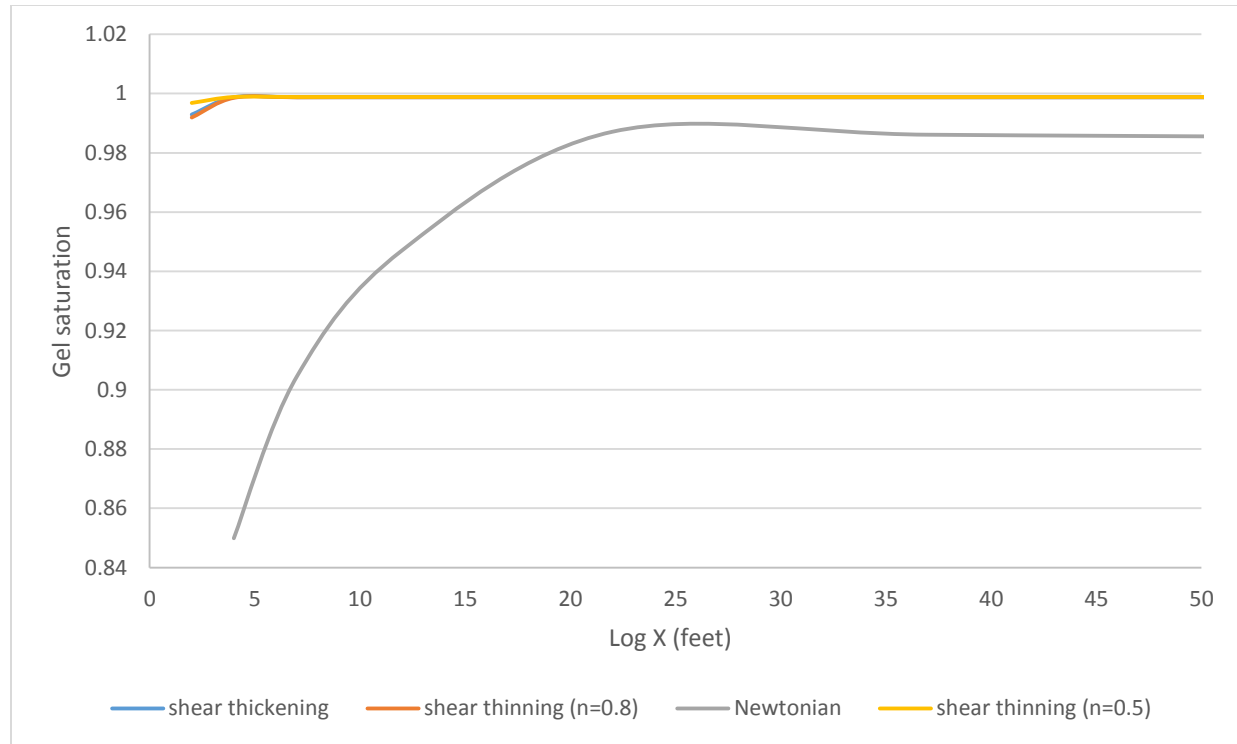
Figure 76. Showing the effect of fluid type on cumulative gel saturation after 100 days of run time, for k= 0.05 md, $Cfd = 1$, n = 0.5, k'= 200, τ_0=5Pa.

The effect of fluid type was simulated by using a shear thinning fluid with yield stress ($\tau_0 = 5, and\ n = 0.5\ or\ 0.8$), a shear thickening fluid (such as cornstarch with viscosity of 2000cp in a 1.5 M solution) and a Newtonian fluid with ($\tau_0 = 0,\ n = 1$). Cumulative gas production is increased by a factor of 17.16 when the fracturing fluid type was switched from non-Newtonian to Newtonian as can be seen in **Figure 75**, thus reiterating the importance of ample degradability of fracturing fluids on the fracturing fluid cleanup process. **Figure 76** shows quite a bit of an effect of fluid type on gel saturation distribution along the fracture face as the fracture cleans up a lot faster when a Newtonian fluid is simulated compared to a non-Newtonian fluid.

5   Conclusion and Recommendations

For this study, a 2-D, three-phase simulator tool was developed and used in analyzing certain damaging mechanisms, and providing guidelines for characterizing fractured wells in tight gas reservoirs. The effects of fracture conductivity, breaker concentration on the yield stress of partially-degraded filter cake, fracture length, capillary forces, formation damage and aqueous phase trapping on the fracturing cleanup process have been fairly investigated. The main inferences are as follows

    I.   The three-phase IMPES simulator developed for this study is stable, fast and robust. It accurately models three-phase flow through any structured grid.

    II.   The gridding system proposed by Bennett accurately represents the transient response of a hydraulically fractured well and as such it is recommended for all future fracture grid modeling configurations.

    III.   A shift in the capillary pressure curve to higher values significantly reduces fluid recovery. Increasing the capillary pressure to a maximum of 350.10 psi resulted in a 10.4% decrease in cumulative gas production.

    IV.   For tight gas formations ($k = 0.05 md$), fluid recovery increases with increasing shut-in time, increasing fracture conductivity and fracture length irrespective of the yield stress of the fracturing fluid.

    V.   Increasing the breaker concentration for a more complete degradation of the yield stress of the fracturing fluid would significantly enhance production.

    VI.   The rate of increase in the yield stress of the fracturing fluid along the fracture face is proportional to the square of the volume of fluid loss (PVs) to the formation.

    VII.   For low permeability reservoirs, mechanically induced formation damage combined with hydraulic damage tends to be the most significant.

    VIII.   It is more realistic to simulate yield stress variation along the fracture face rather than assuming constant values because the fluid lost to the formation and the polymer concentration distribution along the fracture face decreases as we move away from the injection well.

Nomenclature and Abbreviations

$\gamma =$ shear rate (s^{-1})

$\mu =$ viscosity of fluid (cp)

$\mu_w =$ viscosity of water (cp)

$\rho =$ density of fluid (g/cm^3)

$\rho_p =$ density of proppants $(g/cm3$ or $kg/m^3)$

$\rho_s =$ density of fluids $(g/cm^3$ or $kg/m^3)$

$\tau_o =$ yield stress (Pa)

$\Phi =$ potential gradients

$\Phi =$ rock porosity (fraction)

$C_t =$ total compressibility of reservoir fluid (psi^{-1})

$C_w =$ water compressibility of reservoir fluid (psi^{-1})

$C_g =$ gas compressibility of reservoir fluid (psi^{-1})

$C_o =$ oil compressibility of reservoir fluid (psi^{-1})

$C_r =$ rock compressibility of reservoir fluid (psi^{-1})

$g =$ Acceleration due to gravity (m/s^2)

$L_f =$ fracture length (ft)

$b =$ fracture width (ft)

$K' =$ consistency index non $-$ Newtonian fluid $(kPa \bullet sn')$

$n' =$ behavior index of a non $-$ Newtonian fluid

$P_c =$ capillary pressure, psi

$P_i =$ initial reservoir pressure, psi

$p_{wf} =$ bottom $-$ hole flowing pressure, psi

q_{sp} = flow rate, $bbl\ or\ scf/D$

S_g = gas saturation, fraction

S_w = water saturation, fraction

S_o = oil saturation, fraction

S_{gel} = gel saturation, fraction

Δx = grid size in the x − direction, ft

Δy = grid size in the y − direction, ft

Δt = timestep (days)

h = reservoir net thickness, ft

k = formation permeability, md

k_f = fracture permeability, md

k_{rg} = relative permeability to gas, md

k_{rw} = relative permeability to water, md

C_{fd} = dimensionless fracture conductivity, $(wkf)/(\pi\ Lf\ k)$

IMB = material balance

f_w = fractional flow of water, fraction

t_{Dxf} = dimensionless time

μ_{nn} = viscosity of gel (cp)

d = proppant diameter (m)

w = mass flow rates (kg/s)

Λ = mobility ratio (μ^{-1})

C_{lg} = coefficient usd in describibg the expansion of the accumulation term

References

[1] "The National Academies of Sciences, Engineering and Medicine," [Online]. Available: http://needtoknow.nas.edu/energy/energy-sources/fossil-fuels/natural-gas/.

[2] "The U.S. Energy Information Administration," [Online]. Available: https://www.eia.gov/tools/faqs/faq.php?id=58&t=8.

[3] J. L. Gidley, S. A. Holditch, D. E. Nierode and R. W. Veatch Jr, "Recent Advances In Hydraulic Fracturing," *SPE,* 1990.

[4] "The U.S. Energy Information Administration," Hydraulically fractured wells provide two-thirds of U.S. natural gas production, 5th May 2016. [Online]. Available: https://www.eia.gov/todayinenergy/detail.php?id=26112. [Accessed April 2017].

[5] J. Ayoub, R. E. Hutchins, F. Van der Bas, S. Cobianco, C. Emiliani, M. Glover, M. Kohler, S. Marino, G. Nitters, D. Norman and G. Turk, "New Findings in Fracture Cleanup Change Industry Perceptions," in *paper presented at the SPE International Symposium and Exhibition on Formation Damage Control ,February 15-17*, Lafayette, lousiana, 2006.

[6] M. Economides and N. K.G., "Reservoir Stimulation", 3rd Edition ed., John Wiley & Sons, Inc, 2000.

[7] Y. Wang, " Simulation of Fracture Fluid Cleanup and its Effects on Long-Term Recovery In Tight Gas Reservoirs",PhD dissertation, Dept. Petroleum Eng., Texas A&M Univ., 2008.

[8] D. Davies and T. Kulper, "Fracture Conductivity in Hydraulic Fracture Stimulation," *Journal of Petroleum Technology,* 1988.

[9] R.B. Ghahfarokhi, "Fracturing Fluid Cleanup by Controlled Release of Enzymes from Polyelectrolyte Complex Nanoparticles-PhD thesis", Lawrence: University of Kansas, 2010.

[10] Holditch S.A. and Tschirhart N.R., "Optimal Stimulation Treatments in Tight Gas sands," *SPE 96104,* 2005.

[11] E. May, L. Britt and K. Nolte, "The effect of Yield Stress on Fracture Fluid Cleanup," presented at the SPE Annual Technical Conference and Exhibition, San Antonio, Texas, October 5-8., 1997.

[12] T. Friedel, "Numerical Simulation of Production from Tight-Gas Reservoirs by Advanced Stimulation Technologies ", PhD thesis, Freiberg University, 2004.

[13] I. Faergestad, "Formation Damage," 2016.

[14] H. Qutob and M. Byrne, "Formation Damage in Tight Gas Reservoirs," *Society of Petroleum Engineers,* 3 June 2015.

[15] S. A. Holditch, "Factors Affecting Water Blocking and Gas Flow From Hydraulically Fractured Gas Wells," pp. JPT 1515-24., (December 1979).

[16] G. Voneiff, B. Robinson and S. Holditch, "The Effect of Unbroken Fracture Fluid on Gas Well Performance," *SPEPF,* pp. 223-229., 1996.

[17]   T. Friedel, "Numerical Investigation on Hydraulic Fracture Cleanup and its Impact on the Productivity of a Gas Well with a non-Newtonian Fluid Model," 2006.

[18]   R. Gdanski, J. Weaver, B. Slabaugh, H. Walter and Parker, "Fracture Face Damage – It Matters," 25-27 May 2005.

[19]   R. Gdanski, F. Dwilight and S. Chun, "Fracture-Face-Skin Evolution During cleanup," in *presented at the SPE Annual Technical Conference and Exhibition,*, San Antonio, Texas, 2006.

[20]   Cinco-Ley. and Fernando Samaniego V., "Effects of Wellbore storage and Damage on the Transient Pressure behavior of Vertically fractured Wells," *SPE 6752,* 1977.

[21]   T. Al-Fariss, S. King and K. L. Pinder, "Flow of Shear-Thinning Liquid with Yield Stress through Porous Media," Texas, 1985.

[22]   C. Bennett, A. Reynolds, R. Raghavan and J. Elbel, "Performance of Finite Conductivity, Vertically Fractured Wells in Single-Layer Reservoirs," *SPEFE,* pp. 399-412., 1986.

[23]   R. Barati, R. Hutchins, T. Friedel, J. Ayoub, M. Dessinges and E. K. :, "Fracture Impact of Yield stress and fracture-face damage on production with a three phase 2D Model," *SPE productions & operations,* 2009.

[24]   R. Argarwal, R. Carter and C. Pollock, "Evaluation and Performance Prediction of Low Permeability Gas Wells Stmulated by Massive Hydraulic Fracturing," *JPT (March 1979) 362-72; Trans, AIME, 267. SPE-6838-PA.,* 1979.

[25]   P. Ghahri, M. Jamiolahmady and M. Sohrabi, "A Thorough Investigation Of Cleanup Efficiency Of Hydraulic Fractured Wells Using Response Surface Method," in *SPE European Formation Damage Conference*, 2011.

[26]   B. Cai, B. Guoqiang, J. Xu, C. He, Y. Gao, J. Chen, N. Cheng and J. Wang, "Damage Appraisal of Massive Hydraulic Fracture Stimulation in Unconventional Oil and Gas Reservoirs," in *presented at the SPE Asian Pacific Oil and Gas Conference Exhibition*, Perth, Australia, 2016.

[27]   T. Ertekin, J. H. Abou-Kassem and G. R. King, "Basic Applied Reservoir Simulation", SPE Textbook Series Vol.7, Copyright 2001, pp. 297- 299.

[28]   L. J. Klinkenberg, "The permeability of porous media to liquids and gases," *Drilling and Production Practice,* 1941.

[29]   H. Philip, "Evolution of Permeability-Porosity Trends In Sandstones," 2000.

[30]   J. W. Draper, " A Textbook on Chemistry", p.46, 1861.

[31]   I. N. Levine, "Physical Chemistry", University of Brooklyn: McGraw-Hill, 1978.

[32]   F. Fayers and J. Mathews, "Evaluation of Normalized Stone's Methods for Estimating Three-Phase Relative Permeabilities," *Society of Petroleum Engineers,* April 1984.

[33]   M. Leverett and M. Lewis, "Steady flow of Gas-Oil-water Mixtures through Unconsolidated Sands," *Society of Petroleum Engineers,* 1941.

[34]   A. Kantzas and B. Nikakhar, "Principles of three phase Capillary pressures," *Petroleum Society of Canada,* 1998.

[35]   S. Whitaker, "Flow in porous media : A theoretical derivation of Darcy's law", 1986.

[36]   K. Coats, "IMPES Stability: Selection of Stable Timestep," *Society of Petroleumm Engineers,* 2003.

[37]   K. Coats, "IMPES Stability: The CFL Limit," in *presented at the SPE Reservoir Simulation Symposium*, Houston, 2001.

[38]   S. Y. and Schultz M.H., "GMRES: A generalized minimal residual algorithm for solving nonsymmetric linear systems," *SIAM J.,* 1986.

[39]   G. Schein, "The Application and Technology of Slickwater Fracturing," p. SPE Distinguished Lecture, 2005.

[40]   G. Coulter, E. Benton and C. Thomson, "Water Fracs and Sand Quantity: A Barnett Shale Example," in *presented at the SPE Annual Technical Conference and Exhibition,*, Houston, Texas,, 2004.

[41]   S. A. Holditch and J. Ely, "Successful Stimulation of Deep Wells Using High Proppant Concentrations," *JPT 25 (08),* pp. 959-964., 1973.

[42]   J. A. Ayoub, R. E. Hutchins, F. Van der Bas, S. Cobianco, C. N. Emiliani, M. Glover, M. Kohler, S. Marino, G. Nitters, D. Norman and G. Turk, "New Results Improve Fracture Cleanup Characterization and Damage Mitigation," 2006.

[43]   S. A. Holditch, "Factors Affecting Water Blocking and Gas Flow From Hydraulically Fractured Gas Wells," pp. JPT 1515-24., (December 1979).

[44]   J. Wang, S. Holditch and D. McVay, "Simulation of gel damage on Fracture Fluid Cleanup and Long-term recovery in Tight Gas Reservoirs," *SPE paper 117444,* 2008.

[45]   C. E. Cooke, "Effect of fracturing fluids on Fracture conductivity," *Journal of Petroleum Technology, 27(SPE Paper 5114):,* pp. 1273-1282, Oct. 1975.

[46]   T. T. Palisch, R. J. Duenckel, L. W. Bazan, J. H. Heidt and G. A. Turk, "Determining Realistic Fracture Conductivity and Understanding its Impact on Well Performance - Theory and Field Examples," *Society of Petroleum Engineers,* 1 January 2007.

[47]   X. Ben, A. Hill, Z. Ding and L. Wang, "Experimental Evaluation of Guar Fracture Fluid Filter Cake Behavior," in *presented at the SPE hydraulic Fracturing Technology Conference and Exhibition held in the Woodlands,24-26 January*, Texas USA, 2011.

[48]   R. Seright, "Conformance Improvements Using Gels," New Mexico Institute of Mining and Technology/US DOE, Sorroco, New Mexico, 2002.

[49]   "Proppant and Fluid," Consortia, Stim-Lab , 1997-2006.

[50]   C. Montgomery, Effective and Sustainable Hydraulic Fracturing, P. B. Andrew, M. John and R. J., Eds., Tulsa, Oklahoma: NSI Technologies,, 2013.

[51]   X. Yi, "Model for Displacement of Herschel-Bulkley Non-Newtonian Fluid by Newtonian Fluid in Porous Media and Its Application in Fracturing Fluid Cleanup," in *presented at International Symposium and Exhibition on Formation Damage Control*, Lafayette, Louisiana,, 2004.

[52]   "Oil & Gas Fields of Colorado/Nebraska & Adjacent areas," 1982. [Online]. Available: http://archives.datapages.com/data/rmag/oilgasfields82/plumbushcreek.pdf. [Accessed 5th May 2017].

[53]   W. Lee and S. Holditch, "Fracture Evaluation with Pressure Transient Testing in Low-Permeability Gas Reservoirs," *9975-PA SPE Journal Paper,* 1981.

[54]   K. Farayola, A. Olaoye and A. Adewuyi, "Petroleum Reservoir Characterisation for Fluid with Yield Stress Using Finite Element Analyses," no. SPE Nigeria Annual International Conference and Exhibition, 2013.

[55]   E. P. Lolon, D. A. McVay and S. K. Schubarth, "Effect of Fracture Conductivity on Effective Fracture Length", Society of Petroleum Engineers, 2003.

[56]   M. M. Sharma and P. B. Gadde, "The Impact of Proppant Retardation on Propped Fracture Lengths," *Society of Petroleum Engineers,* 1 January 2005.

[57]   D. B. Bennion, R. F. Bietz, F. B. Thomas and M. P. Cimolai, "Reductions In the Productivity of Oil And Low Permeability Gas Reservoirs Due to Aqueous Phase Trapping," *Petroleum Society of Canada,* 1 September 1994.

[58]   J. G. Davis, J. J. Reynolds and H. F. Coffer, "The Effect of Fluid Loss on Fracture Extension," *Society of Petroleum Engineers,* 1 January 1955.

[59]   S. Oilfield glossary.

[60]   R. D. Gdanski, D. D. Fulton and C. Shen, "Fracture-Face-Skin Evolution During Cleanup," *Society of Petroleum Engineers.,* 2009.

[61]   M. R. Islam, Unconventional Gas Reservoirs: Evaluation, Appraisal, and Development, 1st Edition ed., Gulf Professional Publishing, 2014.

[62]   J. H. Abou-Kassem, M. Islam and S. Farouq Ali, Petroleum Reservoir Simulation: A Basic Approach, Copyright 2006 by Gulf Publishing Company.

[63]   J. H.P. and E. Herron, "Three-Phase Reservoir Simulation," SPE-AIME, Esso Production Research Co..

[64]   C. Bose, T. J. B. Fairchild, A. Gul and R. Ghahfarokhi, "Application of nanoproppants for fracture conductivity improvement by reducing fluid loss and packing of micro-fractures," *Journal of Natural Gas Science and Engineering,* Vols. Vols. 27, 424-431,, 30 November 2015.

[65]   S. Holditch and W. Laufer, "The Analysis of Fractured Gas Wells Using Simulation," in *presented at the SPE Annual Technical Conference and Exhibition*, Houston,Texas, 1978.

[66]   D. Peaceman, "Interpretation of Well- Block Pressures in Numerical Reservoir Simulation with Non-Square gridblocks and Anisotropic Permeability," *SPE-Paper 10528,* pp. 531-543, 1983.

A.   Appendix

Multiphase Flow Functions and Solution Techniques Applied to Flow Equations

The coefficient equations C_{lu} where $l = o, w$ or g and $u = P_o, S_w,$ or S_g used in **Equations 51, 52 and 53** are expressed as

$$C_{op} = \frac{V_b}{\alpha_c \Delta t} [\frac{\phi'}{B_o^n} + \phi^{n+1}(\frac{1}{B_o})'](1 - S_w^n - S_g^n)$$

$$C_{wp} = \frac{V_b}{\alpha_c \Delta t} [\frac{\phi'}{B_w^n} + \phi^{n+1}(\frac{1}{B_w})'](S_w^n)$$

$$C_{gp} = \frac{V_b}{\alpha_c \Delta t} (\{\left[\frac{\phi'}{B_o^n} + \phi^{n+1}\left(\frac{1}{B_o}\right)'\right] R_s^n + \left(\frac{\phi}{B_o^{n+1}}\right) R_s'\}(1 - S_w^n - S_g^n) + [\frac{\phi'}{B_g^n} + \phi^{n+1}\left(\frac{1}{B_g}\right)']S_g^n)$$

$$C_{ow} = -\frac{V_b}{\alpha_c \Delta t} (\frac{\phi}{B_o})^{n+1}$$

$$C_{ow} = -\frac{V_b}{\alpha_c \Delta t} (\frac{\phi}{B_w})^{n+1}$$

$$C_{og} = -\frac{V_b}{\alpha_c \Delta t} (\frac{\phi}{B_g})^{n+1}$$

$$C_{wg} = 0$$

$$C_{gw} = -\frac{V_b}{\alpha_c \Delta t} (\frac{\phi}{B_o})^{n+1} R_s^{n+1}$$

$$C_{gg} = -\frac{V_b}{\alpha_c \Delta t} [(\frac{\phi}{B_g})^{n+1} - (\frac{\phi}{B_o})^{n+1}] R_s^{n+1}$$

The derivatives ϕ', R_s' and $(\frac{1}{B_l})'$ are the chord slopes defined as

$$\phi' = \frac{(\phi^{n+1} - \phi^n)}{(P^{n+1} - P^n)}$$

$$R_s' = \frac{(R_s{}^{n+1} - R_s{}^n)}{(R_s{}^{n+1} - R_s{}^n)}$$

$$\left(\frac{1}{B_l}\right)' = \frac{\left(\frac{1}{B_l^{n+1}}\right) - \left(\frac{1}{B_l^n}\right)}{(P_o{}^{n+1} - P_o{}^n)}$$

History matching for the other three wells from three-phase flow exercise (Phase I).
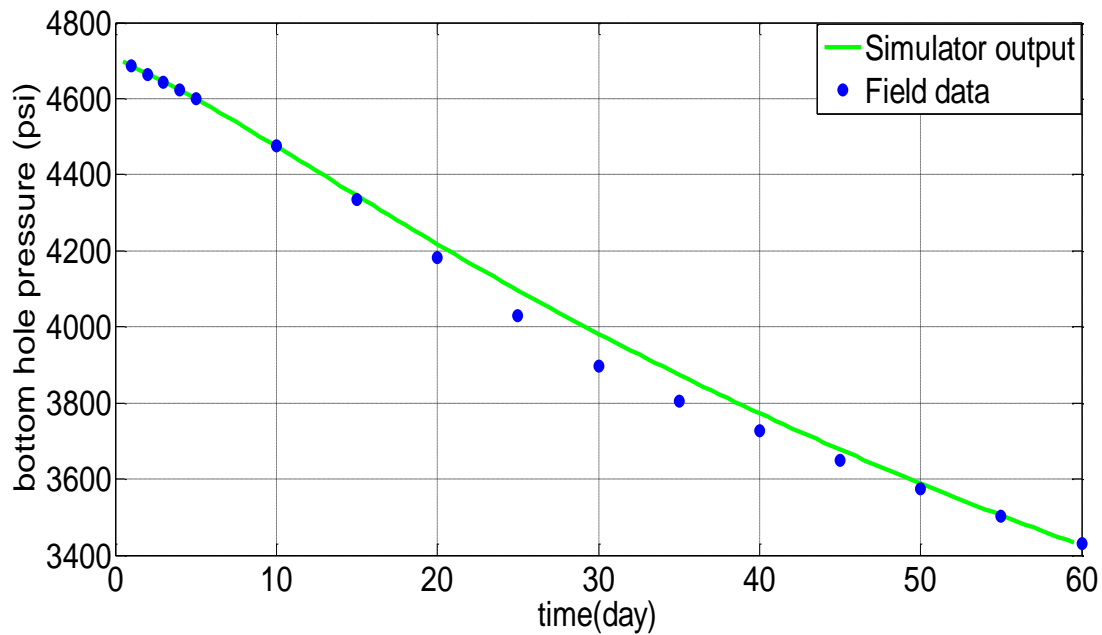
Liquid rate specified well

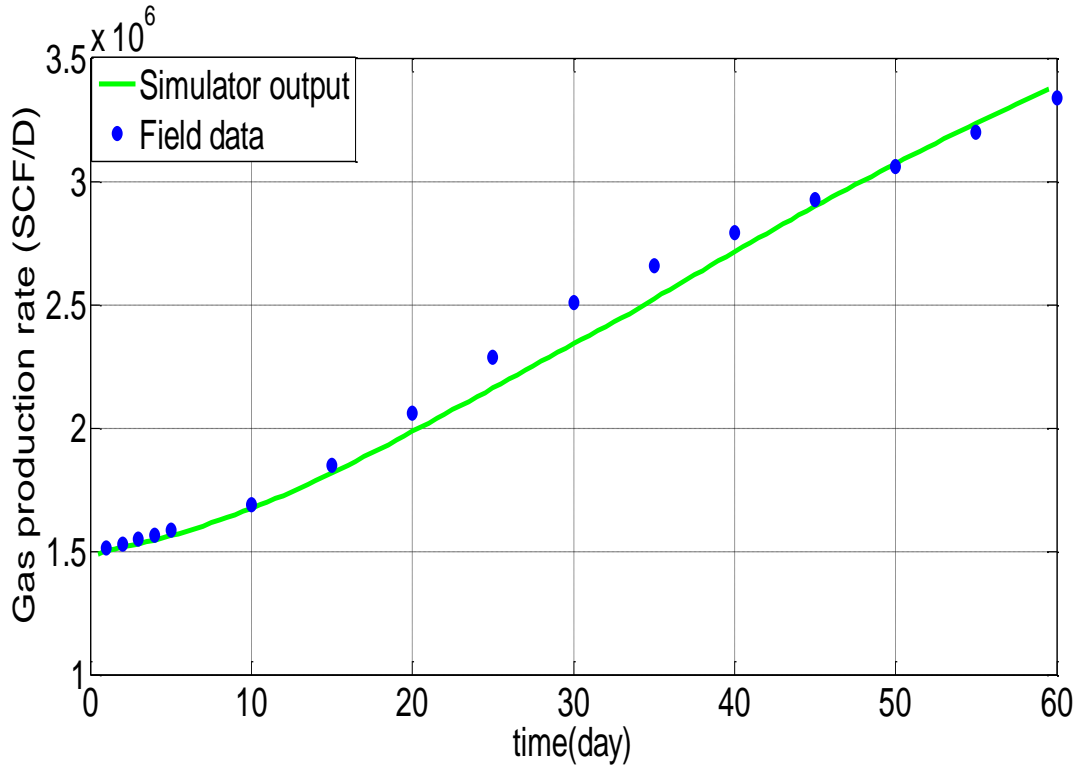*Figure 77. Bottom-hole pressure for Liquid rate specified well, (W-5)*

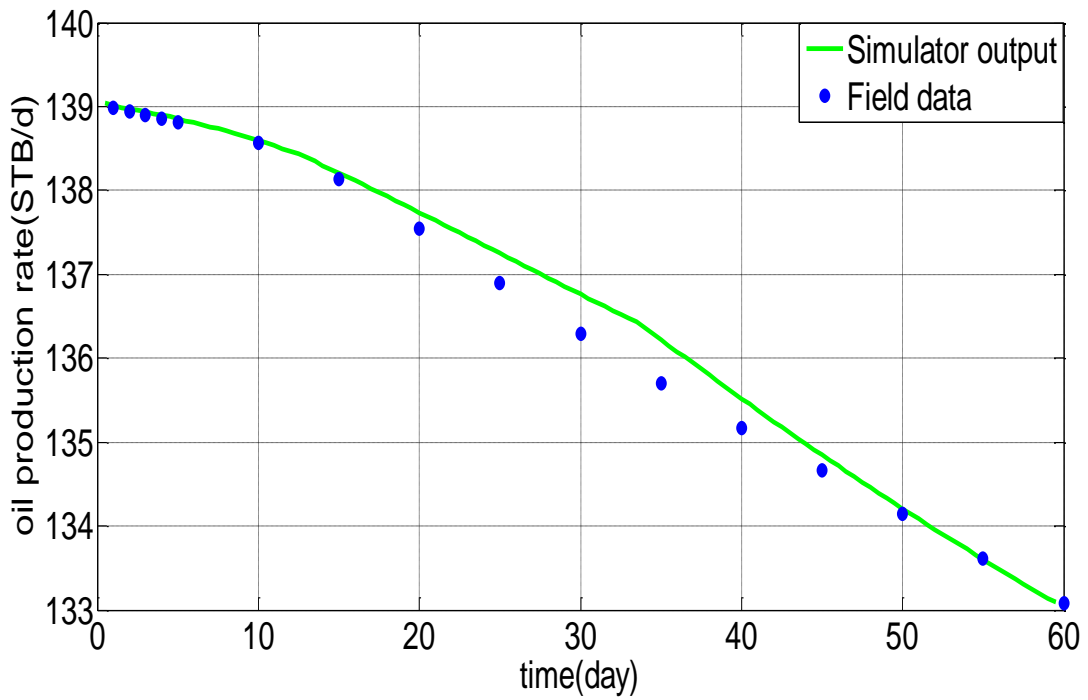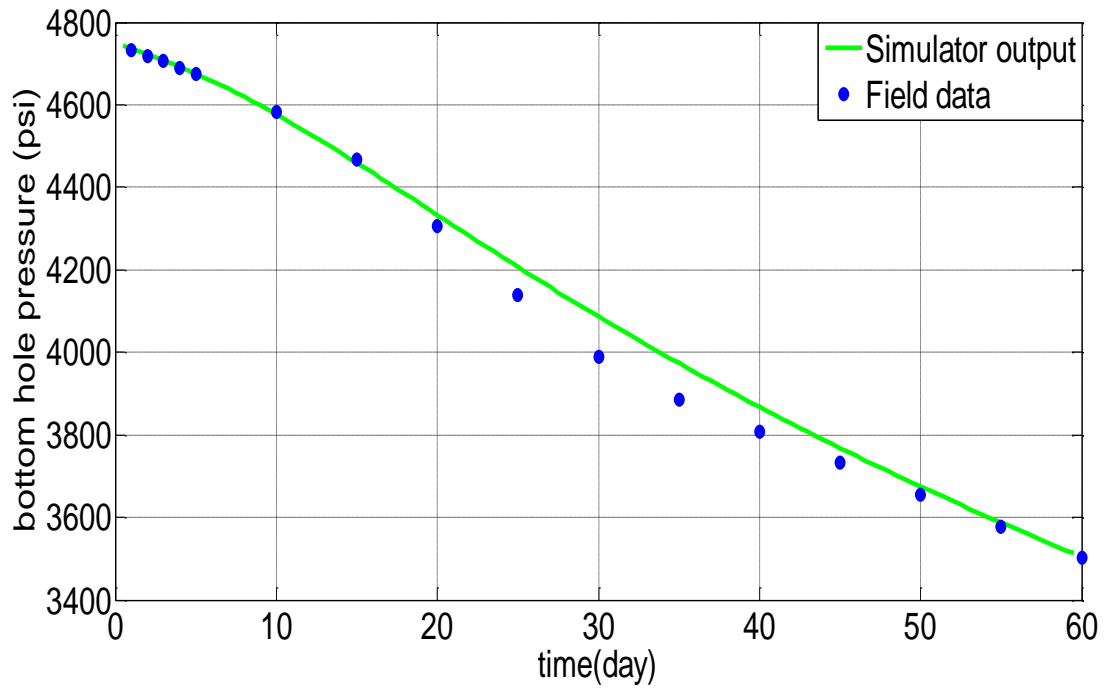*Figure 78. Gas production rate for Liquid rate specified well, (W-5)*

Figure 79. Oil production rate for Liquid rate specified well, (W-5)
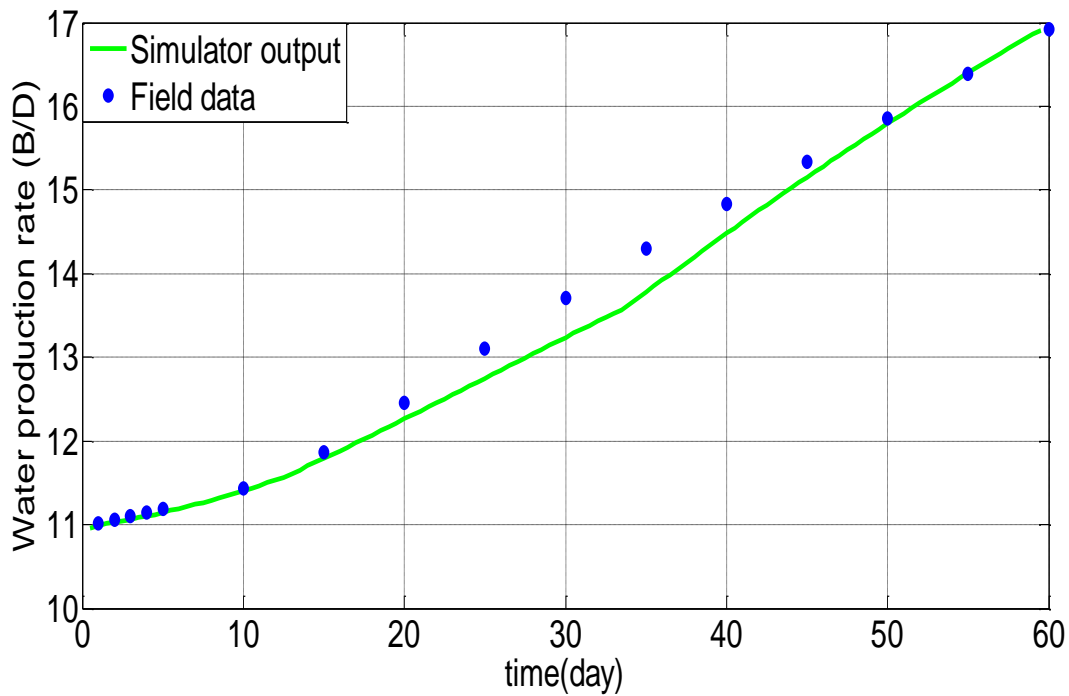
Figure 80. Water production rate for Liquid rate specified well, (W-5)

Figures 77, 78, 79 and 80 shows the bottom-hole pressures, oil, water and gas production rates realized for $(W - 5)$. In this well, a total liquid rate production of 150 STB/D was specified. Well five $(W - 5)$ responds to this boundary specification by producing 1.5 to 3.2 million standard cubic feet of gas, 133 to 139 stock tank barrels of oil and 11 to 16.5 barrels of water per day. Analysis of well performance shows an increase in water and gas production rates, accompanied by a slight decrease in oil production rate.

Oil rate specified well

Figure 81. Bottom-hole pressure for Oil rate specified well, (W-3)
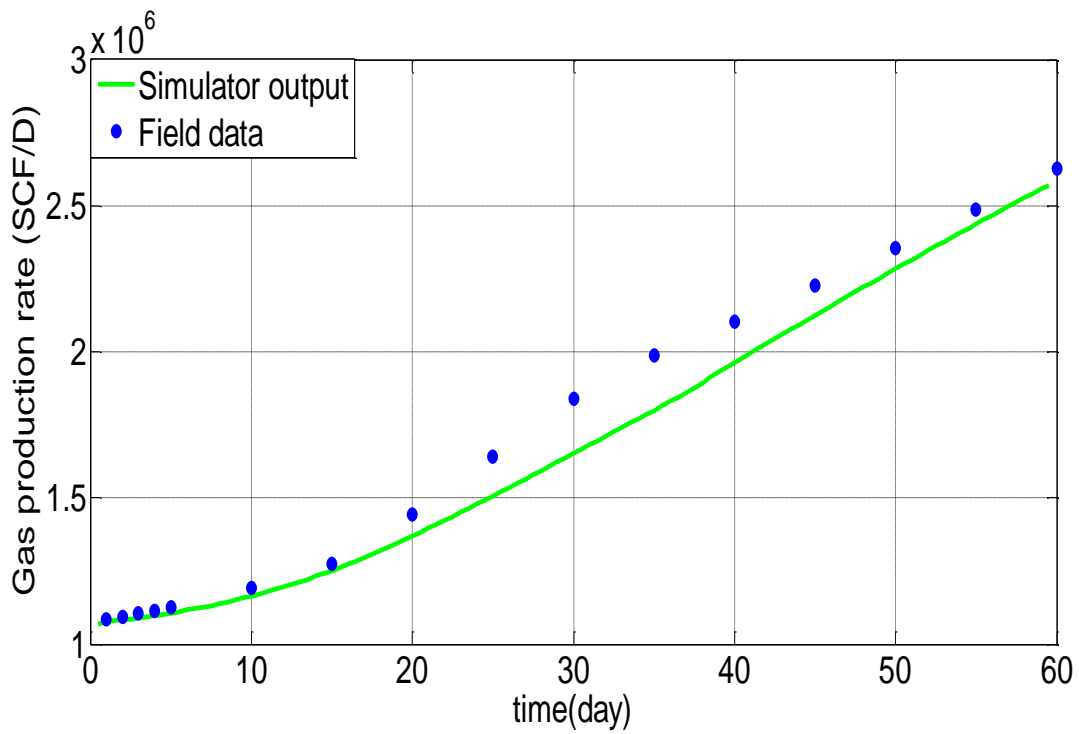

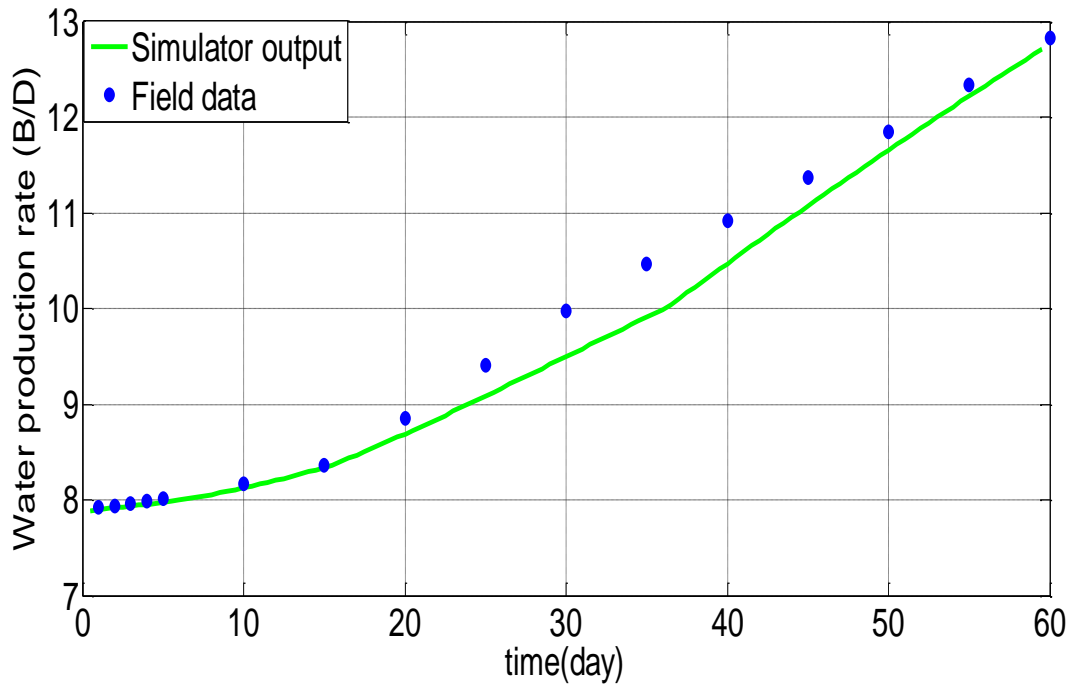*Figure 82. Gas production rate for Oil rate specified well, (W-3)*

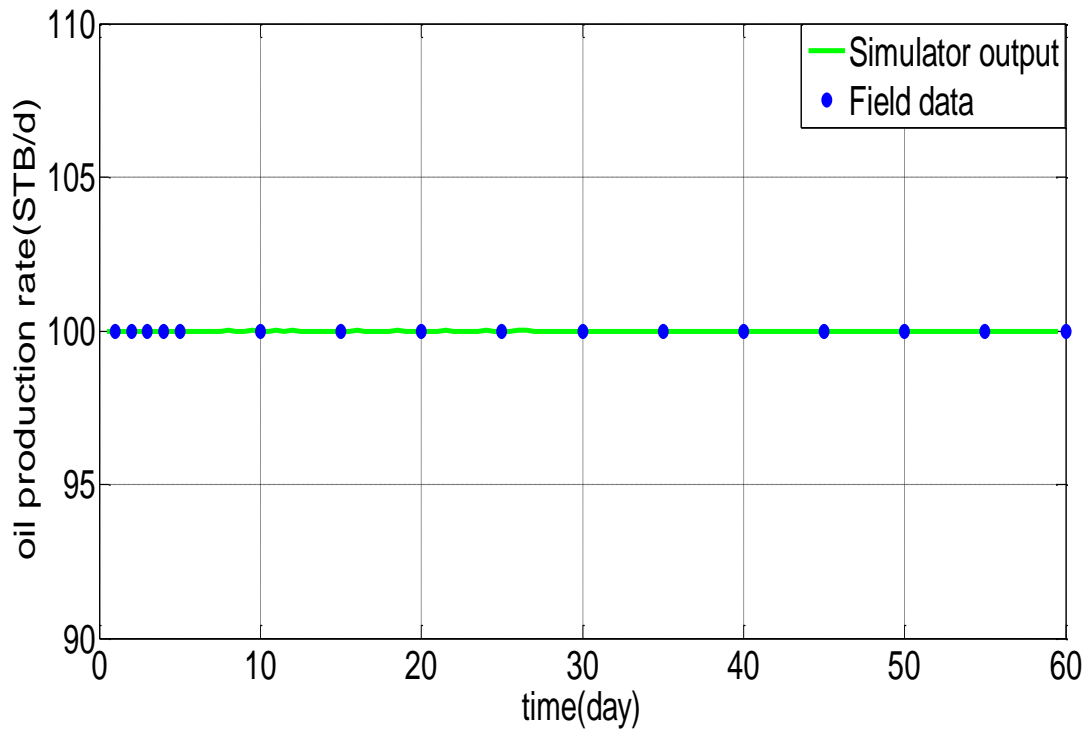*Figure 83. Water production rate for Oil rate specified well, (W-3)*

Figure 84. Oil production rate for Oil rate specified well, (W-3)

128

Figures 81, 82, 83 and 84 shows the bottom-hole pressures, oil, water and gas production rates realized for $(W - 2)$. In this well, an oil rate production at 100 stock tank barrels per day was specified. Well $(W - 3)$ responds to this boundary specification by producing produces 1 to 2.6 million standard cubic feet of gas and 8 to 13 barrels of water. Oil production rate stayed constant at 100 stock tank barrels per day at the expense of increasing water and gas production.
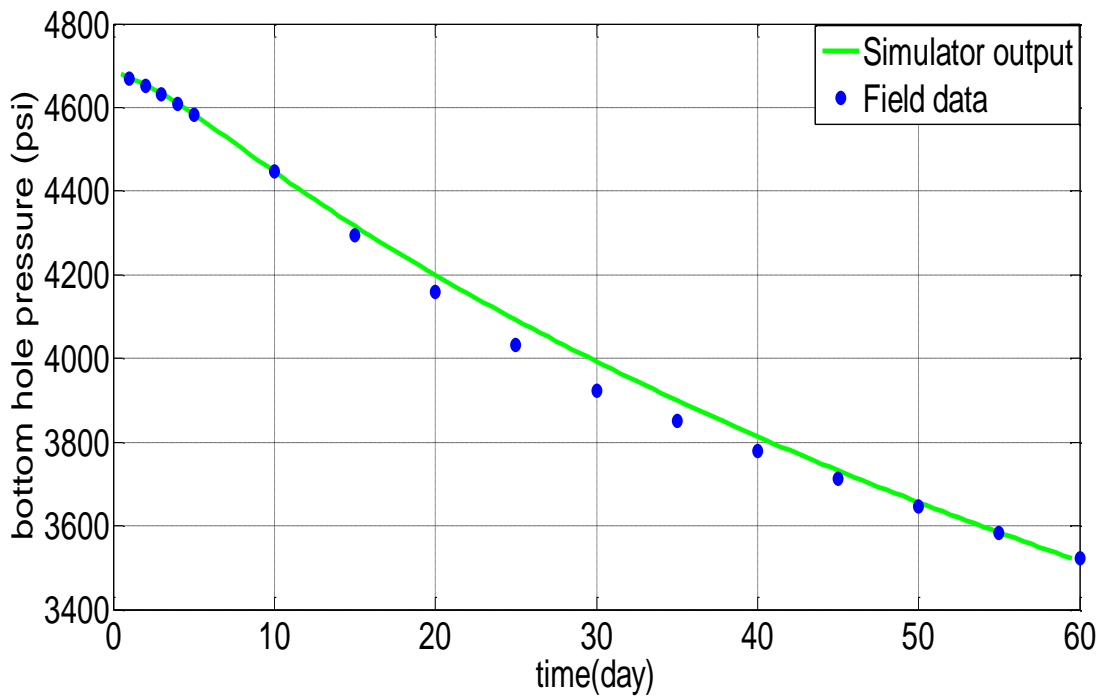
Total rate specified well

Figure 85. Bottom-hole pressure for Total rate specified well, (W-1)
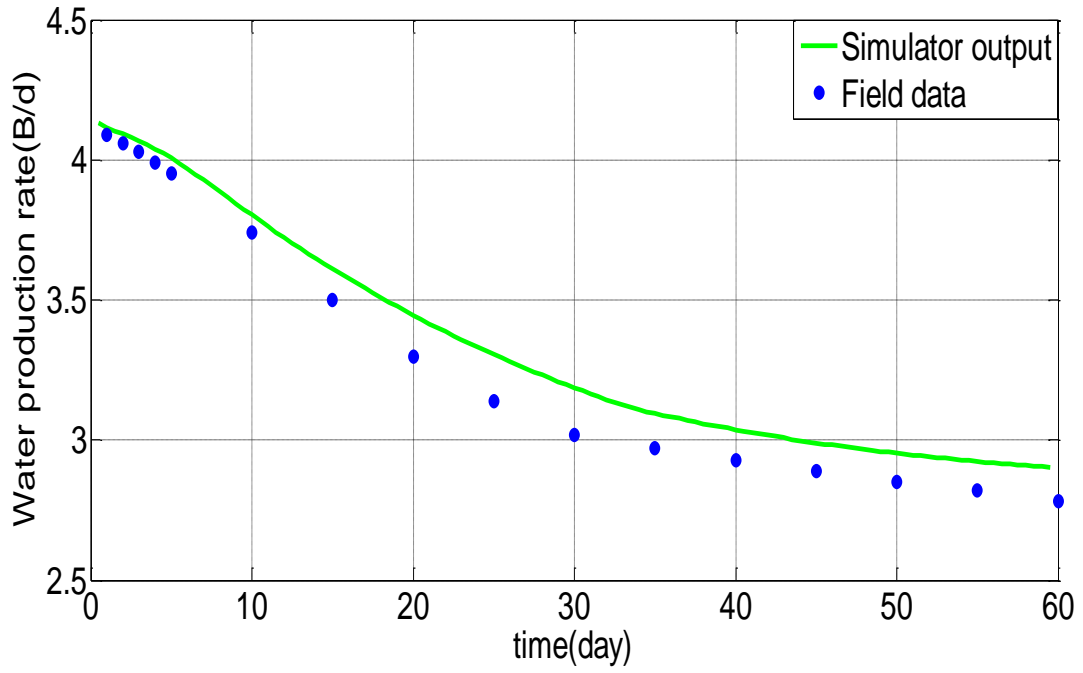
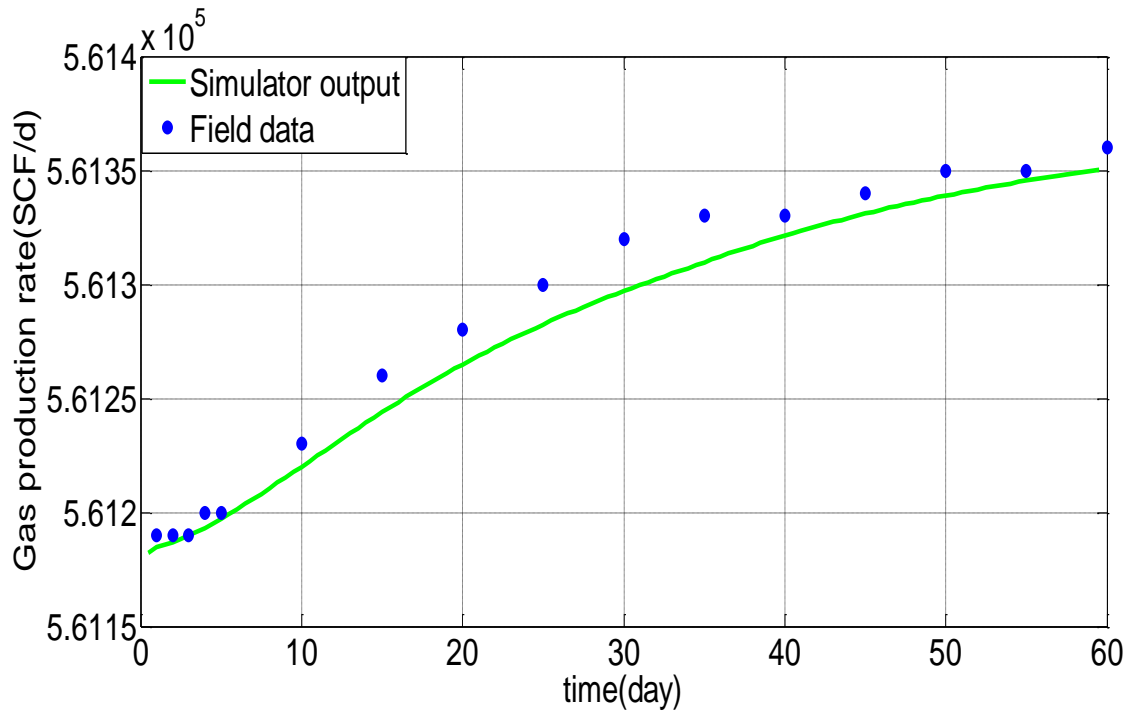*Figure 86. Water production rate for total rate specified well, (W-1)*

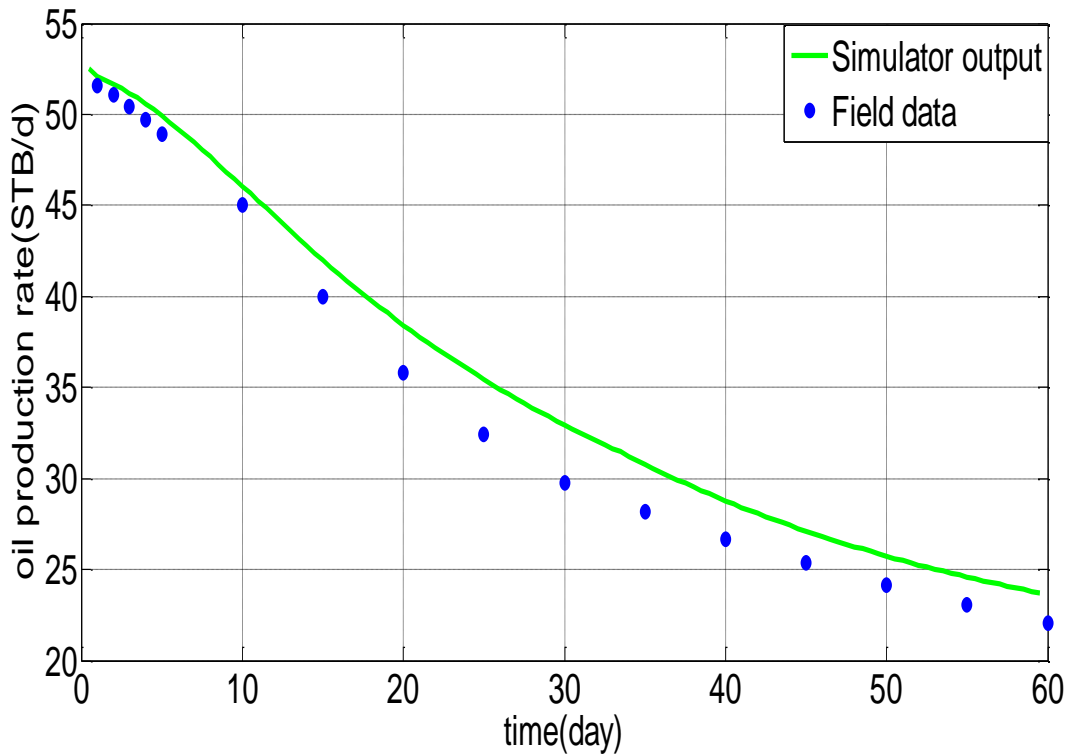*Figure 87. Gas production rate for total rate specified well, (W-1)*

Figure 88. Oil production rate for total rate specified well, (W-1)

Figures 85, 86, 87 and 88 shows the bottom-hole pressures, oil, water and gas production rates realized for $(W-2)$. In this well, a total fluid production of 100,000 stock tank barrels per day is specified. Well $(W-1)$ responds to this boundary specification by producing slightly over 0.5 million standard cubic feet of gas, 24 to 52 stock tank barrels of oil and a few barrels of water. Significant decrease in oil production from 52 to 24 stock tank barrels, steady decrease in water production from 4.2 to 2.8 barrels and slight increase in gas production from 0.5612 to 0.5614 million standard cubic feet.

Fractured Well Design

The algorithm for choosing suitable grids for fractured wells as presented by Bennett et al. [22], is as follows

For all grid blocks

$$\Delta x_{i+1/2} \leq \Delta x_i \leq \Delta x_{i-1}, \qquad i = 2 \ldots \ldots (Nx - 1).$$

$$\Delta y_{j+1/2} \leq \Delta y_i \leq \Delta y_{j-1}, \qquad j = 2 \ldots \ldots (Ny - 1).$$

Near the fracture $(x/L_{x_f} \leq 1.5, y/L_{x_f} \leq 1)$

$$\Delta x/L_{x_f} \leq 10^{-2} \quad \text{At the well for } C_{fd} \geq 100$$

$$\Delta x/L_{x_f} \leq 10^{-3} \quad \text{At the well for } C_{fd} < 100$$

$$\Delta x/L_{x_f} \leq 1.5 * 10^{-2} \text{ At the fracture tip}$$

$$\max(\Delta x/L_{x_f}) \leq 0.15$$

$$b_f/L_{x_f} = 2\Delta y_1/L_{x_f} \leq 2 * 10^{-3}$$

$$\Delta y_1 = \Delta y_2 = \Delta y_3 = \Delta y_4$$

$$\max(\Delta y/L_{x_f}) \leq 0.20$$

Near the fracture $(x/L_{x_f} > 1.5, y/L_{x_f} > 1)$

$$\max(\Delta x/L_{x_e}) \leq 0.17$$

$$\max(\Delta y/L_{x_e}) \leq 0.17$$

Figure 89. Bennett Algorithm for Fracture Well grids [22]

The length of the fracture L_{x_f}, the length of grid to external boundaries L_{i_e} and the fracture width b were very crucial in determining the grid block sizes. Grid blocks should not change too rapidly in the (x and y) directions. Finer grids should be applied to the model near the well for more accurate flow rate and bottom-hole pressure calculations and near the fracture tip to model large pressure gradients accurately. Away from the fracture larger values of Δx and Δy are used which are largely dependent on L_{i_e} .

The x and y grids used in this model were those recommended in Bennett et al. [22]

---

x-Grid – values of Δx:

[1 1 2 3 5 10 15 20 30 50 73 100 100 150 150

100 85 60 30 15 15 30 60 85 100 160 225 325]

y-Grid– values of Δy:

[0.25 0.25 0.25 0.25 0.5 0.75 1 1.5 2 3 5 10 20

30 50 75.25 100 125 175 200 250 300 325 325]

Figure 90. Recommended x and y-Grids for Fractured Wells [22]